Defense Threat Reduction Agency
8725 John J. Kingman Road, MS
6201 Fort Belvoir, VA 22060-6201

TECHNICAL REPORT

Reaction Dynamics and Dispersion of Energetic Biocides

Distribution Statement A. Approved for public release; distribution is unlimited.

April 2017

Michael R. Zachariah

Prepared by:
University of Maryland
3130 Chemistry Building
College Park, MD 20742

REPORT DOCUMENTATION PAGE

Public reporting burden for this collection of information is estimated to average 1 hour per response, including the time for reviewing instructions, searching existing data sources, gathering and maintaining the data needed, and completing and reviewing this collection of information. Send comments regarding this burden estimate or any other aspect of this collection of information, including suggestions for reducing this burden to Department of Defense, Washington Headquarters Services, Directorate for Information Operations and Reports (0704-0188), 1215 Jefferson Davis Highway, Suite 1204, Arlington, VA 22202-4302. Respondents should be aware that notwithstanding any other provision of law, no person shall be subject to any penalty for failing to comply with a collection of information if it does not display a currently valid OMB control number. **PLEASE DO NOT RETURN YOUR FORM TO THE ABOVE ADDRESS.**

1. REPORT DATE *(DD-MM-YYYY)*	2. REPORT TYPE	3. DATES COVERED *(From - To)*

4. TITLE AND SUBTITLE

5a. CONTRACT NUMBER

5b. GRANT NUMBER

5c. PROGRAM ELEMENT NUMBER

6. AUTHOR(S)

5d. PROJECT NUMBER

5e. TASK NUMBER

5f. WORK UNIT NUMBER

7. PERFORMING ORGANIZATION NAME(S) AND ADDRESS(ES)

8. PERFORMING ORGANIZATION REPORT NUMBER

9. SPONSORING / MONITORING AGENCY NAME(S) AND ADDRESS(ES)

10. SPONSOR/MONITOR'S ACRONYM(S)

11. SPONSOR/MONITOR'S REPORT NUMBER(S)

12. DISTRIBUTION / AVAILABILITY STATEMENT

13. SUPPLEMENTARY NOTES

14. ABSTRACT

15. SUBJECT TERMS

16. SECURITY CLASSIFICATION OF:			17. LIMITATION OF ABSTRACT	18. NUMBER OF PAGES	19a. NAME OF RESPONSIBLE PERSON
a. REPORT	b. ABSTRACT	c. THIS PAGE			19b. TELEPHONE NUMBER *(include area code)*

Standard Form 298 (Rev. 8-98)
Prescribed by ANSI Std. Z39.18

UNIT CONVERSION TABLE
U.S. customary units to and from international units of measurement[*]

U.S. Customary Units	Multiply by → ← Divide by[†]		International Units
Length/Area/Volume			
inch (in)	2.54	$\times 10^{-2}$	meter (m)
foot (ft)	3.048	$\times 10^{-1}$	meter (m)
yard (yd)	9.144	$\times 10^{-1}$	meter (m)
mile (mi, international)	1.609 344	$\times 10^{3}$	meter (m)
mile (nmi, nautical, U.S.)	1.852	$\times 10^{3}$	meter (m)
barn (b)	1	$\times 10^{-28}$	square meter (m^2)
gallon (gal, U.S. liquid)	3.785 412	$\times 10^{-3}$	cubic meter (m^3)
cubic foot (ft^3)	2.831 685	$\times 10^{-2}$	cubic meter (m^3)
Mass/Density			
pound (lb)	4.535 924	$\times 10^{-1}$	kilogram (kg)
unified atomic mass unit (amu)	1.660 539	$\times 10^{-27}$	kilogram (kg)
pound-mass per cubic foot (lb ft^{-3})	1.601 846	$\times 10^{1}$	kilogram per cubic meter (kg m^{-3})
pound-force (lbf avoirdupois)	4.448 222		newton (N)
Energy/Work/Power			
electron volt (eV)	1.602 177	$\times 10^{-19}$	joule (J)
erg	1	$\times 10^{-7}$	joule (J)
kiloton (kt) (TNT equivalent)	4.184	$\times 10^{12}$	joule (J)
British thermal unit (Btu) (thermochemical)	1.054 350	$\times 10^{3}$	joule (J)
foot-pound-force (ft lbf)	1.355 818		joule (J)
calorie (cal) (thermochemical)	4.184		joule (J)
Pressure			
atmosphere (atm)	1.013 250	$\times 10^{5}$	pascal (Pa)
pound force per square inch (psi)	6.984 757	$\times 10^{3}$	pascal (Pa)
Temperature			
degree Fahrenheit (^{o}F)	[T(^{o}F) − 32]/1.8		degree Celsius (^{o}C)
degree Fahrenheit (^{o}F)	[T(^{o}F) + 459.67]/1.8		kelvin (K)
Radiation			
curie (Ci) [activity of radionuclides]	3.7	$\times 10^{10}$	per second (s^{-1}) [becquerel (Bq)]
roentgen (R) [air exposure]	2.579 760	$\times 10^{-4}$	coulomb per kilogram (C kg^{-1})
rad [absorbed dose]	1	$\times 10^{-2}$	joule per kilogram (J kg^{-1}) [gray (Gy)]
rem [equivalent and effective dose]	1	$\times 10^{-2}$	joule per kilogram (J kg^{-1}) [sievert (Sv)]

[*]Specific details regarding the implementation of SI units may be viewed at http://www.bipm.org/en/si/.
[†]Multiply the U.S. customary unit by the factor to get the international unit. Divide the international unit by the factor to get the U.S. customary unit.

2015-11-16

FINAL REPORT for HDTRA1-10-1-0118

Reaction Dynamics and Dispersion of Energetic Biocides

Proposal number:BRBAA08-Per2-B-2-0025

Michael R. Zachariah

Department of Mechanical Engineering and

Department of Chemistry and Biochemistry

University of Maryland – College Park;

www.enme.umd.edu/~mrz

mrz@umd.edu

301-505-4311

<u>**Reaction Dynamics and Dispersion of Energetic Biocides**</u>

I. ABSTRACT

The objectives of this project are to probe the reactive and dispersion characteristics of energetic biocides (EB). We will employ a new mass-spectrometric tool to probe reaction dynamics, employ bulk combustion studies, and post-combustion analysis to assess the dispersion characteristics of the biocidal agent.   Through these studies we hope to develop an understanding of the ignition and propagation of these EB systems and more specifically address the four primary goals.

- Basic scientific information on initiation temperature, reaction time, and temporal speciation of energetic biocides.

- Basic scientific information on initiation and propagation mechanisms

- Nature of biocidal dispersion and its relationship to combustion dynamics.

- Chemical and morphological state of biocide.

II. SCOPE.

This proposal is in support of the Basic and Applied Sciences Directorate and the JSTO and Biological-Agent Dynamics in Turbulent Reacting Flows (Thrust 4) topic.

A. OBJECTIVE

The objectives of this project are to probe the reactive and dispersion characteristics of energetic biocides (EB). We will employ a new mass-spectrometric tool to probe reaction dynamics, and we will employ post-combustion analysis to assess the dispersion characteristics of the biocidal agent.

III. Results for FY-11

1. Encapsulation of Perchlorate Salts within Metal Oxides

SUMMARY

High oxygen content strong oxidizer perchlorate salts were successfully incorporated into current nano-thermite composite formulations. The perchlorates were encapsulated within mild oxidizer particles through a series of thermal decomposition, melting, phase segregation and re-crystallization process occurred within confined aerosol droplets. This approach enables the use of hygroscopic materials by stabilizing them within a matrix. Several samples including $Fe_2O_3/KClO_4$, $CuO/KClO_4$ and Fe_2O_3/NH_4ClO_4

composite oxidizer particles have been created. The results show that these composite systems significantly outperform the single metal oxide system in both pressurization rate and peak pressure. The ignition temperatures for these mixtures are significantly lower as compared to the metal oxide alone, and time resolved mass spectrometry shows O_2 release from the oxidizer also occurs at a lower temperature and with high flux. The results are consistent with O_2 release as the controlling factor in determining the ignition temperature. High speed imaging clearly shows a much more violent reaction. The results suggest that a strategy of encapsulating a very strong oxidizer, which may not be environmentally compatible, within a more stable weak oxidizer offers the opportunity to both tune reactivity and to employ materials that previously would be prohibited.

1. Introduction

Nano-thermite, a subset of metastable intermolecular composites (MIC), is a relatively new class of energetic materials (EMs) that is finding applications in propellants and explosives, as well as microscale energetic material applications and microelectromechanical systems (MEMS) [1, 2]. These solid-state redox reaction systems have in common very rapid, exothermic and self-propagating behavior. With respect to traditional inorganic solid-state EMs, a mixture of fine powders of oxidizer and reducing agent, nano-thermite is characterized by nanoscale constituents that enable intimate mixing of the fuel and oxide, whose nano-dimension homogeneity results in substantial enhancement in heat and mass diffusion, and therefore reactivity and burn rate [3-5]. It has been experimentally observed that the activation energy for nanoaluminum oxidization and for the oxidizer decomposition is significantly lower than the corresponding values for their macroscopic counterparts [6], and the higher surface area presumably is at least partially responsible for the higher reaction rate and facilitates energy transfer [7]. Aumann et al. was one of the first to see the enhanced performance nano-energetic materials could potentially deliver, with a 1000 x increase in reactivity [8]. It has been speculated that this increases in reaction propagation rate is related to the mode of energy transfer in a composite, which likely shifts from conductive to convective mode [9-11]. These results have been confirmed by further studies by others who have shown that the packing density is inversely correlated with reaction velocity and that intimacy of mixing was a very key variable [12].

This latter point suggests that the manner of assembling the fuel and oxidizer either through physical mixing, or through direct assembly and microstructure manipulation may yield new and more controllable properties. This has lead to for example, self-assembled Al/Fe_2O_3 nanotubes [7], self-assembled Al/CuO nanorods [13, 14], nanowired Al/CuO [2, 15], electrostatically assembled Al/Fe_2O_3 nanoparticles [16], Al/SnO_2 coating by atomic layer deposition (ALD) [17].

While there are a wide variety of possible metal and oxidizer combinations for thermite mixtures, aluminum (Al) is most often the fuel choice, due to its availability, high reaction enthalpy, low ignition temperature, high thermal conductivity, and the passivation nature of its native oxide. Further the high negative enthalpy of the oxide of aluminum (Al_2O_3) offer many possible low cost metal oxides as possible oxidizers, including Fe_2O_3, CuO, MoO_3, Bi_2O_3, WO_3, and SnO_2, etc. [1, 18, 19].

3

On the other hand, one can envision many other more powerful oxidizer molecules. Many of these are typically composed of salts. For example ammonium perchlorate (AP) is a very labile species composed of the perchlorate ion ClO_4^- with chlorine in an oxidation state +7. The high oxygen content and good thermal stability of perchlorates have made them indispensible ingredients for the pyrotechnics industry and as key ingredient in solid rocket propellants. For example, composite solid rocket propellants typically contain 60-80 wt % ammonium perchlorate (AP) together with polymer binder (e.g. polybutadiene acrylic acid acrylonitril terpolymer (PBAN), hydroxyl-terminated polybutadiene (HTPB), nitramines, tetrazoles and nitrourethanes) and metallic fuel like aluminum powder [20]. In microscale MEMS application, the perchlorates such as $Ca(ClO_4)_2$, $KClO_4$ and $NaClO_4$ have been incorporated into nanoporous silicon by impregnation or vapor deposition technique [1, 21] Among the various perchlorate salts, AP is the most widely used today as it is characterized by high heat and high oxygen content. Potassium perchlorate (PP) is also a good solid propellant additive because of its fast burn rate and high caloric value.

Unfortunately, these oxidizers have not found application in MIC formulations, due to their highly hygroscopic nature which poses long term stability constraints on the nano-fuel (e.g. aluminum). Perchlorate release due to its water solubility has raised many environmental concerns during manufacture, transport and launch operations [22].

Ideally one would like to harness the oxidizer properties of perchlorates, with the longevity and stability offered by traditional metal oxides. In this paper we focus on developing a generic strategy of encapsulation of the strong oxidizer within a relatively mild and insoluble oxidizer. This strategy has previously been tested by us in the fabrication of a core-shell structured $Fe_2O_3/KMnO_4$ which showed enhanced performance characteristics [23]. In the current work, we have described a generic method for composite-structure oxidizer particles with several powerful oxidizer perchlorates being successfully encapsulated within common inorganic oxides such as Fe_2O_3 and CuO. The synthesis was realized via an aerosol-based spray drying/pyrolysis method, employing careful control of the precursor decomposition and melting processes. The aerosol technique enables formation of nano-sized perchlorate particles via a process of re-crystallization out of solution phase within an aerosol droplet, and simultaneous encapsulation of each perchlorate particle with an oxide shell, derived from the thermal decomposition of a metal nitrate precursor. The resulting materials are tested for their combustion behavior and compared with existing formulations.

2. Experimental section

2.1 Materials

Iron (III) nitrate nonahydrate ($Fe(NO_3)_3 \cdot 9H_2O$, > 98%), Cupric nitrate trihydrate ($Cu(NO_3)2 \cdot 3H_2O$, > 98%), ammonium perchlorate (NH_4ClO_4, 99.8%), potassium perchlorate ($KClO_4$, ≥ 99.5%), and reference CuO (~ 50 nm) and Fe_2O_3 (< 50 nm) nanopowders were all purchased from Sigma-Aldrich and were used as received. The aluminum nanopowders used in the combustion test were obtained from the Argonide Corporation which is designed as 50 nm ALEX by the supplier. The aluminum was found to be 70 wt% active as measured by thermogravimetric analysis (TGA).

2.2 Aerosol spray drying and pyrolysis

The composite oxidizer particles were fabricated via a one-step, two-furnace temperature strategy in an aerosol setup, the scheme of which is shown in Figure 1. Aerosol droplets containing the dissolved precursors were generated by a home built pressure atomizer. The geometric mean diameter of the generated droplet, as measured by a laser aerosol spectrometer, is about ≈1 μm. Droplets were passed through diffusion dryer to remove most of the solvent, and then to tube furnaces to thermally decompose the included precursor salts and further densify the particle structure. Normal residence times are ~1 second for a total gas flow rate of 3.5 L/min. Product particles were collected on a 0.4 μm pore Millipore HTTP membrane filter (housed in a stainless steel holder covered by a heating tape to prevent re-condensation of solvent vapor. Typical products yields exceed 50 %.

2.3 Thermite samples preparation

The MIC sample powders were prepared by first weighing out the fuel and oxidizer and adding the contents to a ceramic crucible. Approximately 10 mL of hexane was then added, and the mixture was sonicated in a common laboratory ultrasonicating bath for 20 min to ensure intimate mixing. The hexane was then allowed to dry in air and then the samples were placed in a furnace at 100 °C for a few minutes to drive off any remaining hexane. The powders were then very gently broken apart with a spatula until the consistency for each sample was that of a loose powder.

2.4 Simultaneous pressure and optical characterization of reactivity

The reactivity of MICs is typically reported as a relative value, due to the current lack of fundamental understanding of the reaction mechanism. Two common methods for measuring the reactivity of MICs are to combust the sample and measure the linear burning rate, and also to combust the material in a constant-volume cell and measure the pressurization rate. The flame velocity and pressurization rate have been shown to correlate with each other, however, the correlation is not quantitative. In this work, the pressurization rate from combustion in a small volume cell has been used to characterize the reactivity of the burning material. Since this is a relative measurement, a reference oxidizer (CuO) is shown with the data as a comparison.

In a typical pressurization rate measurement in our experiment, a fixed mass (25 mg) of the sample powder was placed inside a constant-volume (~ 13 mL) pressure cell, and a nichrome wire coupled to an external power supply was placed in contact with the top of the powder, serving as an ignition source through resistive heating of the wire. A piezoelectric pressure sensor was employed in series with an in-line charge amplifier and a signal conditioner, and the resultant voltage trace upon ignition was captured by a digital oscilloscope. The pressurization rate (dP/dt) was calculated by converting the voltage rise to pressure (1 mV = 0.237 psi), and dividing by the rise time in microseconds. Three repeated shots were performed for each sample for the average pressurization rate. The optical emission is simultaneously collected using a lens tube assembly, containing a plano–convex lens ($f = 50$ mm), and photodetector to collect the broadband emission.

2.5 Time resolved mass spectrometry measurement of the oxygen release of the oxidizers

The recently developed temperature-jump/time-of-flight mass spectrometer (T-Jump/TOFMS) was used to characterize the reactivity of the nanocomposites. Typically, the T-Jump filament (Pt wire, length ~ 12 mm, diameter ~ 76 um) was coated with a thin layer of sample powder (< 0.03 mg) which could be heated up to ~1800 K at a heating rate of ~ 5×10^5 K/s. The filament was replaced after each heating event. From the current and voltage trace, a resistivity measurement can be obtained and related to the instantaneous temperature of the filament, which can be mapped against the mass spectra. Time resolved mass spectra combined with temperature information were then used for characterization of nanocomposite thermite reactions. A detailed experimental description of T-Jump/TOFMS can be found in our previous papers [24-25].

2.6 Simultaneous fast-heated ignition wire test and high-speed imaging

The T-Jump technique was coupled with a photomultiplier tube (PMT) setup for the measurement of the optical emission. The ignition temperature of the thermite sample reaction is obtained from the correlated emission signal with temperature profile of the T-Jump filament. The experiments used the same T-Jump wire in the T-Jump/TOFMS except for those performed at atmospheric pressure. A detailed experimental description can be found in our previous papers [24, 25].

High-speed digital video imaging of sample burning was conducted with a Vision Research Phantom® v9.1 digital camera, which has maximum resolution of 1632 x 1200 and maximum frame rate of 153846 fps at 96 x 8 resolutions.

3. Results and discussion

3.1 Synthesis of $Fe_2O_3/KClO_4$, $CuO/KClO_4$ and Fe_2O_3/NH_4ClO_4 composite oxidizer

The microstructure control of the composite particles was realized by tuning temperatures of the two furnaces that govern the thermal decomposition of the metal nitrates and the melting of the perchlorate, respectively. In a typical synthesis (e.g. $Fe_2O_3/KClO_4$), a precursor aqueous solution of iron (III) nonahydrate and potassium perchlorate is sprayed into aerosol droplets by an atomizer. For the starting components, the molar ratio of Fe/K was fixed at 1:2, and the total salt precursor concentration is kept constant at 5.0 wt%. The temperature of first furnace (T_1) was set at 125 °C and the second (T_2) at 550 °C.

Before or just entering into the first furnace, water evaporation from the droplet drives the crystallization or precipitation of both iron nitrate and potassium perchlorate. Each aerosol droplet may be considered as a micro-reactor containing a solid mixture of the two starting component salts. In the first furnace, iron nitrate ($T_{decomp(Fe(NO3)3)} = 125$ °C) decomposes to form iron oxide while potassium perchlorate ($T_{m.p.(KClO4)} = 525$ °C) remains a solid. From TEM image in Figure 2 (left) one can clearly see the distinct core-shell morphology. This core-shell structure was confirmed by EDS line scan analysis (Figure 2, right) identifying the elemental profile of Fe, O, K, and Cl along the selected line across the particles. Quite clearly we have created a structure of a very strong oxidizer encapsulated within a weak oxidizer shell.

While the mechanism of formation is unknown, we can speculate on likely routes. In one case the drying droplet results in a homogeneously dispersed solid particle containing the two precursors.

In the first furnace thermal decomposition of the iron precursor leads to small iron oxide clusters within the solid $KClO_4$ matrix. As the temperature is raised to the melting point of $KClO_4$, i.e. in the second furnace, the solid matrix becomes molten and liquid-like. At this point the iron oxide clusters become mobile, and begin to aggregate and coalesce at the exterior of the aerosol particle due to surface tension forces. As the particles cool down, the molten $KClO_4$ re-crystallizes to form a solid core that is encapsulated by the exterior oxide shell.

A second possibility is that the core-shell structure is created during the drying process and before the chemistry is initiated resulting in a core-shell $KClO_4/Fe(NO_3)_3$ structure. However the perchlorate is about 80 times less soluble than the iron precursor (at room temperature), so one would expect that if this was occurring we would have the perchlorate on the outside, where the evaporation of the solvent would cause the local concentration of the solute to be highest leading to precipitation of the least soluble component first. In either case it is clear from the figures that the perchlorate is in the interior, that a near perfect phase separation has occurred, and that crystallization of the perchlorate causes the shell to take on a non-spherical shape.

In order to clarify the microstructure formation mechanism, we have conducted another similar experiment at lower temperatures i.e. $T_1/T_2 = 90/90$ °C, in which no decomposition of iron nitrate as well as melting of perchlorate could occur during the processes. Figure 3 exhibits the TEM image along with EDS of the derived particles. It is quite clear that a core-shell structure is formed during the drying/precipitation. But in this case considerably more iron can be found within the core of the particles and less potassium. This suggests that despite the lower solubility of the perchlorate there is during the droplet evaporation process a net phase separation process that creates the core-shell structure. Apparently heating the particle to create the oxide and then subsequently melt the perchlorate, serves to further drive the phase separation process.

The copper oxide/potassium perchlorate ($CuO/KClO_4$) composite structure shown in Figure 4, was obtained under condition of $T_1/T_2 = 400/550$ °C. As in the iron example, the choice of temperatures was governed by the decomposition and melting points. In this example as before, the nitrate has a much higher solubility than the perchlorate. While the structure is obviously core-shell, crystallization of the perchlorate has clearly been disrupted. Careful examination of the TEM image reveals small CuO crystallites dispersed throughout, which could result from the incomplete coalescence and aggregation of CuO primary particles from the molten $KClO_4$ matrix. Possibly this is due to that fact that in this case the reactor temperatures are very close to each other, due to the relatively high decomposition temperature of the copper precursor. So in this case the material can be best described as CuO rich shell composite.

The influence of phase segregation on morphology is even more prominent for the iron oxide/ammonium perchlorate (Fe_2O_3/NH_4ClO_4) system, which was experimentally achieved with $T_1/T_2 = 125/200$ °C and shown in Figure 5. EDS analysis indicates that the two components form a homogeneous hollow-shell. In this case both components are behaving similar to conditions seen for spray pyrolysis in which solvent evaporation from the droplet leads to a hollow structure. In our case the two solutes has solubilities that are similar (~ 6 time difference at room temperature).

3.2 Characterizations of combustion performance

The relative reactivity for stoichiometric (i.e. equivalence ratio $\phi = 1$) mixtures of nano-Al with the oxidizers was measured using the combustion cell. The pressure signals are shown for the various synthesized oxidizers in Figure 6 (a) along with CuO nanopowder (~ 50 nm, Sigma Aldrich) and Fe_2O_3 nanopowder (< 50 nm, Sigma Aldrich) as reference materials. What can be seen is that all systems show a fast pressure rise which occurs on the order of microseconds. From a close look in the range of 0~20 ms as shown by the inset, the perchlorate materials, however, exhibit much higher overpressures than the reference CuO (purple curve) and Fe_2O_3 (light blue curve, barely seen on this scale). Another qualitative comparison is with the Al/Bi_2O_3 system. Martirosyan et al. [26] demonstrated the highest pressure pulse for Al/Bi_2O_3 among reported thermite reactions, suggesting that the extraordinary high pressure results from evaporation of the combustion product bismuth (Bi) whose boiling point is lower than the maximum reaction temperature. A pressurization rate of up to 650 $GPa\ s^{-1}$ (~ 94.3 $psi/\mu s$) was shown in their study, which is considerably lower than that achieved in our materials, without considering the larger sample mass/cell volume ratio of their testing system (i.e. 500 mg/85 cm^3 vs 25 mg/13 cm^3). The peak pressure, rise time, and pressurization rate are summarized in Table 1.

The corresponding optical emission for the same systems is shown in Figure 6 (b). In this case, some obvious differences were seen for the various systems. The oxidizers containing CuO exhibited an intense optical rise and decay, whereas the oxidizers with Fe_2O_3 showed a much weaker optical signal with a prolonged "tail". In all cases, the timescale of optical emission was several hundred microseconds, much longer than the rise time of the pressure signal.

We have recently argued that the pressurization occurs as a result of rapid oxidizer decomposition to release gaseous species, which can occur well before significant optical emission can be measured [27]. In oxidizers like CuO and Fe_2O_3, the gas is largely O_2, however, the kinetics of the O_2 release differ due to the individual decomposition mechanisms. CuO can rapidly release O_2, whereas Fe_2O_3 cannot due to the formation of FeO, essentially trapping O_2 in the condensed phase. In the current work, the synthesized oxidizers show the same relative behavior as an Al/CuO thermite; a rapid pressure signal followed by a prolonged optical signal. Therefore, we argue that the perchlorates burn by similar mechanisms. The mixture ignites, and the exothermic reaction rapidly drives the decomposition of the oxidizer to pressurize the system, then the remainder of the fuel continues to burn in a pressurized, oxygenated environment. In the case of a perchlorate, several other gaseous species (K, Cl, N_2, etc.) can form during the decomposition, and the formation of these gaseous species can greatly enhance the peak pressure, while also aiding in the convective energy transport throughout the thermites.

Direct comparison of the combustion of Al/(CuO+$KClO_4$) and Al/(Fe_2O_3+$KClO_4$) shows that the CuO system has a higher pressurization rate by about a factor of two, consistent with the idea that CuO decomposition contributes to the pressurization more than Fe_2O_3 does [24]. Comparing the optical signals between the two systems, we see qualitative differences in the results. For the CuO system, the optical emission rises and falls, with a burn time (full width half max) of ~190 μs. In fact, both Al/CuO and Al/(CuO+$KClO_4$) have similar burning times, suggesting that in both cases the burning is rate-limited by the aluminum fuel. For the Fe_2O_3 system, however, the observed plateau in the optical emission suggests that the combustion is occurring in two steps. We speculate that some of the oxidizer in the Fe_2O_3 remains trapped as FeO, and thus the combustion ultimately is rate-limited by the oxidizer. The assignment of a burning time is somewhat

ambiguous due to the plateau seen in the optical emission; however, it is characteristically longer than the CuO systems.

The reactivity of the MIC mixture could be tailored by varying the constituent content in the composite oxidizer particles. In particular, the metal oxide was thickened by increasing the ratio of the metal oxide precursor during the process of aerosol synthesis. This was done for both $(CuO+KClO_4)$ and $(Fe_2O_3+KClO_4)$, and the pressure measurements are compared in Table 2. Not surprisingly, the pressurization rate decreases as the less reactive metal oxide is thickened, and provides a simple method for tuning the thermite reactivity.

Experiments were conducted at high heating rates ($\sim 5x10^5$ K/s) on 70 um diameter platinum wires to measure the ignition temperature of the thermites formulated with nanoaluminum and the synthesized composite oxidizer mixture. Based on the average of three repeated shots the measured ignition temperatures of $Al/(Fe_2O_3+KClO_4)$ and $Al/(CuO+KClO_4)$ thermite are 1105 K and 1087 K, respectively, which is significantly lower than that of their corresponding single metal oxide thermite, i.e. > 1500 K of Al/Fe_2O_3, > 1200 K of Al/CuO.

Figure 7 gives sequential snapshots of $Al/(Fe_2O_3+KClO_4)$ and $Al/(CuO+KClO_4)$ burning on a wire under fast heating captured by the high-speed digital camera. Both of the perchlorate-contained thermites show much more violent reaction than that of Al/CuO (commercial) as obviously seen from the images, indicating much faster energy release and pressurization rate.

Our previous work has shown that a clear correlation existed between O_2 release from the oxidizer and the overall reactivity of the formulated nano-thermite, i.e. high thermite reactivity can be reasonably attributed to the strong oxygen release of the oxidizer [24]. In this work, time-resolved mass spectrometry was conducted to study the O_2 release of the synthesized perchlorate-encapsulated composite oxidizer. O_2 peak intensity as a function of time obtained from flash heating along with a comparison of commercial Fe_2O_3 nanopowder and synthesized $(Fe_2O_3+KClO_4)$ were plotted and shown in Figure 8. Not surprisingly, much higher O_2 signal intensity from $(Fe_2O_3+KClO_4)$ than from commercial Fe_2O_3 nanopowder was observed. Clearly, quick release of abundant oxygen attributed to the high reactivity in current thermite. Further, the onset temperature of O_2 release from $(Fe_2O_3+KClO_4)$ (~1045 K) is much lower than that of commercial Fe_2O_3 nanopowder (~1524 K), but close to that of $KClO_4$ (~1070 K), suggesting the dominant source of O_2 is from the perchlorate. Similar results were also observed from $(CuO+KClO_4)$ and $(Fe_2O_3+NH_4ClO_4)$ samples, which further confirmed the O_2 origin.

4. Conclusion

Water soluble and hygroscopic perchlorate salts including $KClO_4$ and NH_4ClO_4 were successfully encapsulated by common metal oxides through an aerosol synthesis approach. The unique microstructures of the composite oxidizer particles were characterized and structure evolution mechanisms were discussed. Thermite samples formulated with nano-fuel and synthesized oxidizers show a higher pressurization rate and peak pressure, a lower ignition temperature and a faster and more intense O_2 release. High speed imaging clearly shows a much more violent reaction. The results imply that the use of a strategy of incorporating a very strong oxidizer within a milder oxidizer offer many advantages in controlling reactivity and enabling the use of a material

that for long term compatibility would not normally be considered.

References

[1] C. Rossi, K. Zhang, D. Estéve, P. Alphonse, P. Thailhades, C. Vahlas, J. Microelectromechanical Sys. 16 (2007) 919.
[2] M. Petrantoni, C. Rossi, V. Conédéra, D. Bourrier, P. Alphonse, C. Tenailleau, J. Phys. Chem. Solids 71 (2010) 80.
[3] K. B. Plantier, M. L. Pantoya, A. E. Gash, Combust. Flame 140 (2005) 299.
[4] S. Majumdar, G. B. Kaleb, I. G. Sharma, J. Alloy Compd. 394 (2005) 168.
[5] M. E. Brown, S. J. Taylor, M. J. Tribelhorn, Propell. Explos. Pyrotech. 23 (1998) 320.
[6] A. N. Pivkina, Y. V. Frolov, D. A. Ivanov, Combust. Explos. Shock Waves 43 (2007) 51.
[7] J. L. Cheng, H. H. Hng, H. Y. Ng, P. C. Soon, Y. W. Lee, J. Phys. Chem. Solids 71 (2010) 90.
[8] C. E. Aumann, G. L. Skofronick, J. A. Martin, J. Vac. Sci. Technol. B, Microelectron. Process. Phenom. 13 (1995) 1178.
[9] B. W. Asay, S. F. Son, J. R. Busse, D. M. Oschwald, Propell. Explos. Pyrotech. 29 (2004) 216.
[10] H. L. Berghout, S. F. Son, B. W. Asay, Proc. Combust. Inst. 28 (2000) 911.
[11] B. S. Bockmon, M. L. Pantoya, S. F. Son, B. W. Asay, J. T. Mang, J. Appl. Phys. 98 (2005) 064903.
[12] M. L. Pantoya, V. I. Levitas, J. J. Granier, J. B. Henderson, J. Propul. Power 25 (2009) 465.
 [13] S. Apperson, R. V. Shende, S. Subramanian, D. Tappmeyer, S. Gangopadhyay, Z. Chen, K. Gangopadhyay, P. Redner, S. Nicholich, D. Kapoor, Appl. Phys. Lett. 91 (2007) 243109.
[14] S. Subramaniam, S. Hasan, S. Bhattacharya, Y. Gao, S. Apperson, M. Hossain, R. V. Shende, S. Gangopadhyay, P. Redner, D. Kapoor, and S. Nicolich,Proc. Mater. Res. Soc. Symp. 896 (2006) 0896-H01-05.1.
[15] K. Zhang, C. Rossi, G. A. A. Rodriguez, C. Tenailleau, P. Alphonse, Appl. Phys. Lett. 91 (2007) 113117.
[16] S. H. Kim, M. R. Zachariah, Adv. Mater. 16 (2004) 1821.
[17] J. D. Ferguson, K. J. Buechler, A. W. Weimer, S. M. George, Powder Technol.156 (2005) 154.
[18] G. M. Dutro, R. A. Yetter, G. A. Risha, S. F. Son, Proc. Combust. Inst. 32 (2009) 1921.
[19] S. H. Fischer, M. C. Grubelich, Proc. 24th Int. Pyrotechnics Seminar, Monterey, CA, Jul. 1998, 1-6.
[20] S. Jain, M. S. Nandagopal, P. P. Singh, K. K. Radhakrishnan, B. Bhattacharya, Defense Sci. J. 59 (2009) 294.
[21] H. Laucht, H. Bartuch, D. Kovalev, Proc. 7th Int. Symp. Exhib. Sophisticated Car Occupant Safety Syst., 2004, 12–16.
[22] E. W. Fournier, B. B. Brady, J. Propul. Power, 21 (2005) 937.
[23] A. Prakash, A. V. McCormick, M. R. Zachariah, Nano Lett. 5 (2005) 1357.
[24] L. Zhou, N. Piekiel, S. Chowdhury, M.R. Zachariah, J. Phys. Chem. C. 114 (2010) 14269.
[25] L. Zhou, N. Piekiel, S. Chowdhury, M.R. Zachariah, Rapid Commun. Mass Spectrom.

23 (2009) 194

[26] K. S. Martirosyan, L. Wang, A. Vincent, D. Luss, Nanotechnol. 20 (2009) 405609.
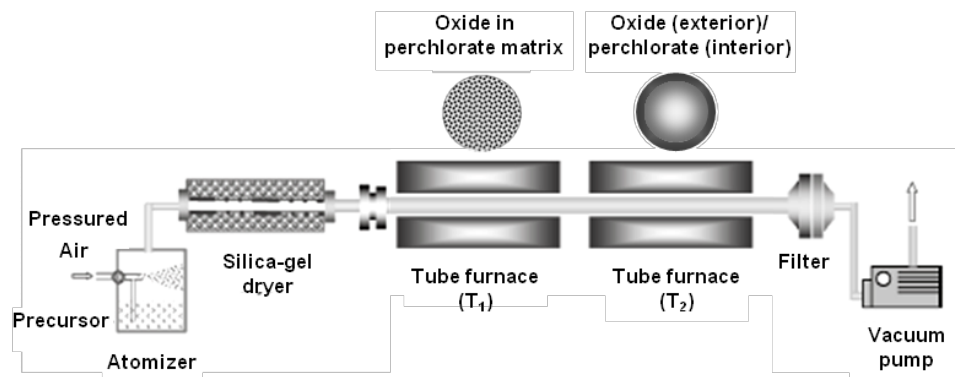[27] K. Sullivan, M. R. Zachariah, J. Propul. Power 26 (2010) 467.

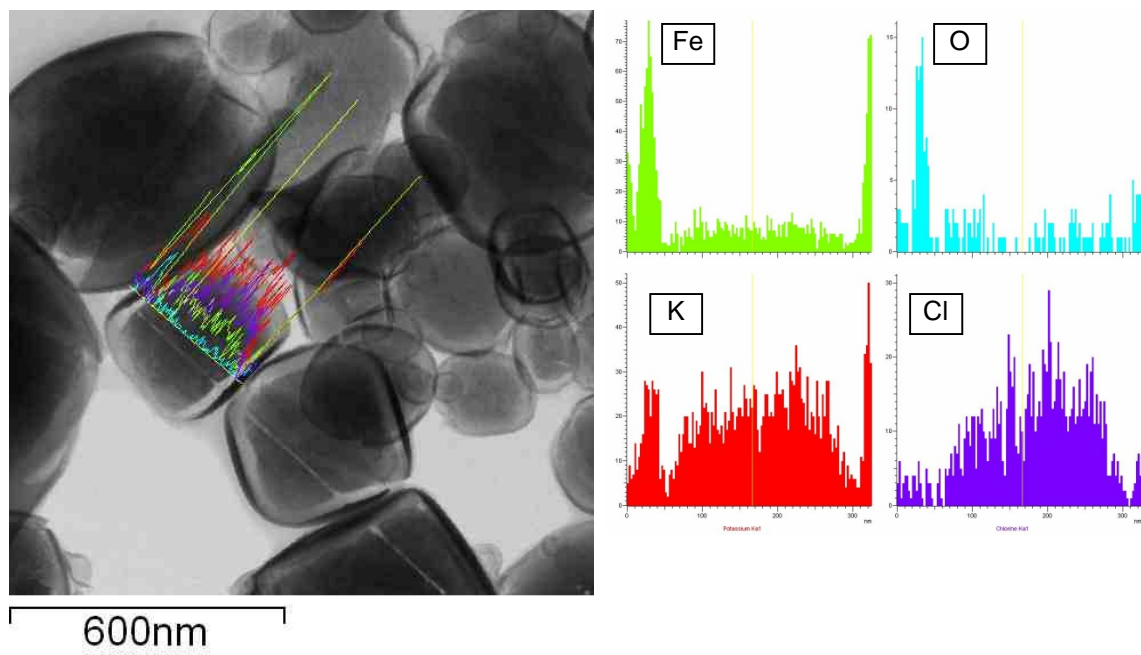Fig. 1. Aerosol spray drying/pyrolysis setup for the fabrication of composite oxidizer particles

Fig. 2. TEM image (left) and EDS line scan analysis (right) of the composite $Fe_2O_3/KClO_4$ particles, revealing elemental concentration profile of Fe, O, K and Cl across the line, [Fe/K] = ½ in precursor solution
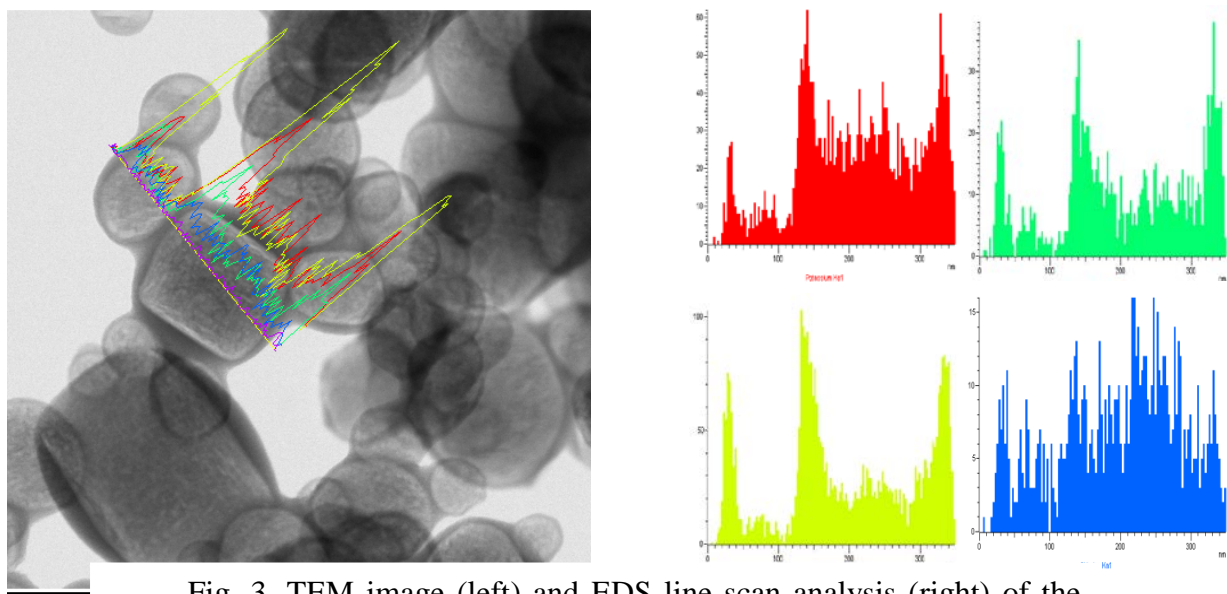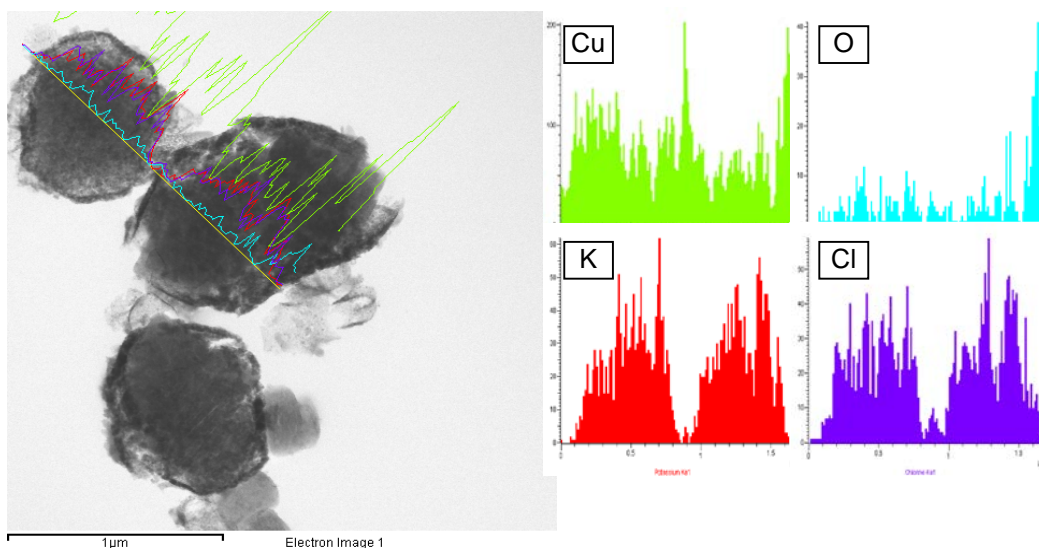

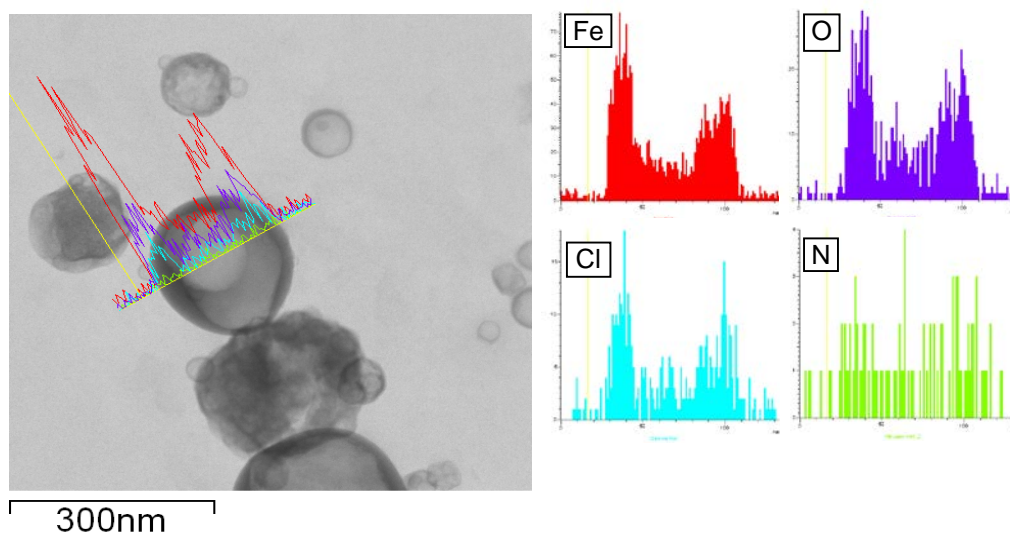Fig. 3. TEM image (left) and EDS line scan analysis (right) of the composite $Fe_2O_3/KClO_4$ particles obtained at T_1/T_2 = 90/90 °C

Fig. 4. TEM image (left) and EDS line scan analysis (right) of the composite CuO/KClO$_4$ particles, revealing elemental concentration profile of Cu, O, K and Cl across the line, [Cu/K] = ½ in precursor solution

Fig. 5. TEM image (left) and EDS line scan analysis (right) of the composite Fe$_2$O$_3$/NH$_4$ClO$_4$ particles, revealing elemental concentration profile of Fe, O, N and Cl across the line, [Fe/N] = ½ in precursor solution

Oxidizer (w/Al, $\phi = 1$)	P_{max} (*psi*)	Rise Time (μs)	Pressurization Rate (*psi/μs*)
(CuO+KClO$_4$)	534	1.5	356
(Fe$_2$O$_3$+KClO$_4$)	495	2.4	206
(Fe$_2$O$_3$+NH$_4$ClO$_4$)	389	3.3	117
CuO (ref.)	98	10.4	9.4
Fe$_2$O$_3$ (ref.)	13	800	0.017

Table 1. Measurements of the peak pressure and rise time for thermites prepared with the perchlorate-included systems relative to commercially available CuO. The pressurization rate is an accepted indicator of relative reactivity, and the results show a large enhancement in the reactivity for all synthesized oxidizers. All oxidizers were mixed with Al, and were prepared stoichiometrically assuming complete conversion to Al$_2$O$_3$. The elemental molar ratio in the synthesized oxidizers is [Cu/K] = [Fe/K] = [Fe/N] = 1/2. Typically a 25 mg sample was loaded in a 13 mL cell for the measurement.

Oxidizer (w/Al, $\phi = 1$)	Molar ratio	P_{max} (*psi*)	Pressurization Rate (*psi/μs*)
(CuO+KClO$_4$)	[Cu/K] = 1/2	534	356
	[Cu/K] = 2/1	279	112
(Fe$_2$O$_3$+KClO$_4$)	[Fe/K] = 1/2	495	206
	[Fe/K] = 2/1	240	97

Table 2. Effect of changing the relative amount of metal oxide/perchlorate onthermite reactivity. Typically a 25 mg sample was loaded in a 13 mL cell for the measurement.
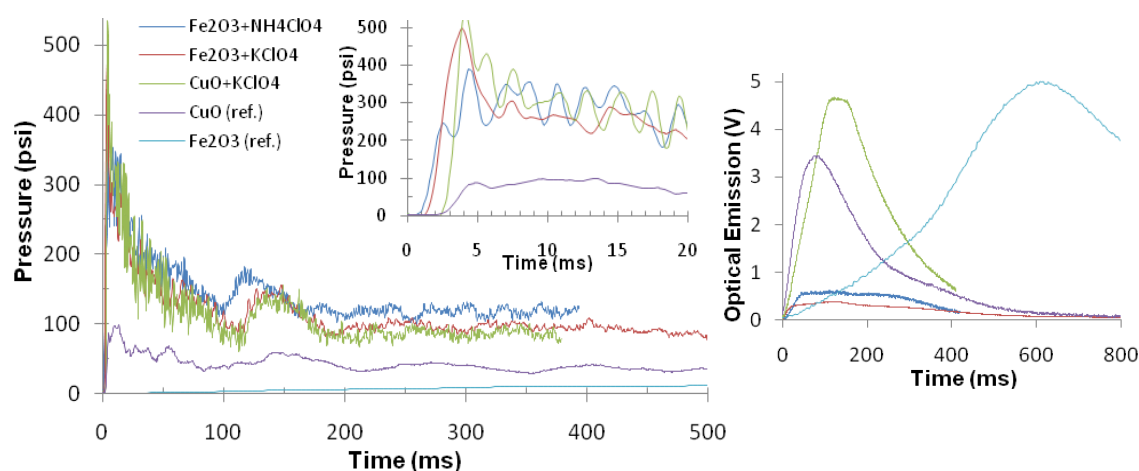
Fig. 6. Simultaneous pressure (a) and optical (b) traces for various thermites as measured during combustion in a constant-volume pressure cell. Inset of left is magnified part between 0-20 ms. All pressure traces showed a rapid rise, with the synthesized perchlorate-included oxidizers significantly outperforming reference CuO and Fe_2O_3. The optical traces for CuO-containing mixtures showed an intense rise to a peak, followed by decay. The Fe_2O_3-containing mixtures, on the other hand, exhibited less intense optical signals, and a "tail" lasting several hundred microseconds. All thermites were weighed stoichiometrically, assuming complete conversion to Al_2O_3. The elemental molar ratio in the synthesized oxidizers is [Cu/K] = [Fe/K] = [Fe/N] = 1/2.
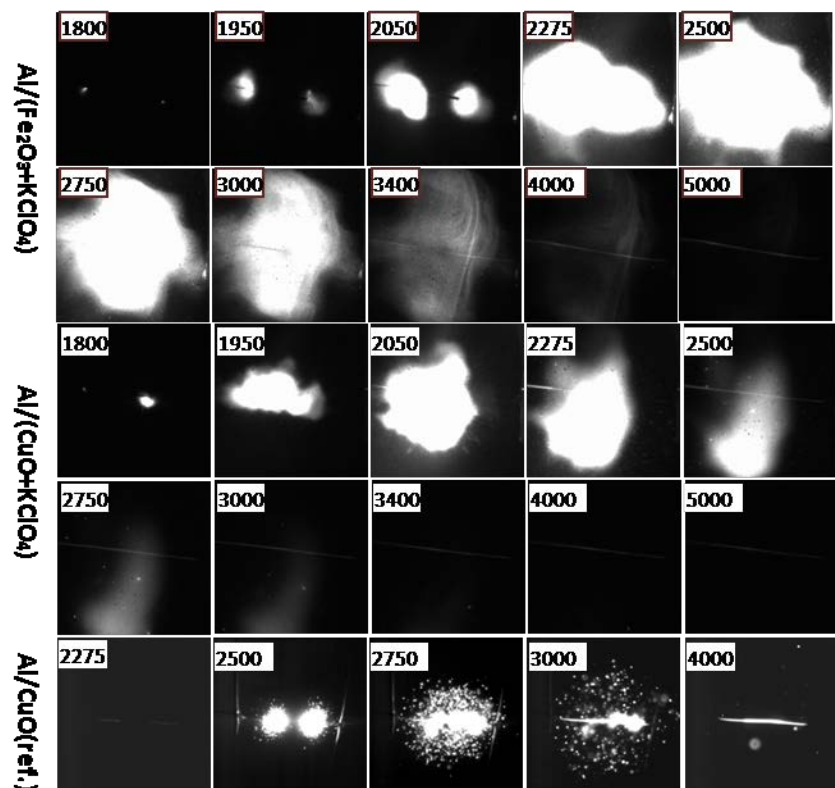

15

Fig. 7. Sequential snapshots of Al/(Fe₂O₃+KClO₄), Al/(CuO+KClO₄) and Al/CuO (commercial) burning on fast-heating wire that is captured by the high-speed video camera. The labeled numbers are time elapsed (μs) after triggering

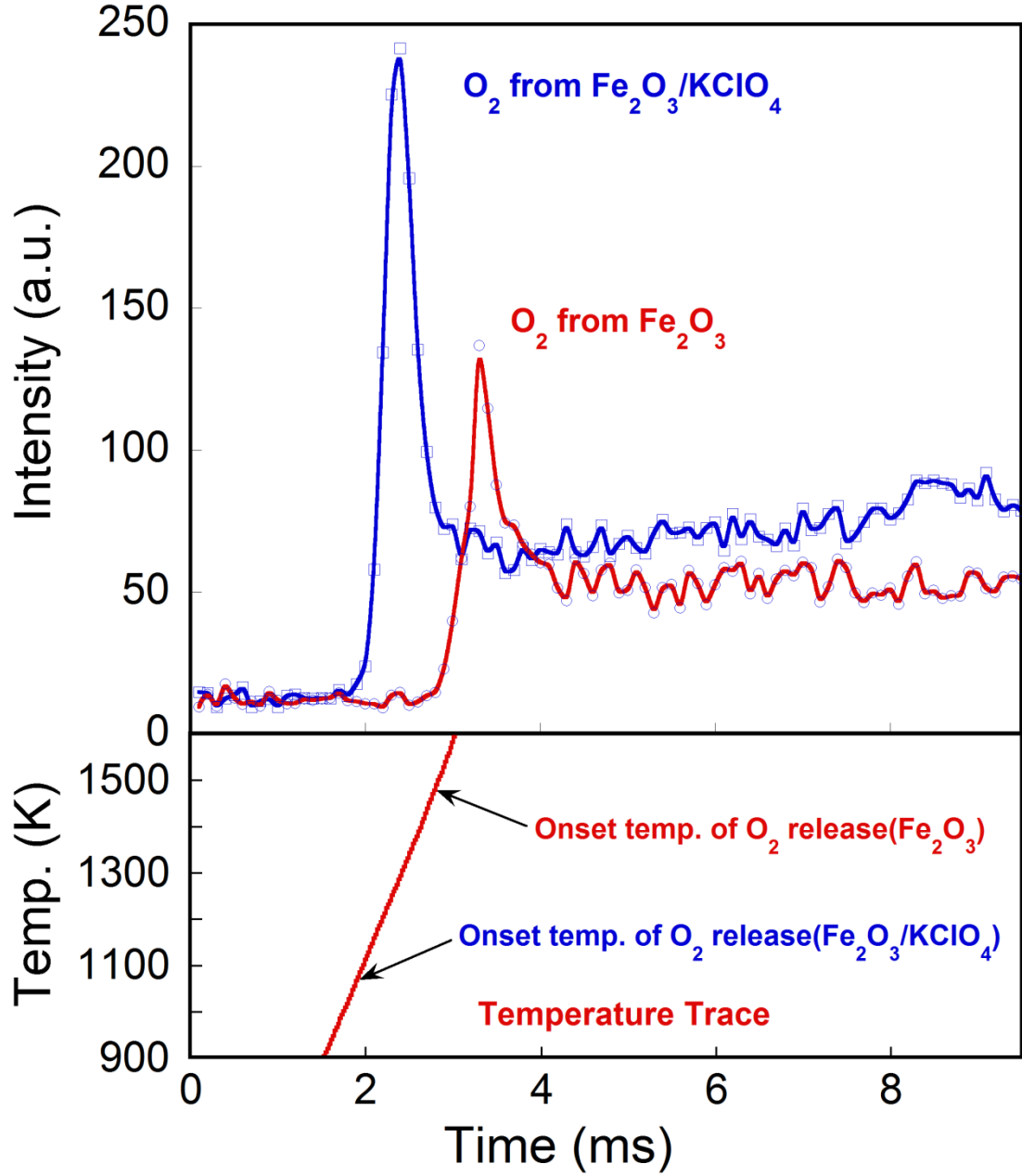Fig. 8. Temporal profile of oxygen releases upon heating of the synthesized composite oxidizer (Fe₂O₃+KClO₄) and commercial Fe₂O₃ nanopowder. The heating pulse time is 3.0 ms.

2. Synthesis and reactivity of nano-Ag$_2$O as an oxidizer

SUMMARY

We investigated Ag$_2$O as a potential oxidizer in antimicrobial energetic systems. Ultrafine Ag$_2$O was synthesized, and its performance in nanoaluminum-based thermite systems was evaluated using a constant volume combustion cell. The Ag$_2$O alone was found to be a relatively poor oxidizer, but it performed well when blended with more reactive oxidizers, CuO and AgIO$_3$. Time resolved mass spectrometry was used to investigate the reaction mechanism in more detail. Post-reaction analysis confirmed the production of Ag, but it was seen to exist in a matrix with Cu in the Al/CuO/Ag$_2$O ternary system. The product in surface contact with Al$_2$O$_3$ suggested a reactive sintering mechanism occurred. The results indicate that Ag$_2$O, while a poor oxidizer itself, can be integrated into more reactive systems to produce high yields of biocidal silver. The morphology of the final product, however, indicates that a large amount of the silver may not be surface-exposed, a result which would negatively impact the biocidal activity.

Introduction

We have recently investigated the combustion performance and product morphology of silver iodate (AgIO$_3$), a particularly attractive candidate because of its low solubility in water.[5] The ignition temperature was measured using a rapidly heated Pt wire, and the combustion behavior was evaluated using a time of flight mass spectrometer,[6] along with a constant volume combustion cell. X-ray diffraction confirmed that the major reaction product was AgI, and not elemental silver and iodine. While AgI has been used as an antiseptic,[7] at this time there are few studies comparing its efficacy relative to elemental silver and iodine.

Silver has been shown to exhibit antimicrobial characteristics in many forms and at room temperature.[8] As the particle size is reduced and the surface to volume ratio increases, so does the potency of the Ag to bacteria.[9] Also, the presence of an oxide shell has been shown to increase the biocidal activity of silver.[10] The authors claim that silver ions are the actual biocidal species, and a thin oxide shell can promote the release of Ag$^+$ to the environment. This sort of behavior may be analogous to what was recently observed for nano-Al with an oxide shell, where molecular dynamics simulation showed that built in electric fields can serve to facilitate the diffusion of Al ions through the shell.[11]

A comparison of several silver-based oxidizers is shown in Table 1, along with the theoretically predicted maximum amount of elemental silver produced per gram of mixture. Note that the values of produced silver are given as a theoretical maximum, and will actually be lower if any recombination can occur (as is the case for AgIO$_3$, where the product is largely AgI). From Table 1, it can be seen that Ag$_2$O has the highest potential for elemental silver production (86% conversion by mass) out of any other silver-based oxidizer. However, its performance as an oxidizer in antimicrobial energetic thermite systems needs to be examined.

In this investigation, ultrafine Ag$_2$O (<20 nm, measured by TEM) was synthesized by a wet chemical process, and evaluated as an oxidizer in energetic thermite systems, with nanoaluminum as the fuel. The combustion performance and reaction products of binary Al/Ag$_2$O mixtures, along with ternary mixtures of Al/AgIO$_3$/Ag$_2$O and Al/CuO/Ag$_2$O, were investigated as a function of Ag$_2$O loading. AgIO$_3$ was chosen because it performs very well in combustion tests, and also

because its major product, AgI, is likely biocidal in nature. CuO was chosen because it is a relatively good oxidizer, but also because of the higher boiling point of Cu (2840 ^{0}K) relative to Ag (2436 ^{0}K). From a design standpoint, this is an important consideration due to the possible formation of core-shell structures governed by the relevant vaporization temperatures. While a variety of oxidizers could potentially enhance the combustion, an oxidizer such as Bi_2O_3 may be a poor choice due to the low boiling point (1833 ^{0}K) of bismuth compared to the boiling point of silver. Upon cooling, a significant amount of Bi may heterogeneously condense onto Ag, rendering an undesirable Ag core/Bi shell morphology. For CuO, if heterogeneous condensation occurs, then at least in this case we would expect the silver to condense onto copper, an acceptable morphology with the silver product exposed to the environment. With these ideas in mind, there are other oxidizers which may give similar results, however, the thermophysical properties should be considered when making this choice.

Experimental Methods

Materials

The nanoaluminum, termed "50 nm ALEX," was purchased from the Argonide Corporation. The average particle diameter was 50 nm, as specified by the supplier, and TGA showed the aluminum to be 70% elemental by mass. The copper oxide used in this work was purchased from Sigma Aldrich, and has an average particle diameter of <50 nm as specified by the supplier. The nanoscale $AgIO_3$ was synthesized at the Naval Air Warfare Center Weapons Division (NAWCWD) by precipitation from aqueous solutions of silver nitrate and potassium iodate or sodium iodate, using a modification of a literature method.[12] The morphology of the as-produced $AgIO_3$ were thin platelets, with the specific surface area measured to be 4.0 m^2/g, corresponding to a spherical particle diameter of 270 nm. More information on the method and characterization can be found in a separate work.[5]

The nano-scale Ag_2O was synthesized through a wet chemical technique. A 0.005 M silver nitrate ($AgNO_3$, >99% purity, Sigma Aldrich) aqueous solution was prepared, and 80 mL was heated to 60 ^{0}C. 20 mL of a 0.025 M sodium hydroxide (NaOH, >98%, anhydrous, Sigma Aldrich) aqueous solution was added drop-wise, while the solution was constantly stirred with a magnetic stir bar, until the solution had the consistency of a grey-yellow colloidal suspension. The reaction of silver nitrate with sodium hydroxide produces silver hydroxide via the following mechanism:

$$AgNO_3 + NaOH \rightarrow AgOH + Na^+ + NO_3^-$$
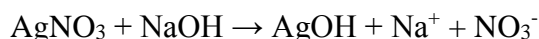
The intermediate AgOH is thermodynamically unstable, and ultimately produces Ag_2O through the following recombination process:

$$2AgOH \rightarrow Ag_2O + H_2O \ (pK = 2.875)$$
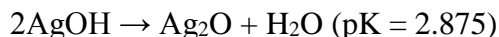
The solution was kept at 60 ^{0}C for two hours to ensure complete reaction. The particles were then collected in 3-4 cycles of a centrifuge/re-dispersion washing process using ethanol, and the solution was allowed to dry, leaving behind the brown Ag_2O particles. A transmission electron microscope image of the as-produced Ag_2O is shown below in Figure 1. As can be seen, the majority of the primary particles are spherical with diameters <20 nm. The particles have a relatively narrow size distribution, however, are found to be highly agglomerated into much larger structures. X-Ray diffraction (XRD) data for the sample is shown in Figure 2, and confirms the synthesized material to be Ag_2O.

The thermite samples were prepared by adding the fuel and oxidizer powders either to a

ceramic crucible or glass vial with a few mL of hexane, and ultrasonicated for ~20-30 min to ensure substantial mixing. For combustion cell tests, the hexane was allowed to evaporate until the samples were completely dry. The loose powder was then very gently broken up using a spatula to remove the larger clumps and make the consistency more homogeneous. To prepare samples for the wire studies, the dispersion was pipetted onto the wire, and the hexane was then allowed to dry before heating began. All mixtures were prepared stoichiometrically assuming complete conversion to Al_2O_3. For the ternary $Al/AgIO_3/Ag_2O$ and $Al/CuO/Ag_2O$ mixtures, the samples are referred to in terms of the Wt% of Ag_2O in the oxidizer.

Measurement of Reactivity

A fixed mass of 25 mg was loaded into a sample holder and combusted inside a constant volume pressure cell (~13 cc). The cell was originally used to only measure the transient pressure signal,[2b] and was later modified to simultaneously collect the optical emission though a series of lenses coupled to a high-speed photodetector.[1b] The transient optical emission and pressure signals are captured during the burning via an oscilloscope, and both can be used to draw conclusions about the combustion behavior. The pressurization rate (peak to peak pressure divided by the pressure rise time) is calculated and is used as a measurement of the system reactivity,[2c] and the burn time is assigned to be the full width of the optical signal at half maximum. Neither of these measurements is intended to be absolute, instead, the focus is to investigate the trends in the measurements as a parametric study (i.e. mass loading of Ag_2O). From the observed trends, conclusions may be drawn about the relative reactivity and mechanisms as a function of the changing parameter.

Certain samples were also investigated using a custom time-of-flight mass spectrometer (TOFMS). Thermite samples were directly pipetted onto a thin Pt wire. The wire is then supplied a tunable current pulse, and undergoes Ohmic heating at rapid heating rates (T_{max} ~2000 K at ~$5x10^5$ K/s). A series of mass spectra is collected every 100 µs to resolve transient speciation during the decomposition or chemical reaction. The details of this setup can be found elsewhere.[6]

Post-Reaction Analysis

The reacted sample was collected after combustion in the pressure cell, and was analyzed using various techniques. X-ray diffraction (XRD, Bruker C2 Discover with GADDS, operating at 40 kV and 40 mA with unfiltered Cu Kα radiation, $\lambda = 1.5406$ Å) was used to determine the crystalline species produced during the reaction. Transmission electron microscopy (TEM, JEOL 2100F) coupled with energy dispersive x-ray spectroscopy (EDS, Oxford INCA 250) was used to analyze the product and determine the morphology of the silver in the product. X-ray photoelectron spectroscopy (XPS) data was collected using a Kratos Axis 165 system operating in hybrid mode, with monochromatic aluminum x-rays (1486.5 eV). Survey spectra and high resolution spectra were collected with pass energies of 160 eV and 20 eV respectively. Samples were mounted on double sided carbon tape, charge neutralization was require to minimize sample charging, all peaks were calibrated to the adventitious hydrocarbon peak at 284.8 eV.

Results and Discussion

Combustion Performance

The pressure cell results for each binary thermite system are shown in Table 2. The $AgIO_3$ significantly outperforms both oxidizers, and we have recently argued that this is largely attributed to iodine gas release during the decomposition of the oxidizer.[13] The Al/Ag_2O system performed very poorly in pressurization rate when compared to a relatively common and reactive thermite, Al/CuO. The reason for this is somewhat of an anomaly when one looks at the thermodynamic predictions of both systems. A comparison of thermodynamic equilibrium predictions for Al/CuO and Al/Ag_2O thermites is shown in Table 3. The calculations are constant HP equilibrium calculations assuming phase changes.[14] Both systems are predicted to produce a relatively large amount of equilibrium gas (mostly comprised of the metal, Cu or Ag), and both systems are comparable in terms of the density. However, the Al/Ag_2O was found to react poorly, while the Al/CuO system reacts violently.

We have recently argued that the oxidizer decomposition is primarily responsible for pressurizing the system if the oxidizer can be decomposed efficiently, and on a timescale faster than the burn time of the fuel.[1b] According to the ICT Database of Thermochemical Values, Ag_2O has an enthalpy of formation of -31 kJ/mol and a decomposition temperature of 523 ^{0}K. In comparison, CuO has an enthalpy of formation of -156 kJ/mol, and calculations using NASA CEA predict it to start decomposing ~1100 ^{0}K at atmospheric pressure. From these thermodynamic considerations, we would expect Ag_2O to decompose similarly, if not more readily than CuO, as its decomposition is less endothermic and occurs at a relatively low temperature.

To further examine the relative difference between Ag_2O and CuO as oxidizers, we turn to the TOFMS results. The O_2 release profile is shown for the binary thermites Al/CuO and Al/Ag_2O in Figure 4. What can be seen is that the relative intensity of O_2 release is similar, if not higher, for Al/Ag_2O than it is for Al/CuO. It can also be seen that the onset of O_2 release occurs earlier (at a lower T) in the Al/Ag_2O system than it does for Al/CuO. These results are consistent with the thermodynamic considerations, where Ag_2O has a lower enthalpy of formation and decomposition temperature than CuO. The results also again raise questions about why Al/Ag_2O reacts so poorly, yet Al/CuO reacts very violently. If the O_2 release rate can be used as a relative measurement of the reactivity, then this analysis alone would suggest Ag_2O to be a better oxidizer than CuO.

From Table 3, the only thing that does stand out between the two thermite systems is the difference in the adiabatic flame temperature. These temperatures are 2843 ^{0}K and 2436 ^{0}K for Al/CuO and Al/Ag_2O, respectively. While everything else seems similar for the two systems, it's possible that the lower adiabatic flame temperature of Al/Ag_2O results in something mechanistically different in its burning. In fact, the temperature is much closer to the melting temperature of Al_2O_3 (2327 ^{0}K), and the inability to rapidly melt Al_2O_3 could negatively impact the reactivity for several reasons, including:

1)   Nanoaluminum is naturally passivated by a few nm thick Al_2O_3 shell,[15,16] and the phase of the shell may greatly affect the outwards mass transport rate of Al. This assumes a diffusion-based reaction mechanism occurs for nanoaluminum.[16,17,11]
2)   If the temperature is too low that the oxide product is solid instead of molten, it provides a substantial diffusion barrier between the fuel and oxidizer which increases in thickness as the reaction proceeds.
The reacted Al/Ag_2O was collected from the combustion cell and examined with XRD, the results of which are shown in Figure 3. It can be seen that there is some residual Ag_2O detected in the product, indicating that the reaction was not vigorous enough to fully decompose the Ag_2O. One major difference between the combustion cell and the TOFMS results is that in the combustion cell, energy propagation through the powder plays a much more important role, since a relatively large mass is being combusted. In other words, the intrinsic reactivity between Al and Ag_2O may be good when sufficiently heated, based on the O_2 release results using the TOFMS. However, if the reactivity does not provide rapid energy transport to further melt/decompose unreacted

particles, the self-propagating reaction will be severely hindered, and may even quench.

Next we look at ternary thermite systems consisting of nano-Al and blends of Ag_2O with more reactive oxidizers, $AgIO_3$ and CuO. The pressurization rates of the ternary systems are presented in Figure 5. All data has been normalized by the pressurization rate of the corresponding binary systems, $Al/AgIO_3$ and the Al/CuO, in order to discuss the relative performance. For the $Al/AgIO_3/Ag_2O$ system, the pressurization rate decreased steadily as Ag_2O was added. Above 45 Wt% Ag_2O, there was a very sudden and sharp drop in the pressurization rate, likely indicating a change in the reaction mechanism. For the $Al/CuO/Ag_2O$ system, the pressurization behavior remained relatively unchanged until >70 Wt% Ag_2O, and even then did not exhibit a sharp drop off in reactivity, instead it steadily decreases until >95 Wt% Ag_2O. Even at 87 Wt% Ag_2O, the pressurization rate had only decreased by a factor of two, and this is likely an insignificant tradeoff when one considers the primary motivation of increasing the silver production yield in thermite systems.

Next we look at the measured burning times, which are shown for the two ternary systems as a function of mass loading of Ag_2O in Figure 6. What can be seen is that the burn time stays relatively constant as Ag_2O is added to both systems. Above 45% in the $Al/AgIO_3/Ag_2O$ system there is a sudden and sharp increase in the burning time, and this is also the point where the pressurization rate was found to decrease suddenly. For the $Al/CuO/Ag_2O$ thermite the burn time remains relatively constant over the entire range of added Ag_2O, and does not increase suddenly until the oxidizer is 100% Ag_2O.

The pressurization rate and burn time measurements show that Ag_2O can display good reactivity, but only when blended with other oxidizers. Several of the species which may be of interest (i.e. AgI and AgO) are currently not contained within the thermodynamic product library of the NASA CEA code, and therefore equilibrium calculations are not included. However, adding both $AgIO_3$ and CuO will serve to increase the adiabatic flame temperature over that of Al/Ag_2O, and apparently even a slight increase in temperature can significantly enhance the performance of Ag_2O. This is especially clear in the $Al/Ag_2O/CuO$ system, where the reactivity is increased orders of magnitude relative to Al/Ag_2O when a mere 5 Wt% of CuO (95% Ag_2O) is added. The results are consistent with both the thermodynamic predictions and TOFMS results, which suggest CuO and Ag_2O should behave mechanistically similar. The exact reason why the binary Al/Ag_2O reacts so poorly will remain an open question, however, we speculate that it is due to the proximity of the reaction temperature to the melting point of Al_2O_3, as was previously discussed.

Post-Reaction Analysis

The reacted product was collected for each sample and studied using XRD to determine the crystalline product species. The diffraction patterns for the $Al/AgIO_3/Ag_2O$ system are shown in Figure 7. As can be seen, the strongest peak of Ag at $2\theta = 38.15$ ° from the ($1\bar{1}1$) plane increases with the mass loading of Ag_2O, while the strongest peak of AgI at $2\theta = 23.81$ ° from (111) plane decreases. Above 40% the relative intensity of both peaks drops off, and this behavior is likely due to the change in mechanism, experimentally seen as the sharp drop-off in reactivity from the pressure cell data. The XRD data for the $Al/CuO/Ag_2O$ system is shown in Figure 8. The Ag peaks are all present, however, only trace amounts of crystalline Cu were detected in the product relative to the amount of Ag which was formed. It's possible that some of the reduced copper can reoxidize with the air in the pressure cell to form an amorphous product, whereas the silver does not readily re-oxidize. It can also be seen that no apparent trend in the intensity of the Ag peaks was observed with increased mass loading of Ag_2O. While this could simply be due to differing sample sizes used in the XRD, it's a somewhat curious observation. XPS was also performed on select samples from each ternary system, and confirmed the production of surface-exposed Ag.

Details of the analysis are included as an appendix.

A small amount of the reacted product was collected and investigated with a TEM. The Al/Ag_2O/$AgIO_3$ is not included, since EDS could not easily distinguish between elemental Ag and AgI. Also, significant morphological changes were induced by the electron beam, thus making imaging and elemental analysis nearly impossible. Since AgI is considered a biocidal species itself, identifying its relative position to Ag is of less importance than looking at a non-biocidal species, such as Cu relative to Ag. Therefore, only results for Al/Ag_2O/CuO are shown. The sample chosen to investigate was 74 Wt% Ag_2O, which corresponds to the maximum amount of Ag_2O which resulted in no loss to the reactivity (see Figure 5). A TEM image, along with corresponding elemental maps is shown in Figure 9.

What can clearly be seen is that the produced Ag/Cu is in surface contact with a product containing Al and O. The Ag and Cu positions are found to almost entirely overlap. It's not likely that alloying reactions between the two have occurred, since no new XRD peaks were observed, so it is speculated that the morphology is a matrix of elemental silver and Cu which has intermixed. What can also be seen is that the large aggregated nanoparticles (<20 nm diameter, see Figure 1) have completely sintered in to characteristically larger and more uniform structures in surface contact. To further characterize the observed morphologies, an elemental linescan was performed and is shown in Figure 10. The linescan shows that the lighter material corresponds to Al and O, whereas the dark material is a mix of both Ag and Cu. It is very clear that the fuel and oxidizer have come into surface contact during the reaction to produce the product. The results suggest that a reactive sintering mechanism had occurred.[18] In a reactive sintering mechanism, the reaction occurs at the interface between fuel and oxidizer. As energy is liberated from the exothermic reaction, material is further melted and rapidly delivered to the interface where it continues to react. In this case, the molten Ag and Cu produced during the reaction are perhaps miscible, and this could explain the coexistence.

Although the TEM results are interesting from a mechanistic point of view, the implications are negative for biocidal applications. If the fuel and oxidizer create a product which is in surface contact, then a large amount of the produced Ag will not be exposed to the environment post reaction. While CuO ternary systems can help to increase the reactivity of Ag_2O up to very high mass loadings of Ag_2O, the Ag/Cu matrix which forms also will greatly reduce the exposed surface area. If a reactive sintering mechanism, or any other large amount of sintering is indeed occurring, the elemental silver will not maintain the high surface to volume ratio characteristic of the initial Ag_2O, and will form much larger structures. While all of these points will lead to reduced overall surface area of the produced Ag, the real question for ternary systems will be whether the enhanced reactivity and high-yield of elemental Ag outweighs the negative effects, and only further experimental testing can resolve this.

Conclusion

Ultrafine Ag_2O powder was synthesized by a wet chemical technique and mixed with nano-Al to form energetic thermite systems designed to produce high yields of antimicrobial silver as a combustion product. The loose powders were combusted in a constant volume pressure cell, where both the transient pressure and optical emission are monitored to investigate performance. Ag_2O itself was found to perform poorly in terms of pressurization rate and burn time, but performed well when combined with two more reactive oxidizers, $AgIO_3$ and CuO. In-situ time of flight mass spectrometry was used to investigate mechanistic differences between Al/Ag_2O and Al/CuO, and the two were found to behave similarly in that they both released a large amount of O_2 gas at a comparable rate. It is suggested that the low reaction temperature of Al/Ag_2O, which is close to the melting point of Al_2O_3, may primarily be responsible for its poor reactivity. A small amount

of CuO, however, can raise the temperature enough for Ag_2O to react violently, as was seen in the ternary system. The relative pressurization rates for both ternary systems were measured. For the $Al/AgIO_3/Ag_2O$ system, the reactivity dropped off fairly linearly as the mass loading of Ag_2O increased, followed by a sharp drop above 45 Wt%. The pressurization rate remained virtually unchanged as the Ag_2O loading was increased in an $Al/CuO/Ag_2O$ system, and had only dropped by about a factor of two when the loading was 87 Wt%. This suggested that Ag_2O can behave mechanistically similar to CuO, and thus the yield of elemental silver produced during the reaction can be dramatically increased with little loss in combustion performance. Ex-situ x-ray diffraction (XRD), x-ray photoelectron spectroscopy (XPS), and transmission electron microscopy (TEM) were performed to characterize select formulations. XRD confirms the production of crystalline silver, and XPS also detected elemental silver, indicating some amount of the silver was surface-exposed. TEM, however, showed large amounts of the silver product was in surface contact with Al_2O_3, and also was trapped within a matrix of Cu for the $Al/CuO/Ag_2O$ ternary system. It is speculated that a reactive sintering mechanism occurs, and large amounts of the product are sintered into characteristically larger particles. High-yields of elemental silver can thus be produced in highly reactive ternary formulations, however, the TEM results suggest several factors which could potentially decrease the biocidal efficacy, due to the formation of undesired morphologies which ultimately prevent the silver from being exposed to the environment.

Table 1: Various silver-containing oxidizers and the maximum calculated silver production in stoichiometric thermite mixtures with aluminum. Note that the calculations assume no recombination (i.e. Ag + 0.5I$_2$ → AgI) and therefore may overestimate the mass production of silver depending on the extent of recombination.

Oxidizer	Stoichiometric Reaction (assuming no recombination)	grams Ag produced (max) / gram thermite
Ag$_2$O	2Al + 3Ag$_2$O → Al$_2$O$_3$ + 6Ag	0.86
AgO	2Al + 3AgO → Al$_2$O$_3$ + 3Ag	0.76
Ag$_2$SO$_4$	8Al + 3Ag$_2$SO$_4$ → 4Al$_2$O$_3$ + 6Ag + 3S	0.56
AgNO$_3$	2Al + AgNO$_3$ → Al$_2$O$_3$ + Ag + 0.5N$_2$	0.48
AgClO$_4$	8Al + 3AgClO$_4$ → 4Al$_2$O$_3$ + 3Ag + 1.5Cl$_2$	0.39
AgIO$_3$	2Al + AgIO$_3$ → Al$_2$O$_3$ + Ag + 0.5I$_2$	0.32

Table 2: Experimental results for the three thermite systems used in this work. All oxidizers were mixed with nanoaluminum with an equivalence ratio of 1.

	Al/AgIO$_3$	Al/CuO	Al/Ag$_2$O
Pressure Rise (psi)	296	116	10.0
Pressure Rise Time (µs)	5.3	13	1459
Pressurization Rate (psi/µs)	57	9.0	0.002
FWHM Burn Time (µs)	172	192	1381

Table 3: A comparison of thermodynamic equilibrium predictions of Al/CuO and Al/Ag$_2$O thermites. Calculations are from Fischer and Grubelich[14] and assume constant HP with phase changes taken into account.

Reaction	ρ_{TMD} g/cm^3	T_{AD} K	moles gas per 100 g	Primary gas at equilibrium
2Al + 3CuO → Al$_2$O$_3$(L) + 3Cu(L,g)	5.109	2843	0.5400	Cu
2Al + 3Ag$_2$O → Al$_2$O$_3$(L) + 6Ag(L,g)	6.386	2436	0.4298	Ag
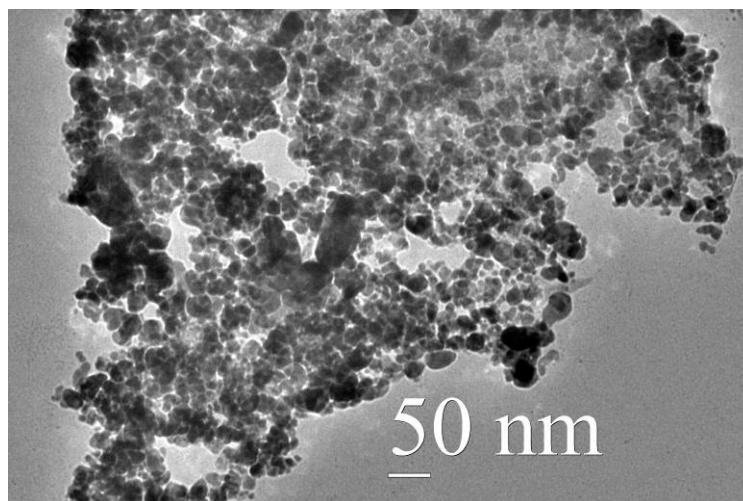
Figure 1: Transmission electron microscope image of the as-produced Ag$_2$O nanoparticles. The particles are primarily spherical and highly agglomerated. The primary particles are generally <20 nm in diameter.
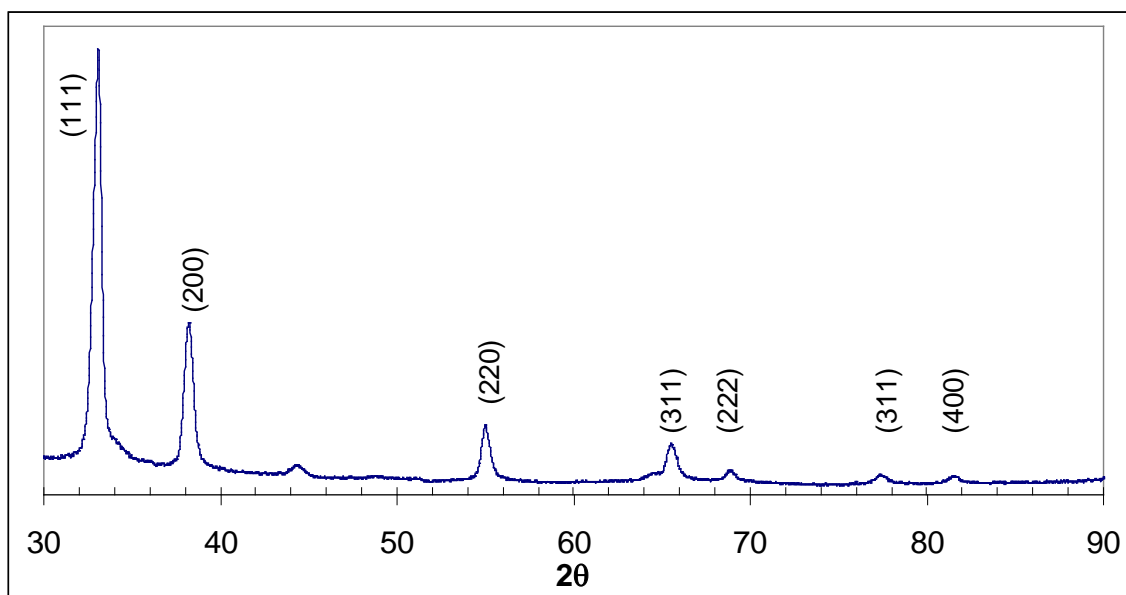
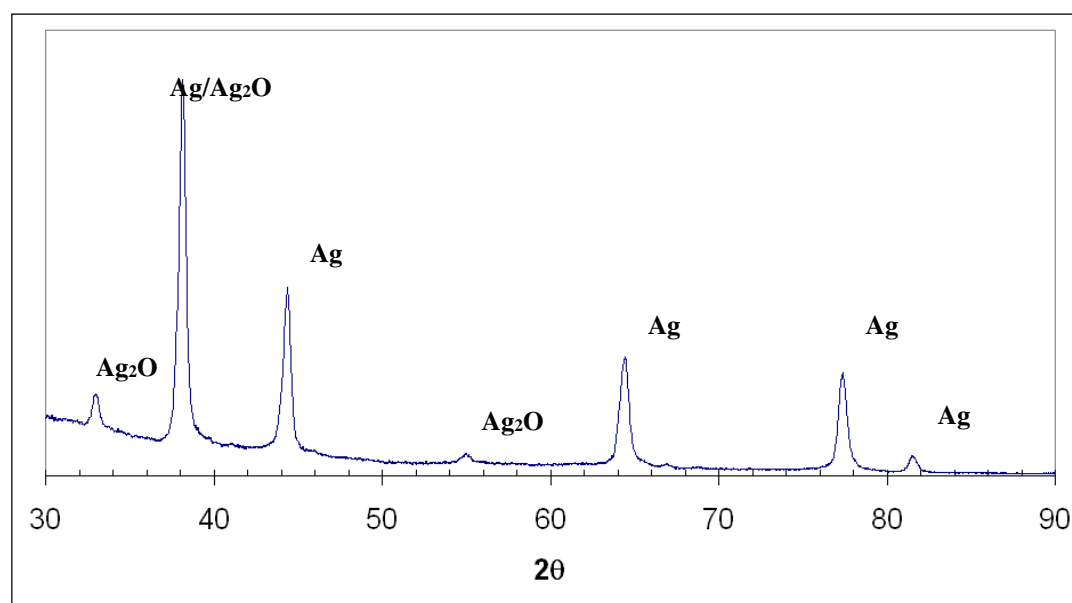**Figure 2: X-Ray Diffraction of the as-produced nanoparticles. The labeled peaks confirm the production of Ag$_2$O.**

Figure 3: X-Ray diffraction of reacted Al/Ag$_2$O. Note the presence of Ag$_2$O even after the reaction, indicating that some of the oxidizer was not fully decomposed.
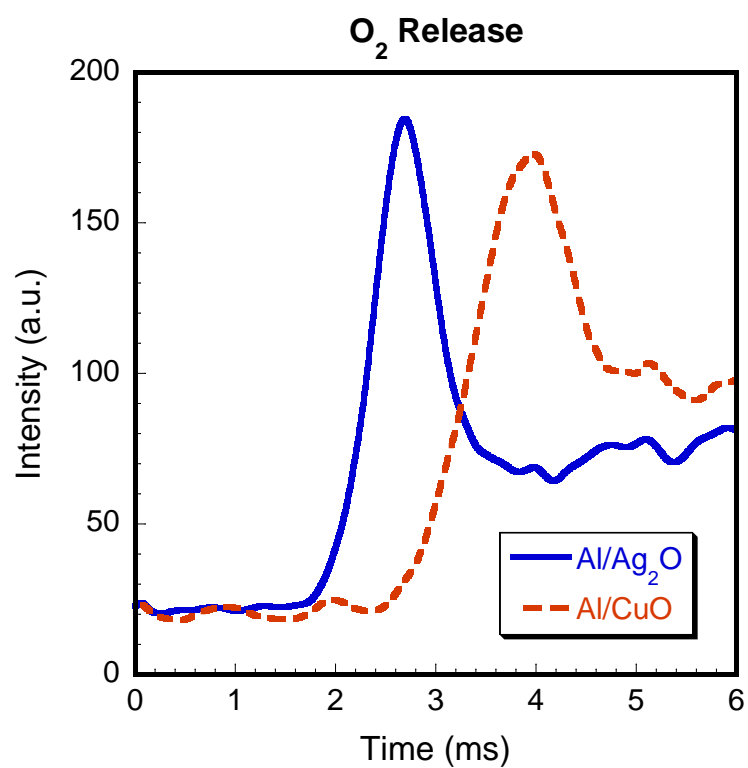
Figure 4: O$_2$ release profile of Al/Ag$_2$O and Al/CuO binary mixtures, as measured using a custom TOF-MS setup. The intensity of the O$_2$ peak is similar in both systems, but the onset occurs earlier in the Al/Ag$_2$O, a result consistent with thermodynamic considerations.
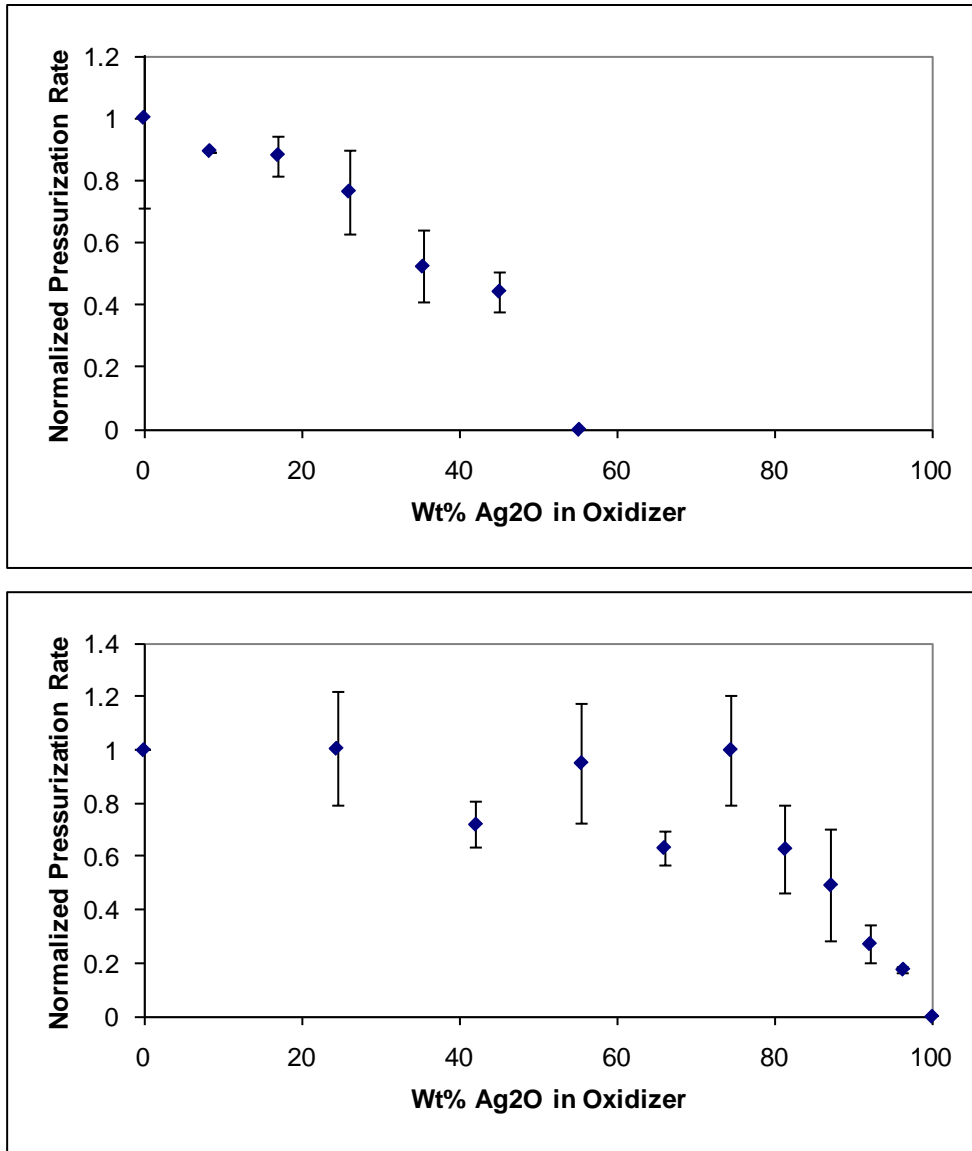
Figure 5: Experimental results for the Al/AgIO$_3$/Ag$_2$O (top) and Al/CuO/Ag$_2$O systems (bottom). Values have been normalized by pure Al/AgIO$_3$ and pure Al/CuO for the top and bottom, respectively. All mixtures are stoichiometric with an equivalence ratio of 1 assuming complete reaction to Al$_2$O$_3$.
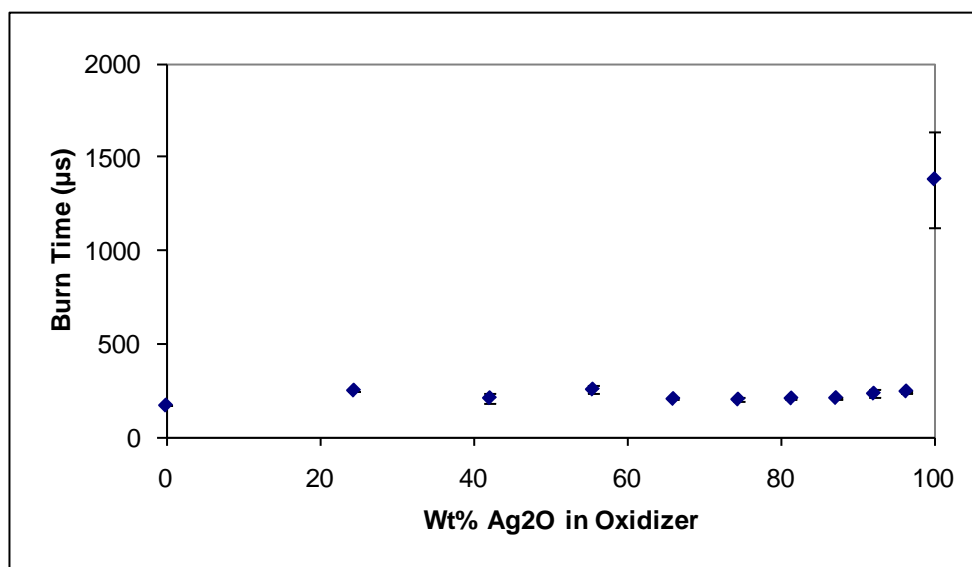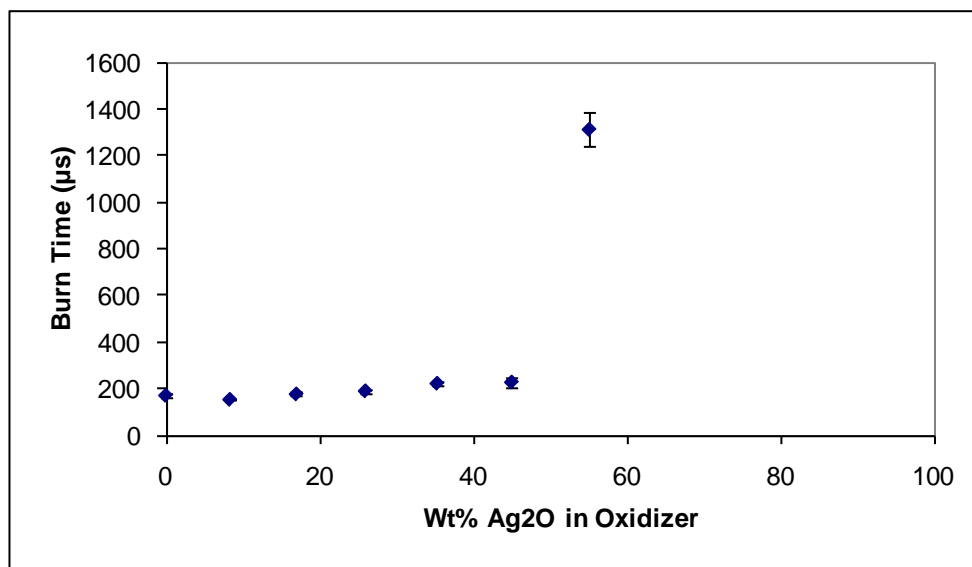
Figure 6: Burn time (full width half max of optical signal) as a function of Ag₂O mass loading for Al/AgIO₃/Ag₂O (top) and Al/CuO/Ag₂O (bottom).
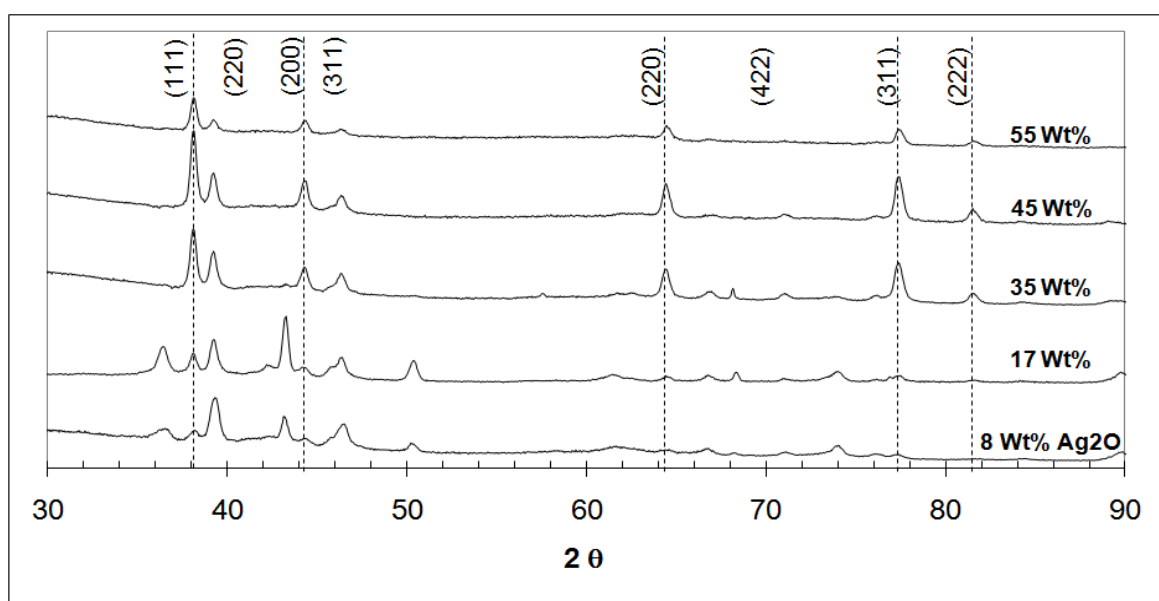
Figure 7: X Ray diffraction of the reacted Al/AgIO$_3$/Ag$_2$O samples collected after combustion in the pressure cell. The dotted vertical lines are Ag peaks, while the bold lines are AgI. XRD confirms the formation of elemental silver, along with decreasing amounts of AgI as the Ag$_2$O mass loading increases. Above 45 Wt%, a drop in the intensity of both Ag and AgI is observed, indicating a shift in the reaction mechanism, and experimentally supported by a sudden drop in the pressurization rate and increase in burn time.

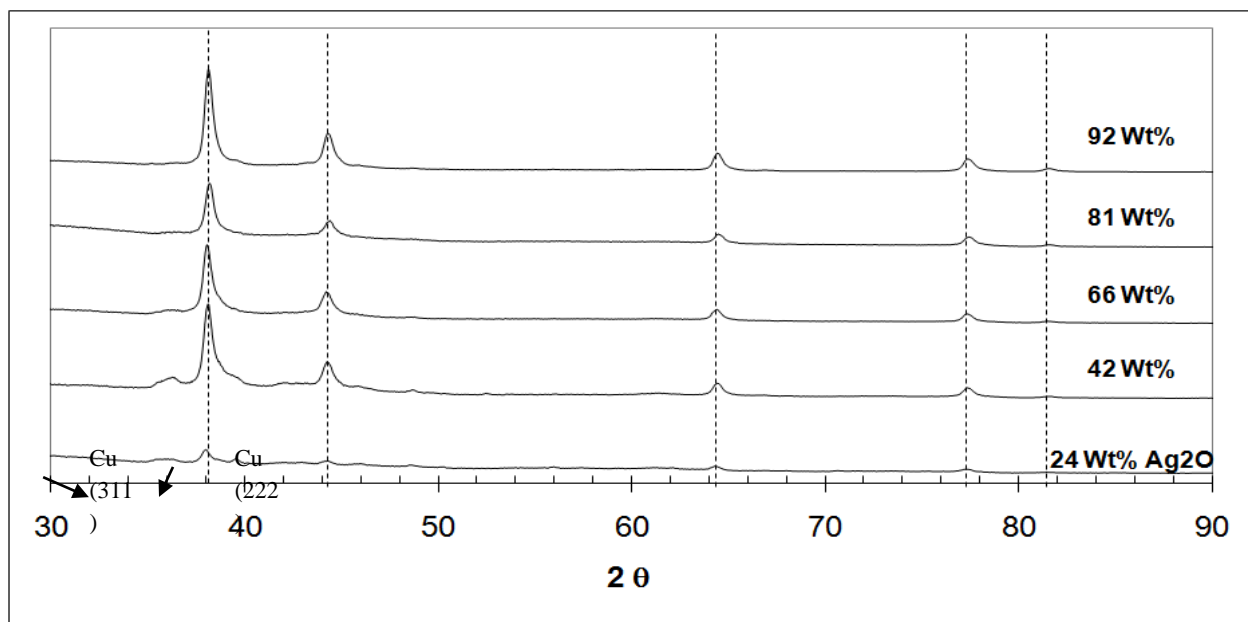**Figure 8: X-Ray diffraction of the reacted Al/CuO/Ag₂O samples collected after combustion in the pressure cell.**
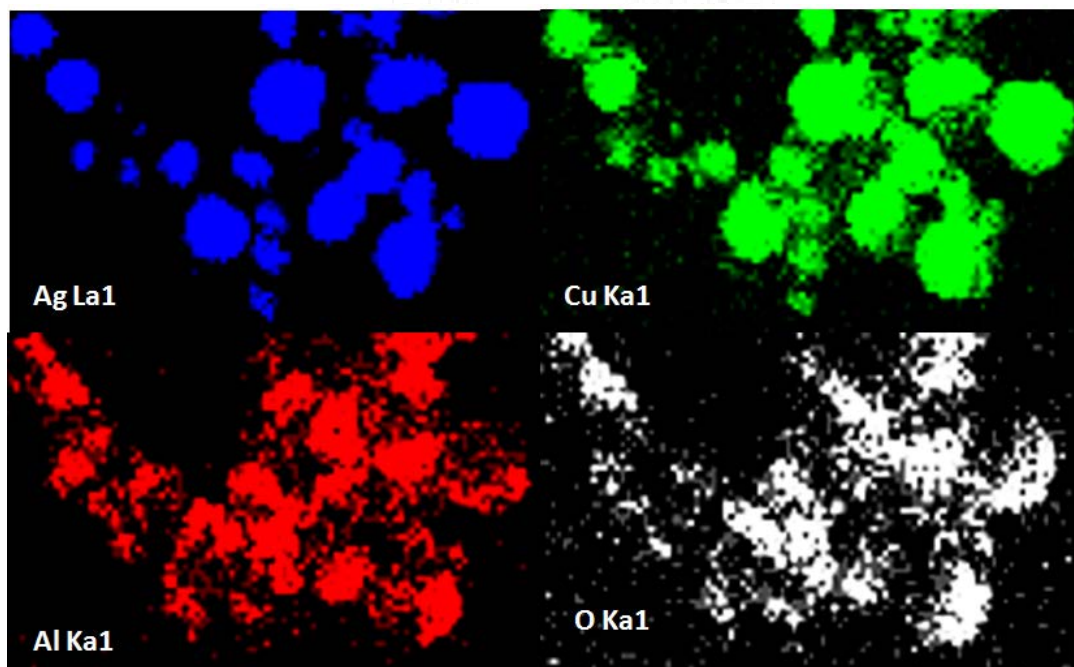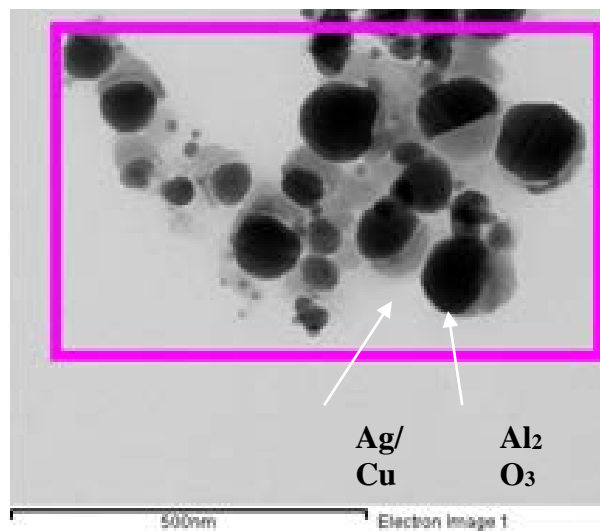
Figure 9: Image and elemental mapping of Al/74Wt% Ag₂O/26 Wt% CuO, corresponding to the maximum Ag₂O added before a significant decrease in the reactivity was seen. The results show Al$_x$O$_y$ is in surface contact with a product which is a combination of both Ag and Cu.
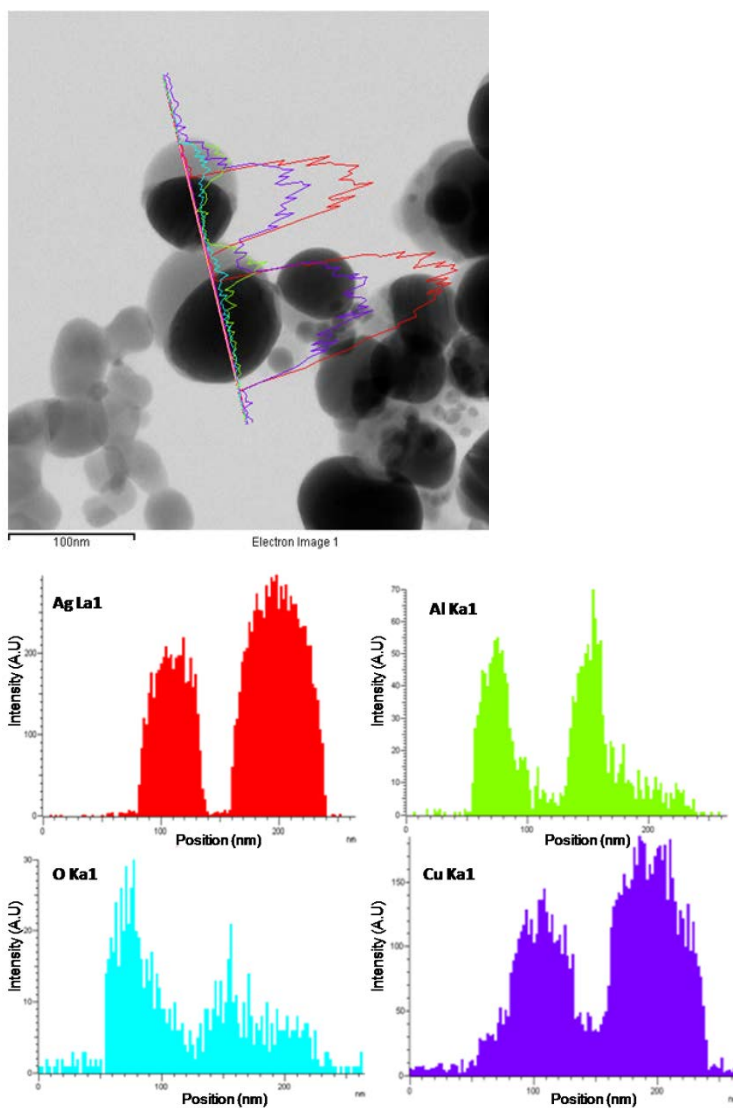
Figure 10: Image and elemental linescan across two particles showing the bright/dark morphology characteristic in the product. The sample was the same as in Figure 9. The linescan indicates that an Ag/Cu matrix is in surface contact with Al and O (assumed to be Al$_2$O$_3$).

References

1.   (a) Granier, J. J.; Pantoya, M. L., Laser ignition of nanocomposite thermites. *Combustion and Flame* **2004,** *138* (4), 373-383; (b) Sullivan, K. T.; Zachariah, M. R., Simultaneous Pressure and Optical Measurements of Nanoaluminum-Based Thermites: An Investigation of the Reaction Mechanism. *In press- Journal of Propulsion and Power* **2010**.

2.   (a) Perry, W. L.; Smith, B. L.; Bulian, C. J.; Busse, J. R.; Macomber, C. S.; Dye, R. C.; Son, S. F., Nano-scale tungsten oxides for metastable intermolecular composites. *Propellants, Explosives, Pyrotechnics* **2004,** *29* (2), 99-105; (b) Prakash, A.; McCormick, A. V.; Zachariah, M. R., Synthesis and reactivity of a super-reactive metastable intermolecular composite formulation of Al/KMnO4. *Advanced Materials (Weinheim, Germany)* **2005,** *17* (7), 900-903; (c) Son, S. F.; Busse, J. R.; Asay, B. W.; Peterson, P. D.; Mang, J. T.; Bockmon, B.; Pantoya, M. L., Propagation studies of metastable intermolecular composites (MIC). *Proceedings of the International Pyrotechnics Seminar* **2002,** *29th*, 203-212.

3.   (a) Aumann, C. E.; Skofronick, G. L.; Martin, J. A., Oxidation behavior of aluminum nanopowders. *Journal of Vacuum Science & Technology, B: Microelectronics and Nanometer Structures* **1995,** *13* (3), 1178-83; (b) Pantoya, M. L.; Granier, J. J., Combustion behavior of highly energetic thermites: nano versus micron composites. *Propellants, Explosives, Pyrotechnics* **2005,** *30* (1), 53-62.

4.   Sambhy, V.; MacBride, M. M.; Peterson, B. R.; Sen, A., Silver Bromide Nanoparticle/Polymer Composites: Dual Action Tunable Antimicrobial Materials. *Journal of the American Chemical Society* **2006,** *128*, 9798-9808.

5.   Sullivan, K. T.; Piekiel, N. W.; Chowdhury, S.; Wu, C.; Zachariah, M. R.; Johnson, C. E., Ignition and Combustion Characteristics of Nanoscale Al/AgIO$_3$: A Potential Energetic Biocidal System. *Combust. Sci. and Tech.* **2011,** (183), 285-302.

6.   Zhou, L.; Piekiel, N.; Chowdhury, S.; Zachariah, M. R., T-Jump/time-of-flight mass spectrometry for time-resolved analysis of energetic materials. *Rapid Communications in Mass Spectrometry* **2009,** *23* (1), 194-202.

7.   Merck, *The Merck Index*. 13 ed.; Merck & Co., Inc.: Whitehouse Station, NJ, 2001.

8.   Rentz, E. J., Viral pathogens and severe acute respiratory syndrome: Oligodynamic Ag+ for direct immune intervention. *Journal of Nutritional & Environmental Medicine (Abingdon)* **2003,** *13* (2), 109-118.

9.   Morones, J. R.; Elechiguerra, J. L.; Camacho, A.; Holt, K.; Kouri, J. B.; Ramirez, J. T.; Yacaman, M. J., The Bactericidal Effect of Silver Nanoparticles. *Nanotechnology* **2005,** *16* (10), 2346-2353.

10.   Smetana, A. B.; Klabunde, K. J.; Marchin, G. R.; Sorensen, C. M., Biocidal activity

of nanocrystalline silver powders and particles. *Langmuir* **2008,** *24* (14), 7457-7464.

11.   Henz, B. J.; Hawa, T.; Zachariah, M. R., On the role of built-in electric fields on the ignition of oxide coated nanoaluminum: Ion mobility versus Fickian diffusion. *Journal of Applied Physics 107* (2).

12.   Sendroy, J., Microdetermination of Chloride in Biological Fluids, with Solid Silver Iodate. *J. Biol. Chem* **1937,** *120*, 335-403.

13.   Sullivan, K. T.; Johnson, C. E.; Piekiel, N. W.; Chowdhury, S.; Wu, C.; Zachariah, M. R., Ignition and Combustion Characteristics of Nanoscale Al/AgIO3: A Potential Energetic Biocidal System. *Submitted to Combustion Science and Technology* **2010**.

14.   Fischer, S. H.; Grubelich, M. C., Theoretical Energy Release of Thermites, Intermetallics, and Combustible Metals. *24th International Pyrotechnics Seminar* **1998**.

15.   Jeurgens, L. P. H.; Sloof, W. G.; Tichelaar, F. D.; Mittemeijer, E. J., Thermodynamic stability of amorphous oxide films on metals: Application to aluminum oxide films on aluminum substrates. *Physical Review B: Condensed Matter and Materials Physics* **2000,** *62* (7), 4707-4719.

16.   Trunov, M. A.; Schoenitz, M.; Dreizin, E. L., Effect of polymorphic phase transformations in alumina layer on ignition of aluminium particles. *Combustion Theory and Modelling* **2006,** *10* (4), 603-623.

17.   Rai, A.; Park, K.; Zhou, L.; Zachariah, M. R., Understanding the mechanism of aluminum nanoparticle oxidation. *Combustion Theory and Modelling* **2006,** *10* (5), 843-859.

18.   Sullivan, K. T.; Chiou, W. A.; Fiore, R.; Zachariah, M. R., In situ microscopy of rapidly heated nano-Al and nano-Al/WO3 thermites. *Applied Physics Letters 97* (13).

19.   Tachibana, Y.; Kusunoki, K.; Watanabe, T.; Hashimoto, K.; Ohsaki, H., Optical properties of multilayers composed of silver and dielectric materials. *Thin Solid Films* **2003,** *442* (1-2), 212-216.

20.   Moulder, J. F.; Stickle, W. F.; Sobol, P. E.; Bomben, K. D., *Handbook of X-ray Photoelectron Spectroscopy*. 5th ed.; Perkin-Elmer Co.: Eden Prairie, 1992.

21.   Rodriguez, J. A.; Kuhn, M.; Hrbek, J., Interaction of silver, cesium, and zinc with alumina surfaces: Thermal desorption and photoemission studies. *Journal of Physical Chemistry* **1996,** *100* (46), 18240-18248.

Appendix: Supporting Information

The following section includes analysis of the materials using X-Ray photoelectron spectroscopy. This material is available free of charge via the Internet at http://pubs.acs.org.

XPS Measurements and Analysis

XPS data for silver Ag 3d and Ag MNN were collected for both ternary systems. Data was collected for various Wt% of Ag_2O in each system, however, only one set of results will be presented from each system. The data selected is for mixtures with a large Wt% of added Ag_2O, but before a significant drop in reactivity was measured. This corresponded to 35 Wt% Ag_2O for the $Al/Ag_2O/AgIO_3$ system, and 87 Wt% for the $Al/Ag_2O/CuO$ thermite. A comparison of the spectra before (a,b) and after (c,d) combustion for 35 Wt% Ag_2O in $Al/Ag_2O/AgIO_3$ and 87 Wt% Ag_2O in $Al/Ag_2O/CuO$ are shown in Figures 11 and 12, respectively. Due to very small shifts in binding energy in the Ag 3d region, less than 0.4 eV between Ag, Ag_2O and AgO, it is not possible to discern oxidation state changes based on BE shifts alone. However, the Auger transition exhibits considerable shifts, this two electron hole final state being more sensitive to surrounding environment. Even more convenient is to compare Auger parameters which have the added benefit of being independent of sample charging and work function. The modified Auger parameter, α' can be obtained through XPS measurements and is defined as:

$$\alpha' = KE(Auger) - KE(photoelectron) + h\nu$$

where KE(Auger) is the kinetic energy of an auger transition, KE(photoelectron) is the kinetic energy of a core level photoelectron, and $h\nu$ is the photoexitation energy.

While the BE shift alones are subtle, the Ag 3d and Auger spectra after combustion are significantly different from that of the starting material for both samples. The Ag 3d

peaks show a significant narrowing of the FWHM, the appearance of a second peak and low intensity plasmon loss peaks associated with the Ag 3d5/2 and 3/2 spin-orbit-split components. The presence of the plasmon peaks which are separated from the most intense Ag 3d 5/2 an 3/2 by ~3.5 eV to higher binding energy[19] (labeled with an arrows in the figure) and the narrowed FWHM are characteristic of metal formation. The appearance of the additional peak at 368.9 eV could be due to the formation of some silver aluminum alloy, as it is in good agreement with literature values, 368.8- 369.0 eV.[20] Another possibility is small metallic clusters of silver dispersed on the alumina have also been reported to lead to increases in the Ag 3d binding energy compared to bulk Ag.[21] The Auger parameter of 726.3 eV calculated using the most intense Ag 3d5/2 peak and the Ag $M_4N_{45}N_{45}$ transition is also consistent with the formation of metallic silver.

In Figure 11, the Ag spectra from the combusted sample differ significantly from both the $AgIO_3$ and Ag_2O starting materials. The Ag 3d 5/2 for the reacted sample has a FWHM of 0.79 eV and Plasmon loss peaks again both these features are consistent with metal formation. For the MNN Auger peaks shown in Figure 11 (d) both $M_4N_{45}N_{45}$ transition (~356 eV) and $M_5N_{45}N_{45}$ transition (~349 eV) seem to be split into two, Auger parameters were calculated using both peaks for the $M_4N_{45}N_{45}$ transition, labeled a and b in Figure 11 and energies reported in Table 4. The binding energy position for the 5/2 peak of 368.8 eV is surprisingly high for pure metallic silver or silver iodide as expected and seen in the x-ray diffraction. Based on the Auger parameter values and XRD results we believe this binding energy to be erroneously high due to differential charging between the hydrocarbon used as the calibration point and the silver. We assign the Auger parameter calculated using peak b ($\alpha' = 726.2$ eV) to be due to metallic silver and peak a ($\alpha' = 724.5$ eV)

to be due to silver iodide, their values compared to literature values in Table 4.

Table 4: Modified Auger parameters (α').

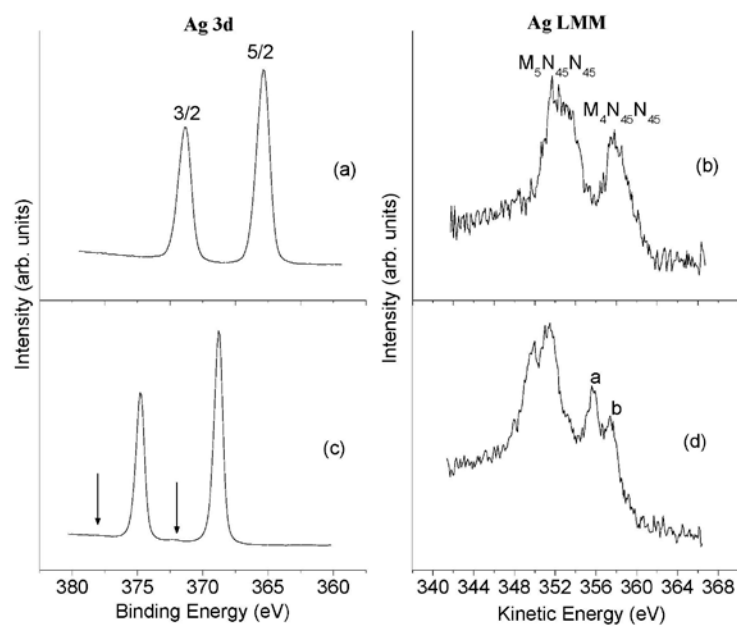|	Ag 3d Binding Energy (eV)	Ag M$_4$N$_5$N$_5$ Kinetic Energy (eV)	α' (eV)
Ag	368.1-368.3[*]	357.9-358.3	726.0-726.6
AgI	368.0[*]	356.1[*]	724.1[*]
Ag$_2$O	368.1[*] 368.0[#]	356.6[*], 356.6[#]	724.4[*], 724.3[#]
AgIO$_3$	367.9[#]	355.8	723.7
40% Ag$_2$O (AgIO$_3$)	368.8[#]	357.4[#a], 355.7[#b]	726.2[#a], 724.5[#b]
70% Ag$_2$O (CuO)	368.1[#], 368.9[#]	358.2[#]	726.3[#], 727.1[#]

*Taken From Ref 22

This work

a For AgI

b For Ag

39

Figure 11: Ag 3d core level and Ag MNN Auger spectra for the AgIO₃ starting material (a,b) as compared to the spectra from the product of combustion (c,d) for an Al/Ag₂O/AgIO₃ mixture with 35 Wt% Ag₂O.
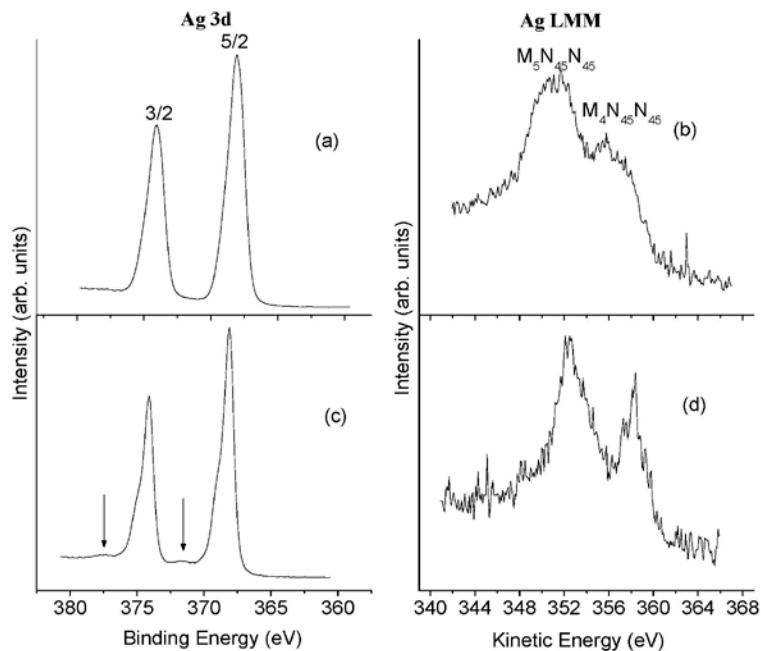
Figure 12: Ag 3d core level and Ag MNN Auger spectra for the Ag$_2$O starting material (a,b) as compared to the product of combustion (c,d) for an Al/Ag$_2$O/CuO mixture with 87 Wt% CuO.

III. Results for FY-12

This year we have focused on two major thrusts:

1. **Development of a method to create passivated I2O5 and its reactive characterization.**
2. **Preliminary results on the dispersion characteristics of thermite samples as a function of time.**

1. **Development of a method to create passivated I2O5 and its reactive characterization.**

Abstract

Iodine pentoxide is a strong oxidizer which has been recently proposed as a candidate oxidizer in nanoenergetic formulations for biocidal applications. However, its highly hygroscopic nature hinders its performance as a strong oxidizer, and prevents its implementation. In this work, we focus on developing a synthetic approach to creat nanoscale partiles of I2O5 which are passivated with a metal oxide shell. Iron oxide passivated iodine pentoxide nanocomposites were successfully fabricated via a gas phase assisted aerosol spray-pyrolysis with the introduction of gas phase precursor to iron oxide. The final product shows a violent reaction when employed as an oxidizer with aluminum fuel demonstrating a higher pressurization rate and transient peak pressure with respect to that of nano-Fe_2O_3. The synthetic strategy proposed here is simple and could be extendable to passivate other hygroscopic materials.

Introduction

Nanoenergetic material, also called nanothermite, in which metal fuel and metal oxide oxidizer have particle dimensions on the nanometer scale, have been shown to have superior exothermic characteristics and possess properties unobtainable by traditional energetic materials. The nanoscale structures enable the intimate mixing between the fuel and oxidizer, which reduce the heat and mass transport limitations, leading to a significant enhancement in its reactivity and burn rate [1].

Iodine pentoxide is a strong oxidizer for thermite reaction and recently has been proposed as an attractive candidate foragent defeat applications [2]. It has been shown that the "Al + I_2O_5" reaction is effective at neutralizing spores, presumably due to release of elemental iodine as a combustion product when reacted with aluminum [3]. Unfortunately I_2O_5 is sensitive to humid environments

and reacts with water to form iodic acid after exposure to air. This severely limit its utility as a possible strong oxidizer in combustion, but also inhibits its application as a biocide in agent defeat. To solve such a problem, it is appealed to create a passivated structure for I_2O_5 to protect it from humidityin air.

Several methods are currently available to fabricate passivated nanoparticles and can be generally categorized into "wet treatment" [4] and "gas phase" approaches[5]. The "liquid phase" approaches, such as the coprecipitation, sol-gel, and mircoemulsion etc., disperse core particles in solvent containing reactive precursors, is not applicable to passivate I_2O_5 since they requires dealing with liquid phase (solvent, binders or water), and I_2O_5 is imcompatible to water and organic solvents [6]. The alternative "gas phase" approaches, which has the possibility of scale up, [5], is explored as more suitable approach to make passivated I_2O_5 material.

Prakash *et al.* in our group reported a single step, two-temperature aerosol spray-pyrolysis process to create a pure core-shell nanostructure for nanothermite formulations, where a thin layer of relatively mild oxidizer (Fe_2O_3) was coated on a strong oxidizer ($KMnO_4$) nanoparticle. In this process, precursor $Fe(NO_3)_3 \cdot 9H_2O$ and $KMnO_4$ are dissolved in an aqueous solution and sprayed into droplets which are typically one micron in diameter [7]. The droplets passthrough the diffusion dryer, and to two tube furnaces maintained at different temperatures. The first furnace was maintained above the iron nitrate decomposition temperature (~120 °C) while the second furnace was operated at near the melting point of potassium permanganate (~ 240 °C). With this strategy at 120 °C, the iron nitrate decomposes into Fe_2O_3 , in the permanganate solid matrix. Then the temperature is raised to 240 °C, where the permanganate melts, and the Fe_2O_3 begins to phase separate, and aggregate as a shell around the $KMnO_4$core. The reactivity of the resulting materials could be tuned by varying the coating thickness of the weaker oxidizer Fe_2O_3 [7]. To further extend

43

the application of this approach, Wu *et al.* in our group employed this strategy and successfully incorporated high oxygen content perchlorate salts ($KClO_4$ and NH_4ClO_4) into the common metal oxide (Fe_2O_3 and CuO) shell [8]. Here the key to this strategy is to take advantage of both the aerosol spray-pyrolysis (all the physical and chemical processes occur in the confined aerosol droplet as a micro-reactor) [9] and the difference in the characteristic temperatures of the two precursors; to create through phase separation processes a desired core-shell nanostructure.

Although the above-mentioned single step, two-temperature aerosol spray-pyrolysis strategy is simple, it failed to passivate I_2O_5 particle. The shell precursors iron nitrate ($Fe(NO_3)_3$) and copper nitrate ($Cu(NO_3)_2$) reacted immediately with iodic acid, to form metal iodate precipitates in starting solution [10] and thus, an alternative approach was required. In this work, we developed a modified gas phase assisted aerosol synthesis approach to successfully passivate I_2O_5 within an iron oxide shell to create an air-stable passivated oxidizer. The as prepared Fe_2O_3/I_2O_5 passivated oxidizer was characterized by transmission electron microscopy (TEM) and =Energy Dispersive X-Ray Spectroscopy (EDS) for composition and morphology. Time resolved high heating rate mass spectrometry was used to characterize reactivity. . These nanocomposite materials were then formulated into nanoaluminum based thermite mixture to evaluate its reactive properties as an oxidizer. The final product shows a violent reaction and exhibits an excellent gas generating behavior when formulated with nanoaluminum, demonstrating a very higher pressurization rate and transient peak pressure.

Experimental Section

Materials

Iodic acid (HIO_3, 99.5%), iodine pentoxide powder (I_2O_5, 99.99 %), iron pentacarbonyl ($Fe(CO)_5$, > 99.99%), reference Fe_2O_3 nanopowder (< 50 nm) and CuO nanopowder (< 50 nm) were all purchased from Sigma-Aldrich. The nano-sized aluminum (~ 50 nm ALEX) used in the combustion cell test was obtained from the Argonide Corporation. The aluminum nanopowders were found to contain 70 wt% active Al as measured by thermogravimetric analysis (TGA).

Aerosol Spray-Pyrolysis and Materials Characterization

Aerosol spray-pyrolysis includes two steps: atomization and thermal decomposition (Figure 1). In the atomization step the aerosol droplets containing the dissolved precursor solution were generated by a home-made pressure atomizer. The droplet diameter, as measured by a laser aerosol spectrometer, is typically around 1 µm [11]. Droplets passed through a silica-gel diffusion dryer to remove most of the precursor solvent, and then through tubefurnaces for the thermal decomposition. The residence time wastypically around 1 second for a total gas flow rate of 3.5 L/min. The final products were collected on a 0.4 µm pore Millipore HTTP membrane filter. TEM (JEOL JEM 2100 FEG) and EDS (Oxford INCA 250) line scans, provided informationon particle morphology and elemental core-shell structure.

Iron Oxide passivation coating   Iron oxide was chosen as a passivating coating because of the prior success in passivating potassium permanganate [ref]. In this case, however the iron oxide coatig was generated by thermal decomposition of iron pentacarbonyl, with the objective of vapor depositing material to the surface of the I2O5. Iron pentacarbonyl vapor was generated by bubbling a metered flow of argon through the liquid in an ice bath. The vapor was then mixed with the aerosol stream and decomposed at ~ 200 C.

Thermite Sample Preparation

In order to create a stoichiometry thermite mixture with aluminum, a knowledge ratio of iron to iodine in the oxidizer, is needed. This was determined by a measurement of the oxidizer's weight loss during the thermal decomposition of I_2O_5 at a temperature of 600 °C [12] using a Sartorius SE2 Ultra Micro Balance. The appropriate amounts of nano-aluminum fuel and oxidizer were weighed out and mixed in hexane and then sonicated for 30 min to ensure an intimate mixture. The hexane was allowed to evaporate in the fume hood overnight (or in a vacuum dryer at room temperature for 3 or 4 hours). The dry powder was gently broken apart to obtain a loose powder, prior to testing.

Constant-volume Combustion Cell Experiment

To evaluate performance simultaneous pressure and optical measurements were conducted in a constant-volume combustion cell [7] [13] to characterize the reactivity of the prepared thermite samples. Since the measurement of the thermites' reactivity is a relative experiment, both the pressurization rate and optical emission measurements are reported as relative values with respect to reference oxidizers of Fe_2O_3 and CuO nanoparticles. In a typical pressure cell experiment, a thermite sample powder with a fixed mass (25 mg), was loadedin a constant-volume (~13 cm^3) pressure cell, and ignited by resistive heating with a nichrome wire.. A fast time response piezoelectric pressure transducer attached to the cell was sued to measure the transient pressure pulse. The optical emission was simultaneously collected by a lens tube containing a planoconvex lens (f = 50 mm). The characteristic burn time of thermites in the combustion cell was represented

by the full width at half-maximum (FWHM) of the recorded optical signal. The details of the combustion cell test can be found in our prior publications [7] [13].

Temperature-Jump/Time-Of-Flight Mass Spectrometry (T-Jump/TOFMS)

Rapid hating experiments coupled to mass-spectrometry employ 12 mm long, ~ 76 μm diameter Pt wire which was coated with a thin layer of sample powder (< 0.03 mg). The wire can berapidly heated up to ca. 1800 K in 3 ms at a heating rate of ~ 5×10^5 K/s and was replaced after each heating event. The temporal measured wire resistance are used to determine the temporal filament temperature. The wire was heated within the ion extraxtion region of a time-of-flight mass spectrometer. The details of T-Jump/TOFMS experiment can be found in our previous papers [14] [15].

High-speed imaging

High speed imaging of the wire tests were conducted under atmospheric conditions using a Vision Research Phantom® v12.0 hi-speed digital camera at a resolution of 256×256 with a frame rate of 67065 fps (14.9 µs per frame) [8].

Results and Discussions

1. Synthesis of Passivated I2O5

The basic idea of this aerosol coating approach was to first synthesize aerosol particles of I_2O_5 , which would then be *in situ* passivated with a layer of iron oxide using controlled thermal decomposition of iron pentacarbonyl in air. The objective was to use the I_2O_5 nanoparticles as

the substrate for the iron oxide to deposit onto, and thus to form a core-shell passivated structure.
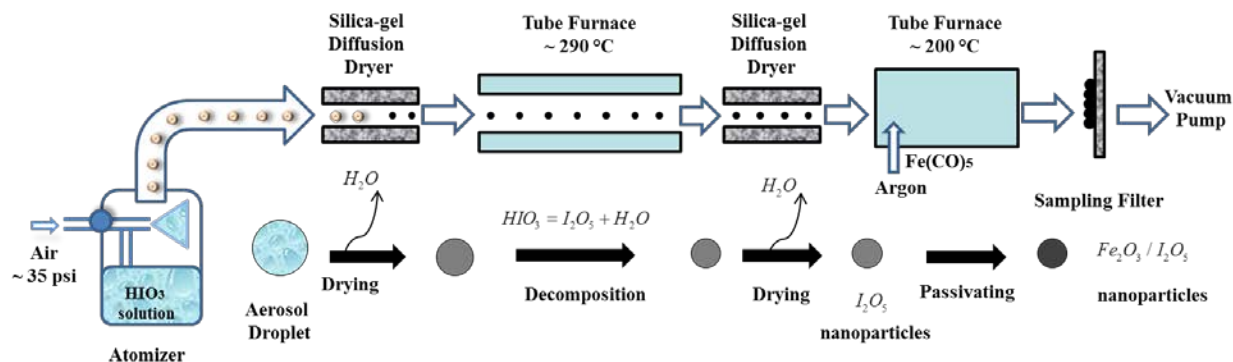
Figure 1. *Experimental system for synthesis and passivation of I₂O₅ with iron oxide.*

The experimental setup is schematically depicted in Figure 1. As shown in Figure 1, I₂O₅ particles were produced using an aerosol spray-pyrolysis with air as the carrier gas in the first furnace heated to ~ 290 °C, which is above the reported decomposition temperature for

$HIO_3 = I_2O_5 + H_2O$, ~ 207 °C [12], but below the reported decomposition temperature of I₂O₅, ~ 391°C [12]. Thus starting with aqueous solutions of iodic acid (HIO₃) the sprayed aerosol droplets from the atomizer were delivered through a silica-gel diffusion dryer to remove most of the water. The first furnace at 290 ℃ should fully decompose iodic acid to iodine pentoxide and water. A second silica-gel diffusion dryer was introduced to remove the water produced during the iodic acid decomposition, to ensure that particles entering the second furnace were I₂O₅ and did not revert back to iodic acid

To create the coated I₂O₅ particles the iron pentacarbonyl precursor vapor was input downstream of the I₂O₅ particles at ~ 200 °C where the iron pentacarbonyl decomposed to iron and carbon monoxide [16]. The delivery rate of the iron pentacarbonyl into the second furnace is controlled by the flow rate of the argon. The *in situ* passivating process is detailed in Figure 2.
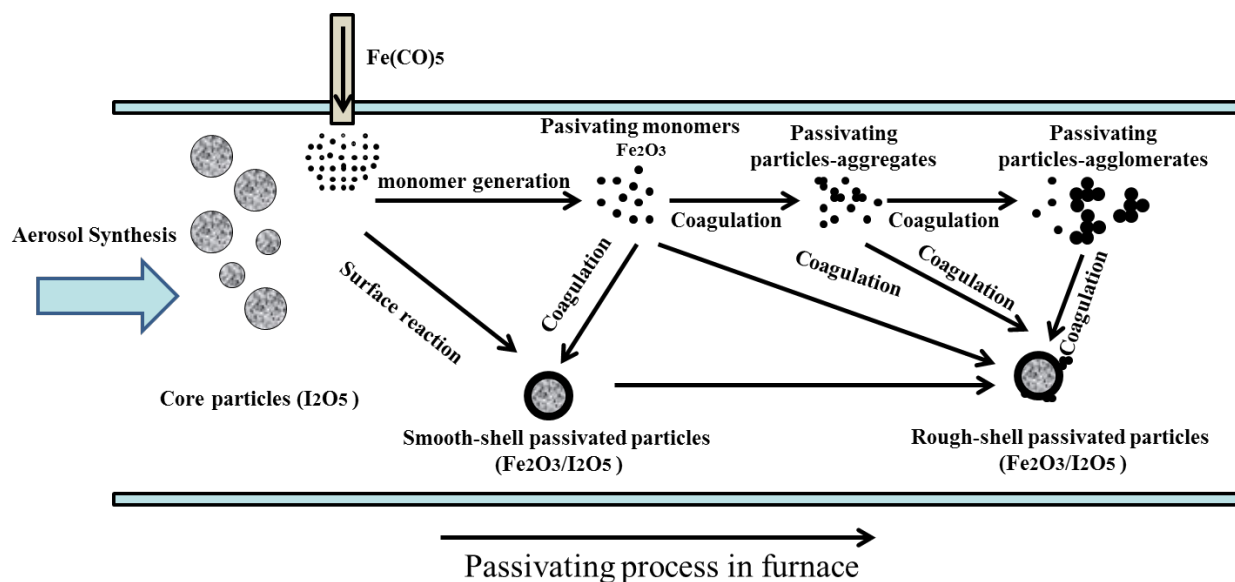
Figure 2. *Schematic illustration of in situ passivating process of I_2O_5 with Fe_2O_3.*

As shown in Figure 2, the core particles (I_2O_5) enter the second furnace with air as the carrier gas and mixed with the $Fe(CO)_5$ vapor. The passivating monomers, Fe_xO_y, are generated by decomposition of iron pentacarbonyl vapor. Several competing steps can occur during the passivating process. One possibility is that the monomers will either deposit onto the I_2O_5 to create smooth-shell passivated particles or coagulate among themselves to grow into larger passivating particles. Also the $Fe(CO)_5$ vapor may decompose onto the core particles by surface reaction leading to smooth-shell passivated particles. Additionally the passivating aggregates and agglomerates could also deposit onto the core particles and form rough-shell passivated particles [17] [18]. However, we expect that at low argon flow rates (i.e. small delivery rate of iron pentacarbonyl) the heterogeneous reaction is favored, leading to a smooth shell-core Fe_2O_3/I_2O_5 passivated particles. With increasing argon flow rate, more Fe_xO_y are produced, and gas phase homogeneous nucleation will lead to new particle formation. These particles will ocatgulate with I2O5 surface and lead to rough-shell passivated particles.

Characterization of the Passivated I2O5

1.1 Structure, Morphology, and Composition.

The synthesized particles, structure, morphology and composition were characterized by several techniques including TEM, elemental analysis as well as time resolved mass spectrometry.
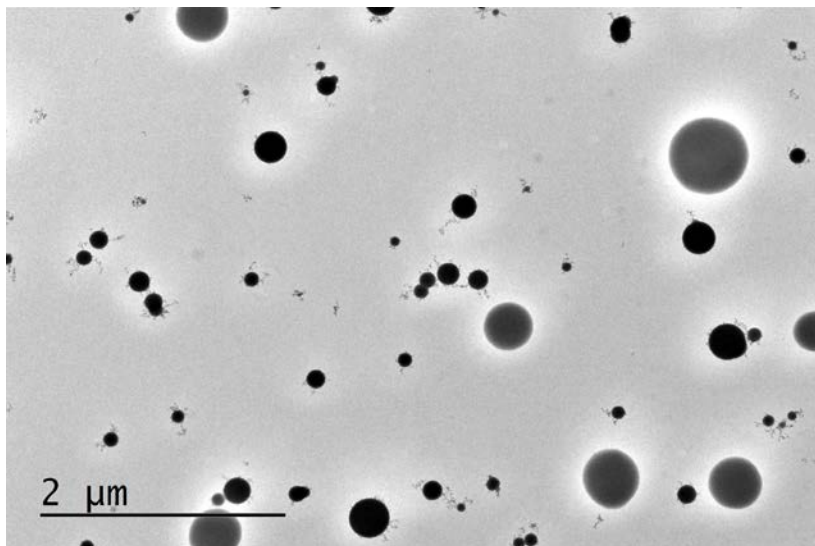
Figure 3. *A representative TEM image of I_2O_5/Fe_2O_3 passivated oxidizer with a Fe/I molar ratio of 1.8.*

Figure 3 shows a representative TEM image of final product with a Fe/I molar ratio of 1.8. The particles are highly spherical (Size distribution , mean size ???) and in this case clear fractal like aggregrates are extending from the surface, implying that considerable gas phase homogeneous nucleation of the iron oxide was taking place.
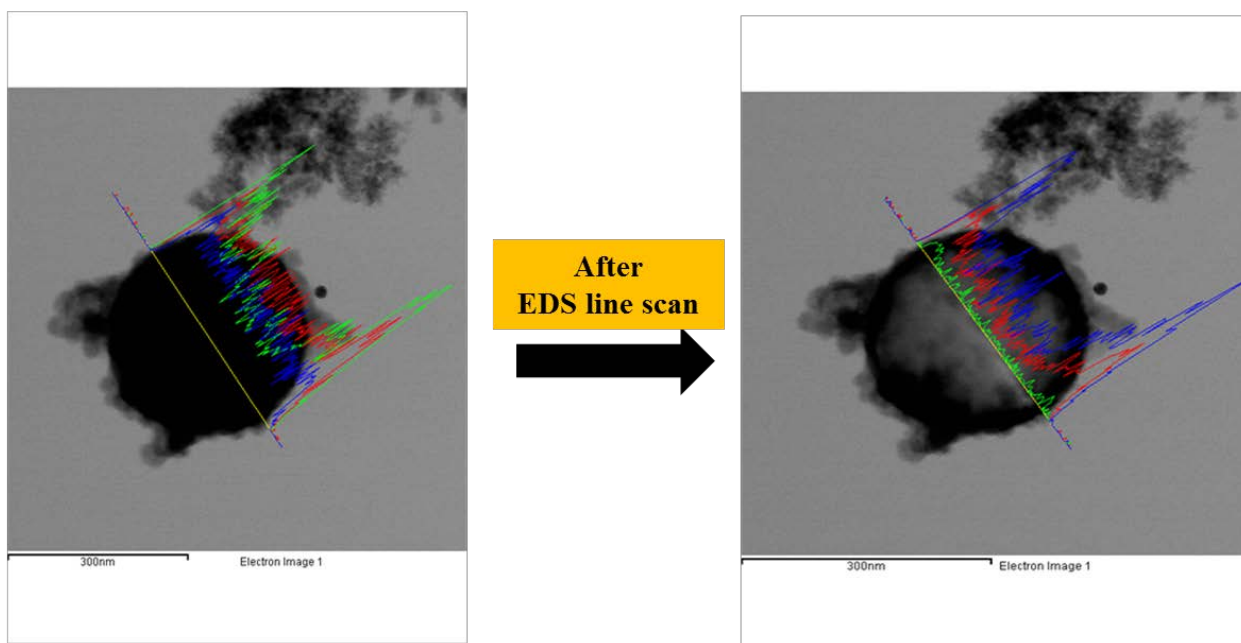
Figure 4. *A typical TEM image of I₂O₅/Fe₂O₃ passivated oxidizer product with elemental line scan:*

*(a) EDS line scan profile of a solid particle. Green: iron; red: oxygen; blue: iodine.*

(b) EDS line scan elemental profile of a hollow particle obtained from (a) after an EDS line scan. Green: iodine; red: oxygen; blue: iron.

Figure 4 shows the TEM image of passivated oxidize product with an elemental line scan. It is obvious from Figure 4 (a), that we have obtained a core/shell type particle, which an iodine oxide core, and an iron oxide shell. It was also apparent that after rastering the electron beam through the aprticle to get the EDS measurement that the particle was changed. This is shown in Figure 4(b) which illustrated that the particle has become hollow. In this case the electron beam effectively heats the particle enough to decompose I2O5 and volatilize the iodine, leaving behind the iron oxide shell..
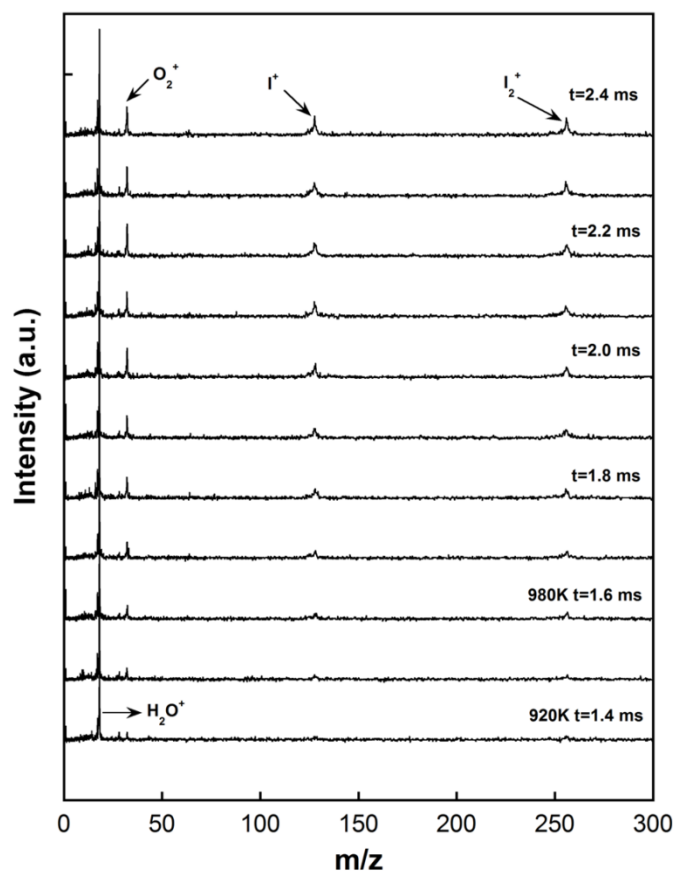
Figure 5. *Time resolved mass spectra of the Fe$_2$O$_3$/I$_2$O$_5$ passivated oxidizer with a Fe/I ratio of 4.3 under rapid heating. Note: heating pulse is ~3 ms, i.e. heating rate of ~5 × 10^5 K·s^{-1}.*

T-Jump/TOFMS wass employed to characterize the species formed during rapid heating, as might be encountered in a true combustion event. In this case the passivated oxidizers are rapidly heated to ~1800 K in 3 ms, and time resolved mass spectra of the products are obtained. Figure 5 shows the time resolved mass spectra of the Fe$_2$O$_3$/I$_2$O$_5$ nanocomposite oxidizer under a heating rate ~5 × 10^5 K·s^{-1}. We observe, O$_2$, I, I$_2$ as the primary species produced commencing at ~920 K (t=1.4 ms), . The H$_2$O observed we can attribute to background species in the mass spectrometer. The import point is that production of I$^+$, I$_2^+$ species without other iodine sub-oxides species suggests that the as prepared iron oxide

passivated I_2O_5 , which were exposed to ambient air, successfully encapsulated the I2O5

from forming iodic acid [19].

1.2 Combustion Characterization of "nano-Al + (Fe₂O₃/I₂O₅)" thermite system.

High-speed digital photography to observe the reactive behavior was carried out at high

heating rate ($\approx 5 \times 10^5$ K·s^{-1}) on a 76 μm diameter platinum wire, for which selected

snapshots are shown in Figure 6. The iodine pentoxide-containing thermite system clearly

shows a violent reaction over a period of ~ 2000 μs.
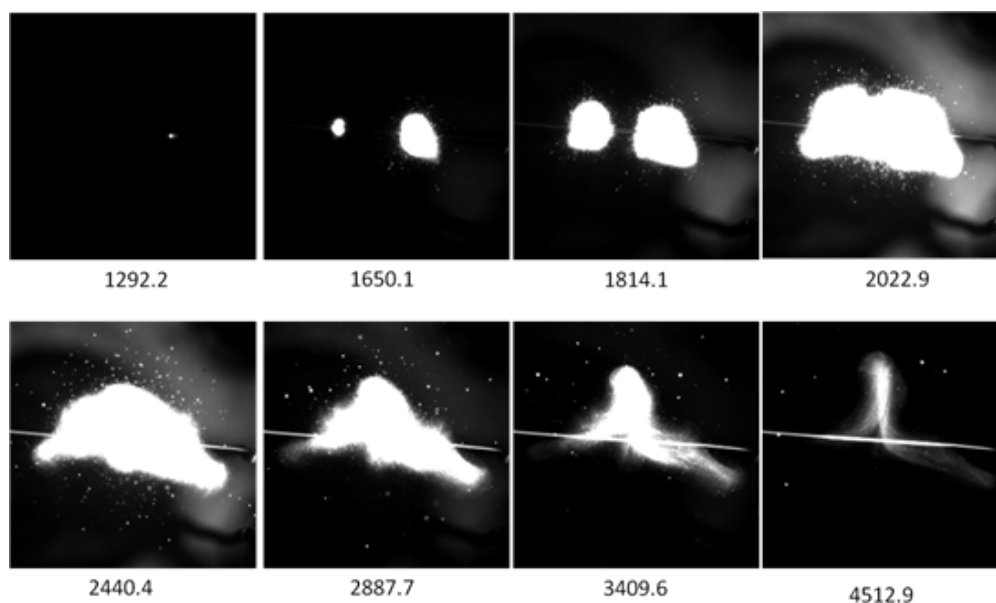
Figure 6. *Selected sequential snapshots of "nano-Al + (Fe₂O₃/I₂O₅)" burning on fast-heating wire*

in air, as captured by high-speed video camera. The labeled numbers are time elapsed (μs) after

triggering (T=883 K at 1292.2 μs). The thermite is nano-Al (ALEX) and nanocomposite oxidizer

Fe₂O₃/I₂O₅ with a Fe/I molar ratio of 4.3.

The relative combustion performance of "Al + (Fe₂O₃/I₂O₅)" thermites against reference

thermites "Al + nano-Fe₂O₃" and "Al + nano-CuO" were evaluated in the constant volume

combustion cell. Table 1 summarizes the experimental results of pressure and optical emission for thermite samples prepared with different oxidizers. Clearly the "Al + (Fe_2O_3/I_2O_5)" thermite with Fe/I molar ratio of 1.8 and 4.3 outperforms "Al + nano-Fe_2O_3" in both pressurization rate and transient peak pressure, and with shorter burning time. However, the formulated nanothermite does not exceed the performance of "Al + nano-CuO", which can be more obviously seen in the directed comparison of their pressurization rates in Figure 7.

Table 1. Combustion cell test data for thermites samples prepared with different oxidizers. All oxidizers were mixed with nano-Al powder (ALEX). Thermites sample was prepared with a specific stoichiometry assuming complete conversion of Al to Al_2O_3.

Oxidizers (w/nano-Al, φ=1)	Molar ratio of Fe/I	Prise (KPa)	Pressure rise time (μs)	Pressurization Rate (KPa/μs)	FWHM burn time (μs)	Note
Fe_2O_3/I_2O_5	0.25	15	1530	0.0896	1910	
	1.8	~112	28	45.1	183	Aerosol + iron pentacarbonyl
	4.3	~82	24	35.2	119	
	6.2	10	2970	0.0363	4280	
Nano-Fe_2O_3(ref.)	N/A	92	800	0.116	936	<50 nm, Sigma-Aldrich
Nano-CuO(ref.)	N/A	80	13	61.5	192	

In our previous study, we have argued that the pressurization occurs as a result of the

oxygen release from oxidizer's decomposition, which can occur well before significant optical emission [13]. A nanothermite system like "Al + CuO" has a rapid pressure rise signal followed by a prolonged optical signal due to the rapid oxygen release of CuO. [20] This is consistent with Table 1 results in which the pressure rise time (13 µs) of "Al + nano-CuO" is shorter than the FHWM burn time (192 µs). Unlike "Al + CuO", the pressure and optical signals of "Al + Fe_2O_3" occur almost concurrently in which the decomposition of Fe_2O_3 becomes the rate-limiting step due to the formed FeO traping O_2 in the condensed phase [8].
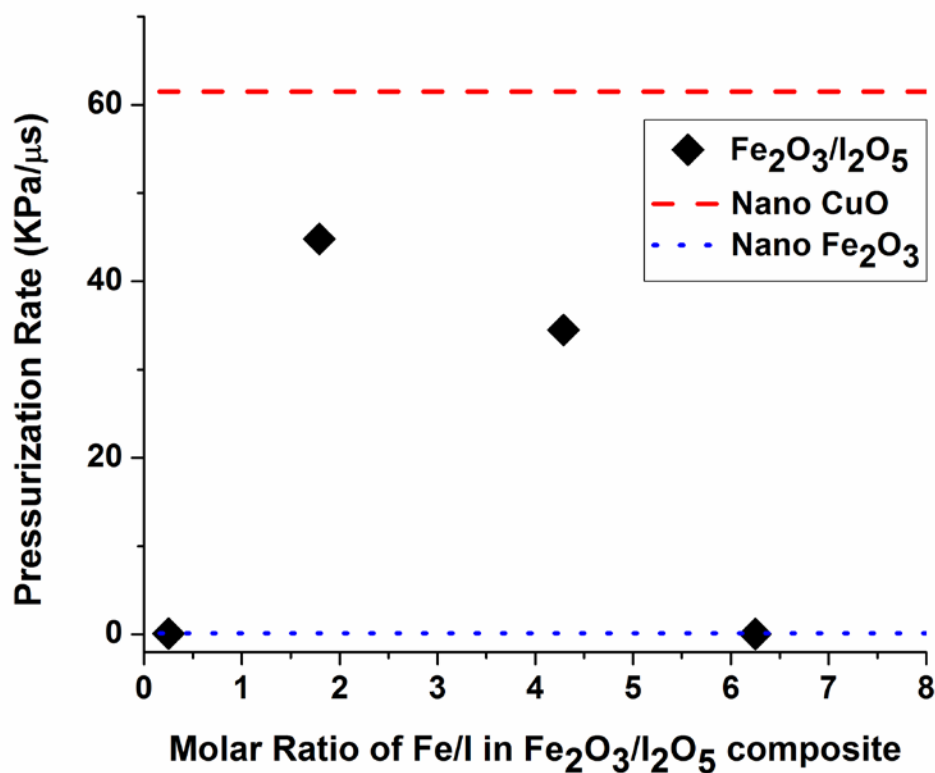
Figure 7. *Pressurization rate for thermites samples prepared with Fe₂O₃/I₂O₅ with different Fe/I molar Ratios in the core-shell particles. The nano-CuO and nano-Fe₂O₃ were used as reference oxidizers.*

The oxidizers with Fe/I molar ratio of 0.25 and 6.2 in Table 1 show the similar relative behavior as an "Al + Fe_2O_3" thermite, the pressure signal occurred almost concurrently with optical signal and the oxygen release is the rate-limiting step. This is suggestive of the fact that Fe_2O_3/I_2O_5 composite is primarily comprised of Fe_2O_3 when the Fe/I ratio is either too small or too large. If the Fe/I ratio is too small, the amount of iron oxide is not sufficient to cover the surface to protect I_2O_5 from reacting with water. While the composite will contain too much iron oxide for a higher Fe/I ratio.

With Fe/I molar ratio of 1.8 and 4.3, the thermites show the similar relative behavior as "Al + CuO", a rapid rising pressure signal followed by a prolonged optical signal, suggesting that the I_2O_5 nanoparticles well passivated by Fe_2O_3 and burn by a similar mechanism as CuO. Thus the reactivity of Fe_2O_3/I_2O_5 passivated oxidizer could be tuned by varying the Fe/I ratio.

Conclusion

In conclusion, hygroscopic strong oxidizer I_2O_5 was successfully passivated by metal oxide shell (Fe_2O_3) through a modified gas phase assisted aerosol approach. Its reactivity as an oxidizer in nanoenergetic formulations can be tuned by varying the molar ratio of Fe/I using a controlled thermal decomposition of iron pentacarbonyl. The produced Fe_2O_3/I_2O_5 passivated oxidizer was formulated into aluminum based thermite as an oxidizer and its reactivity was evaluated by constant-volume combustion cell, simultaneous fast-heated ignition wire test. The future effort will be focused on the optimization of the synthesis strategy by increasing I_2O_5 particles' size to input more iodine pentoxide content in the iron oxide shell to achieve better combustion and biocidal performances.

.

REFERENCES

1. Rossi, C.; Zhang, K.; Estéve, D.; Alphonse, P.; Thailhades, P.; Vahlas, C. *J. Microelectromech. Syst.*, **2007**, *16*, 919-930.

2. Martirosyan, K. S. *J. Mater. Chem.*, **2011**, *21*, 9400.

3. Clark, B. R.; Pantoya, M. L. *Phys. Chem. Chem. Phys.*, **2010**, *12*, 12653.

4. Chaudhuri, R. G.; Paria, S. *Chem. Rev.*, **2012**, *112*, 2373.

5. Zhang, L.; Ranadeb, M. B.; Gentry, J. W. *J. Aero. Sci.*, **2004**, *35*, 457.

6. Chemicalbook, CAS DataBase, Iodine Pentoxide, http://www.chemicalbook.com/ChemicalProductProperty_EN_CB9852918.htm (accessed Oct 2012).

7. Prakash, A.; McCormick, A. V.; Zachariah, M. R. *Nano Lett.*, **2005**, *5*, 1357.

8. Wu, C.; Sullivan, K.; Chowdhury, S.; Jian, G.; Zhou, L.; Zachariah, M. R. *Adv. Funct. Mater.*, **2012**, *22*, 78.

9. Kodas, T. T.; Hampden-Smith, M. J. *Aerosol Processing of Materials*, Wiley-VCH, New York, 1999.

10. IUPAC-NIST Solubility Database, Version 1.0, NIST Standard Reference Database 106.

11. Kim, S. H.; Liu, B. Y. H.; Zachariah, M. R. *Chem. Mater.*, **2002**, *14*, 2889.

12. Farley, C.; Pantoya, M. *J. Therm. Anal Calorim.*, **2010**, *102*, 609–613.

13. Sullivan, K.; Zachariah, M. R. *J. Propul. Power.*, **2010**, 26, 467.

14. Zhou, L.; Piekiel, N.; Chowdhury, S.; Zachariah, M. R. *Rapid Commun. Mass. Spectrom.*, **2009**, *23*, 194.

15. Zhou, L.; Piekiel, N.; Chowdhury, S.; Zachariah, M. R. *J. Phys. Chem. C.*, **2010**, *114*, 14269.

16. Giesen, A.; Herzler, J.; Roth, P. *J. Phys. Chem. A.*, **2003**, *107*, 5202.

17. Buesser, B.; Pratsinis, S. E. *Chem. Eng. Sci.*, **2010**, *65*, 5471.

18. Jain, S.; Fotou, G. P.; Kodas, T. T. *J. Colloid Interface Sci.*, **1997**, *185*, 26.

19. Jian, G.; Chowdhury, S.; Feng, J.; Zachariah, M. R. unpublished results.

20. Jian, G.; Liu L.; Zachariah, M. R. *Adv. Funct. Mater.*, **2012**, DOI: 10.1002/adfm.201202100.

Dispersion study of thermite reaction products

From the stand point of a biocidal agent, in some sense the dispersion characteristics o (i.e final solid products may be the most important component next to combustion behavior. To approach this problem we are developing an experiment to capture particle particles on slides as a function of reaction time, to be interrogated by microscopy.
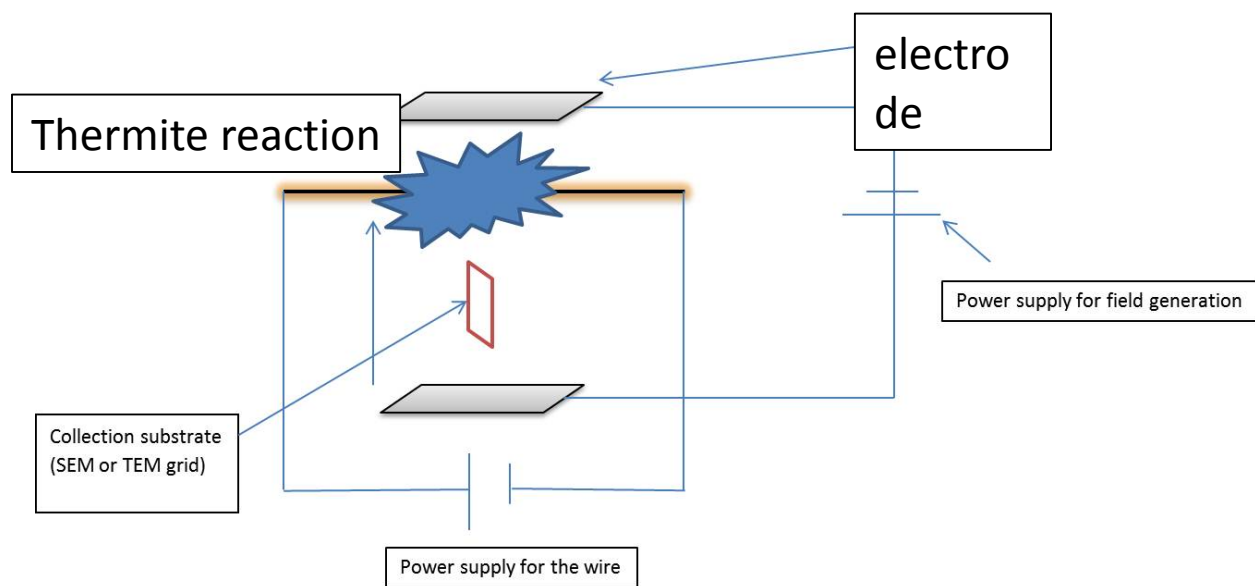
The results, as depicted in the figures, shows that the reactants definitely sinter together. Also, there are noticeably 2 different particle distributions. In the current case of Al/CuO Nano thermite, the big particles are composed of Aluminum Oxide and small ones are Copper as confirmed by the EDX analysis.

A simple coagulation calculation assuming that the products were formed from gas phase showed that it is impossible to form Al2O3 particles of such sizes(~ 5-10 microns) from gas phase, implying that the reaction was condensed phase. This implies that it is likely then that significant sintering is taking place prior to reaction. After the reaction, these particles, as they are ejected of the wire, cool down from the adiabatic flame temperature of Al/CuO (2840K). As Al_2O_3 has a high boiling point (3250K), it remains in the liquid state while copper (B.P. 2835K), the other reaction product, emanates from this sintered particle and forms the small (~50nm) particles from gas phase.

Again, the time scales predicted from the coagulation calculation did not match the sizes as seen in the TEM images. As we could not get an accurate estimate of the time scales from the high speed video, we decided to apply an electric field around the particle cloud and trigger it after specific delays so that we could get only those particles that have formed within the time interval as the field would drive away the particle cloud from the substrate. (Note: at high temperatures, the particles would be positively charged due to thermionic emission)

If we could get copper particles of various sizes at different distances from the wire then it would validate our hypothesis that the copper vapor emanates from the agglomerate and coagulates to form the small particles. We are also trying the same experiments with other materials like Tungsten Oxide/Aluminum Nano-thermite. As Tungsten has a higher boiling point than Al_2O_3, it would essentially be in molten state and won't be ejected out the way Copper is as predicted by the proposed idea.

Schematic of configuration to capture particles from thermite event

Thermite reaction

electro de

Power supply for field generation

Collection substrate
(SEM or TEM grid)

Power supply for the wire

Figures of Reaction Products at various distances from the ignition point.

A. SEM image of Al/CuO reaction products at a distance of 3.074mm from wire

10.0kV 14.6mm x450 SE(U)   100um
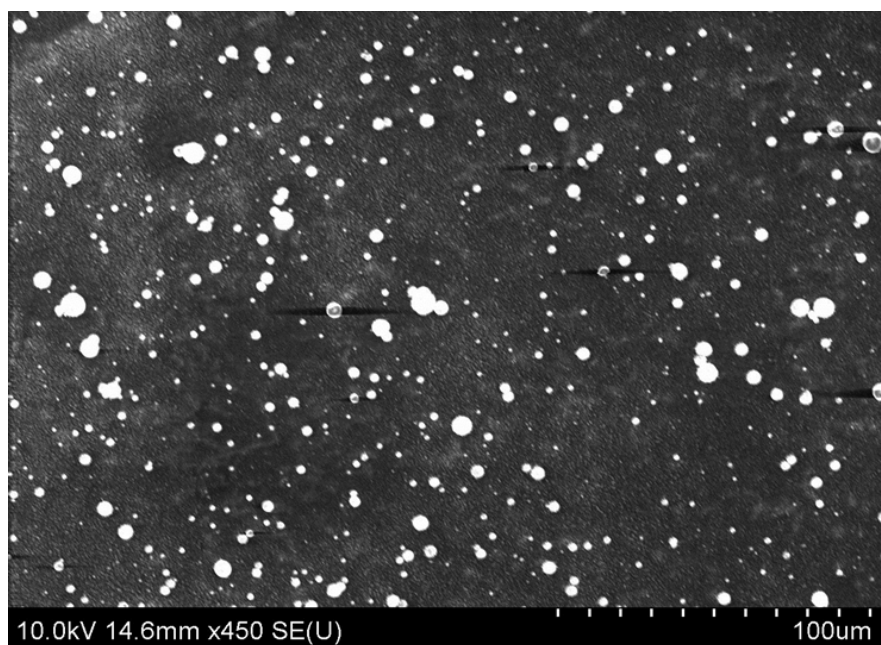
B. SEM image of Al/CuO reaction products at a distance of 0.635mm from wire

10.0kV 14.6mm x450 SE(U)   100um
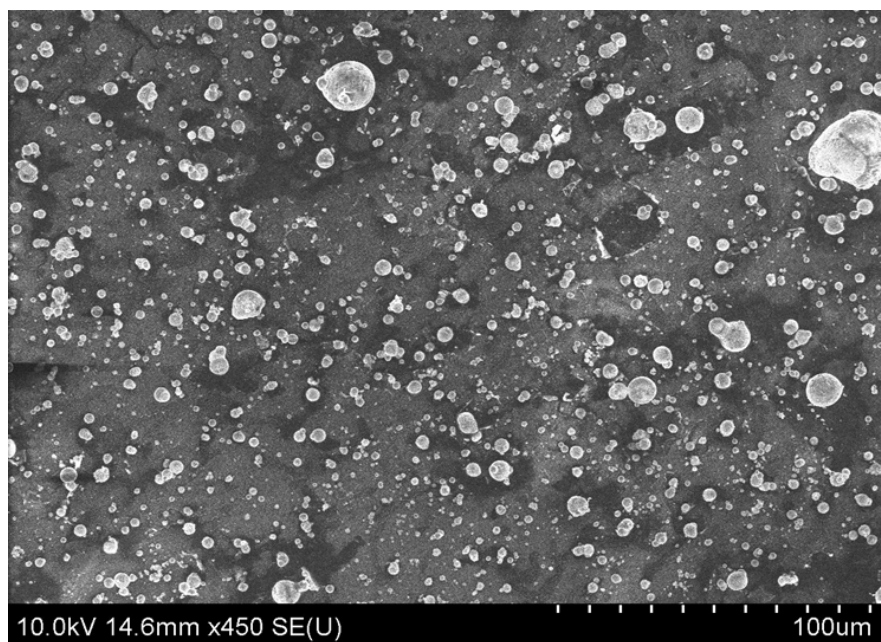
C. SEM image of Al/CuO reaction products at a distance of 3 mm from wire
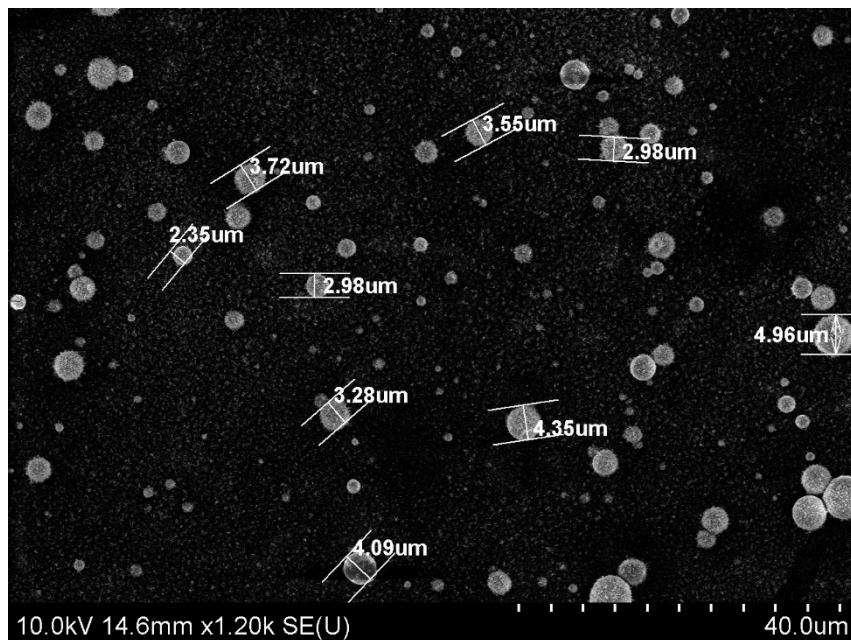
D. TEM images showing the 50nm particles, which is copper as confirmed by EDX analysis
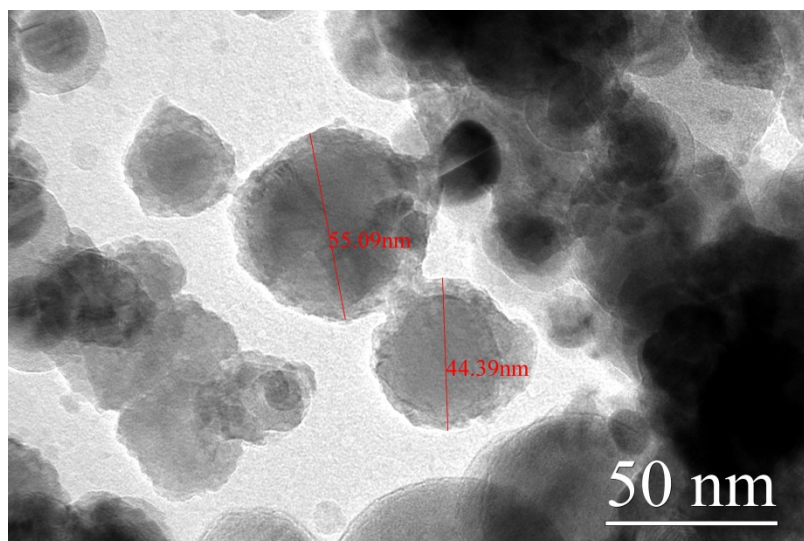
III. Results for FY-13

    **3. Development of a new class of materials : Microparticles comprised of
nanoparticles of thermite and biocide containing materials.**
      a. **Nano-Al/NC**
      b. **Nano-Al/CuO/NC**
      c. **Nano-Al/CuO/NC/I2**

    4. Dispersion characteristics of thermite samples.

1. Development of a new class of materials : Microparticles comprised of nanoparticles of thermite and biocide containing materials.

Material systems created

    a. *Nano-Al/NC*
    b. *Nano-Al/CuO/NC*
    c. *Nano-Al/CuO/NC/I2*

EXECUTIVE SUMMARY

    Due to its high enthalpy and ready availability, conventional aluminum powders with an average size of 3-20 μm, are commonly employed in solid rocket propellant and other propulsive systems. Although the energy density is increased after incorporation of micrometer-sized aluminum fuel in propellant systems, the burning rate however was not found to improve much, resulting in low rates of energy release. Additionally, the oxide coating on the surface of microsized aluminum sufficiently passivates the fuel to a high ignition temperature ~2300 K. In contrast, the use of nanoscale aluminum lowers the ignition temperature to < 1000K, with a much enhanced burning rate, and a lower ignition delay time. Unfortunately nanometallic fuels suffer from processing challenges, that have significantly retarded their utility, most primarily because their very high surface area/small particle size increases the viscosity of polymer binder and oxidizer mix, such that high mass fractions of fuel cannot be formulated.

One approach we will describe here is to maintain the nanostructure characteristics that make nanoaluminum desirable, but formulate them into a structure that is microsized. This micrometer structured particle should have the advantage that it can be processed using traditional methods for micron aluminum, while still maintaining its nano characteristics. We employ electrospray as a means to create a gel within a droplet by evaporation induced rapid aggregation of aluminum nanoparticles, containing a small mass fraction of an energetic binder. In particular, nitrocellulose is introduced into the precursor solution and serves both as the energetic polymer binder but also to tune the final particle size and morphology. In summary, gelled aluminum microspheres with a

narrow size distribution were synthesized by a one-step electrospray method. We find that the average size of the gelled microparticles can be systematically changed from 2 μm to 16 μm by increasing the nano-Al particle concentration in the precursor solution.

The microstructures of the composite particles reveal a porous gelled inner structure with nano features. Brunauer-Emmett-Teller (BET) measurements indicate a surface area of 20 m^2g^{-1} for the gelled aluminum microparticles shown in Figure 1, which is close to that for an individual ~50 nm nano aluminum particles, implying that the whole microparticle structure is accessible. The gelled aluminum microparticles show enhanced burning behavior compared to nanoaluminum (n-Al), which possibly benefits from the nitrocellulose coating and the gelled structure.

The gelled aluminum microspheres were characterized and tested for their burning behavior by rapid wire heating ignition experiments shown in Fig 2.. We attribute the fast reactivity of the gelled material to the localization of the heat release. It is well known, that nanoparticles are pyrophoric, but only when in sufficient high concentration. An isolated nanoparticle in air will not burn because of rapid heat loss to the surroundings. The gelled particle is in effect an extreme example of this phenomena. The porous nature of the gel enables rapid oxygen transport while the constrained nature of the microspheres constrains the heat released within a small volume, which promotes acceleration of the global reaction. Larger size particles contain more NC thus display a shorter ignition delay and longer burning time.

More recently we have extended the process to create mesospheres of Al/CuO nanothermite compositions containing small amounts of nitrocellulose as well as then films containing high volume loadings of metalized polymer composites that are directly sprayed to a surface.

Introduction

Due to its high enthalpy and ready availability, conventional aluminum powders with an average size of 3-20 μm, are commonly employed in solid rocket propellant and other propulsive systems.[1-3] Although the energy density is increased after incorporation of micrometer-sized aluminum fuel in propellant systems, the burning rate however was not found to improve much, resulting in low rates of energy release.[4] Additionally, the oxide coating on the surface of microsized aluminum sufficiently passivates the fuel to a high ignition temperature ~2300 K.[2, 5, 6] In contrast, the use of nanoscale aluminum lowers the ignition temperature to < 1000 K, with a much enhanced burning rate, and a lower ignition delay time.[6-12] Unfortunately nanometallic fuels suffer from processing challenges, that have significantly retarded their utility, most primarily because their very high surface area/small particle size increases the viscosity of polymer binder and oxidizer mix, such that high mass fractions of fuel cannot be formulated. [9, 13-16]

One approach to deal with this issue is to directly incorporate the nanosized metallic fuel in energetic nanofibers.[17] This is not an ideal situation either, since the fibers themselves must be processed. There are other approaches, such as arrested milling to produce micron Al with nano features. [18-23] One alternative approach we will describe here is to maintain the nanostructure characteristics that make nanoaluminum desirable, but formulate them into a structure that is microsized[24, 25]. Even though its density and energy density should be lower than micron Al, this micrometer-structured particle has the advantage that it can be processed using traditional methods for micron aluminum, while still maintaining its nano characteristics. It is also possible that the pores can be filled with other polymeric materials or additives, a topic we are currently exploring.

Electrospray approaches have been demonstrated as a simple method for the fabrication of nano/micro spheres, and is based on liquid jet break-up under the influence of a strong electric force.[26-29] Compared with other wet chemistry methods, electrospray provides a facile one-step approach to generate relatively uniform microspheres.[30] Other spraying methods can also assemble nanoparticles into microspheres.[31-33] But uniquely, the electrospray method has the advantage of producing nano/micro particles with a narrow size distribution. Additionally, precursor suspensions with high mass loading of particles and polymer solution are more easily sprayed by this electrostatic assist, making this approach particularly useful to produce polymer based composite materials. Furthermore, the possible control and tuning of microparticle composition, size and morphology by electrospray exceeds that of conventional spray methods.[34-38]

In this letter, we employ electrospray as a means to create a gel within a droplet by evaporation induced rapid aggregation of aluminum nanoparticles, containing a small mass fraction of an energetic binder. In particular, nitrocellulose is introduced into the precursor solution and serves both as the energetic polymer binder but also to tune the final particle size and morphology. The gelled aluminum microparticles show enhanced burning behavior compared to nanoaluminum (n-Al), which possibly benefits from the nitrocellulose coating and the gelled structure.

The electrospray formation of composite microparticles is conceptually simple, as illustrated in Figure 1. Aluminum nanoparticles (ALEX, <50 nm, Argonide Corp. Figure S1) are dispersed into a nitrocellulose polymer solution and electrosprayed to form micro-droplets, which are further dried to form microparticles after solvent removal. In a typical experiment, aluminum nanoparticles were dispersed into a colloidon solution (~17 mg/ml), and then sonicated and stirred to form a suspension. The suspension was then injected by coaxial capillary tubes (Figure S2), the

inner diameter of inner tube (22 gauge steel) and the outer tube (17 gauge steel) is 0.41 mm and 1.07 mm, respectively, fed by two syringe pumps and electrosprayed to form gelled aluminum microparticles. Details of the experimental process could be found in supporting information. Any operations were carefully processed with using gloves in case of electric shock, and the electrospraying process should be kept in a hood fume to release the organic solvent vapor.
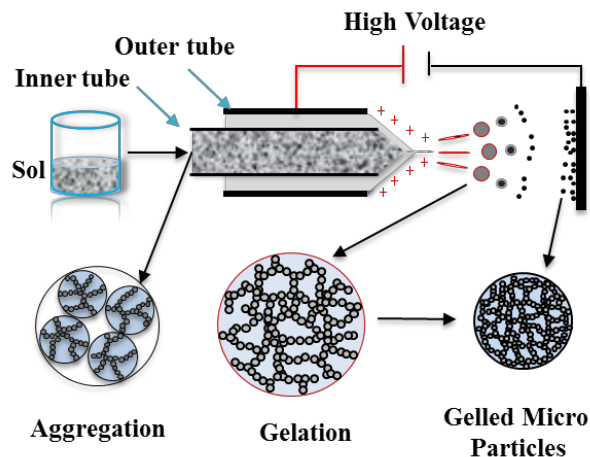
Figure 1. Schematic of electrospray formation of gelled nano-Al microspheres.

Figure 2 shows scanning electron microscopy (SEM) image of electrosprayed gelled samples. The particles are found to be highly spherical with diameters of several micrometers, which can be varied depending on the Al nanoparticle concentration, and nitrocellulose content.
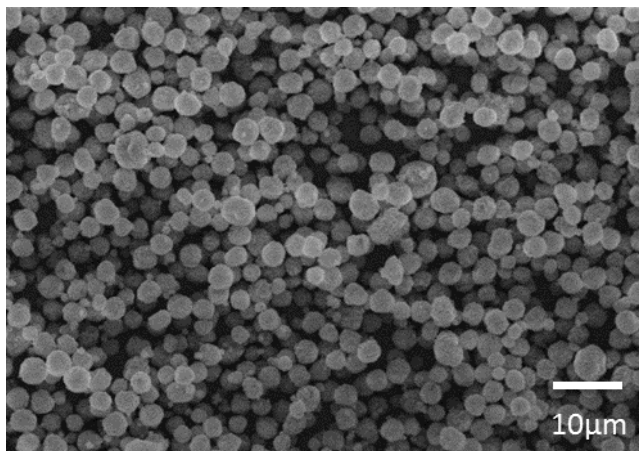
Figure 2. SEM image of aluminum microspheres produced by electrospraying. (Inner tube flow rate: 0.5ml/h)

66

Unlike the sample of Figure 2, which employed both the inner and outer coaxial needle, the sample of Figure 3 only used inner tube. A close up view in Figure 3a reveals a porous structure of gelled aluminum microparticles with a diameter of ~16 µm (10 wt. % NC). The flow rate in this single needle process was 4.5 ml/h. According to the relationship between droplet size and flow rate[26, 36], the average size of these microspheres should be larger than those produced by the coaxial needle electrospray process shown in Figure 2, which is consistent with our results. Also seen in Figure 3a are some smaller particles, which can be ascribed to fission of the primary droplets by Coulombic crowding.[39] Cross-section SEM images in Figure 3b and a high resolution SEM image in Figure 3c further reveals the porous structure of the microparticle, which shows that while some cavities exist within the microparticles, for the most part the gel extends throughout the particle. It appears however that the surface region is denser than the interior, presumably due to aggregates on the surface having more opportunity to move and rearrange relative to the interior aggregates. The surface topology at still higher magnification (Figure 3c) shows that the structure has retained the primary particle structure comprising the gel. Brunauer-Emmett-Teller (BET) measurements indicate a surface area of 20 m^2g^{-1} for the gelled aluminum microparticles shown in Figure 3a-c, which is close to that for an individual ~50 nm aluminum nanoparticle, implying that the whole microparticle structure is accessible. Thus on a per unit mass basis the specific surface area of the gelled microparticle is equivalent to the individual primary particles. This latter point is important for the expectation of high or comparable reactivity to the nascent aluminum nanoparticles. On the other hand one should expect that it is the exposed outer surface of the mesosphere that will have the most impact on the viscous behavior in a formulation. As shown in Figure 1, the chains of NC with nano-Al aggregate in the prepared semi-diluted sol. With the evaporation of solvent within the droplets, the aggregate chains experience crowding and jam against each other to progressively create a three-dimensional porous network, which serves as the main structural skeleton, that is stabilized by the nitrocellulose polymer binder to create the gelled microparticles.[40] The SEM image and elemental mapping clearly demonstrate that the gelled aluminum microparticle has a homogeneous structure with uniform inter-dispersion of nano-Al and nitrocellulose polymer binder (Figure.S4).
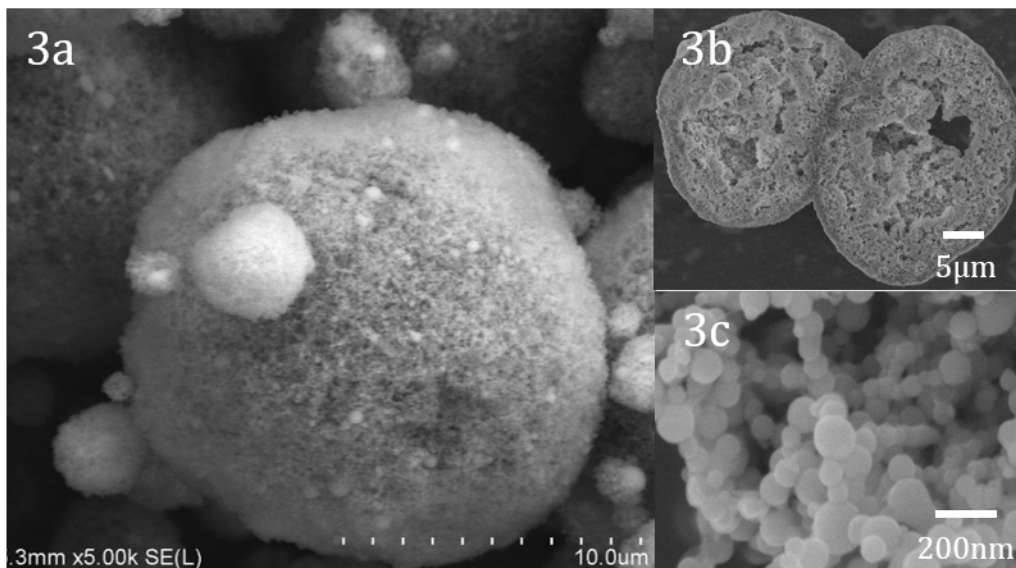
Figure 3. SEM images of (a) a typical gelled microsphere, (b) cross section, (c) High magnification SEM image of gelled microsphere

We find that the average size of the gelled microparticles can be systematically changed from 2 µm to 16 µm by increasing the nano-Al particle concentration in the precursor solution, as shown in Figure 4. The fact that the particle size increases so dramatically by changing particle loading implies that larger droplets are being generated by the electrospray, presumably due to the increased precursor solution viscosity rises with increased particle loading.[42-43] We found we could create even larger microspheres (~40 µm) by further increasing the flow rate (Fig. S7).
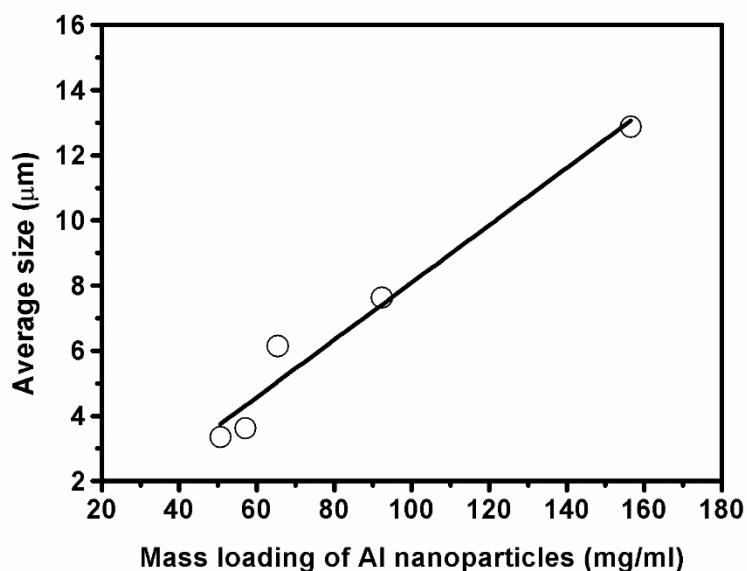
Figure 4. Average gelled particle size can be systematically increased by adding more nano-Al

The reactivity of these gelled microparticles was evaluated by coating a thin platinum wire (dia. 76 μm), which could be rapidly heated to measure the ignition delay time and temperature.[44] The wire was ramped to ~1600 K in 3 ms, at a heating rate of ~4×10^5 K·s^{-1}.[45] The burning process was recorded by a high-speed camera at the speed of 67000 frames per second to determine the time of sample ignition relative to the heating pulse, and temperature of the wire. For comparison purposes, nano-Al particles, nano-Al mixed with nitrocellulose as well as microsized aluminum were also tested.
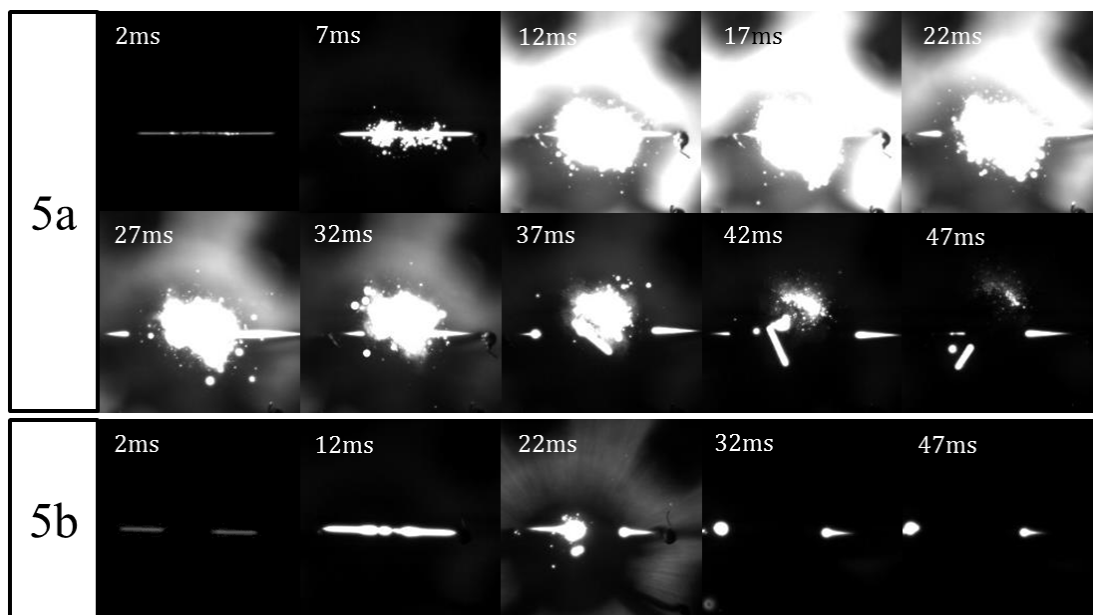
Figure 5. High speed video images: (a): Gelled aluminum microparticles; (b) Nanoaluminum The labeled numbers are time elapsed after triggering.

We propose the following conceptual mechanism of this enhanced burning as illustrated in Figure 6. With nitrocellulose's low decomposition temperature (170 C) we expect gas generation to occur early during the heating process and combustion to commence with the oxygen within the porous structure. Unlike isolated nanoparticles undergoing oxidation that have high heat loss to the surrounding, rapid reaction within the gelled microparticle should be self-accelerating, because the heat of reaction is trapped within the microparticle, resulting in cooperative heating. Eventually it is also possible that this rapid accumulation of heat, and increasing rapid reaction lead to sufficient gas generation so as to overpressure the structural integrity of the gel, and shatter it into isolated burning nanoparticles as evidenced by the large fire ball seen in Figure 5a.
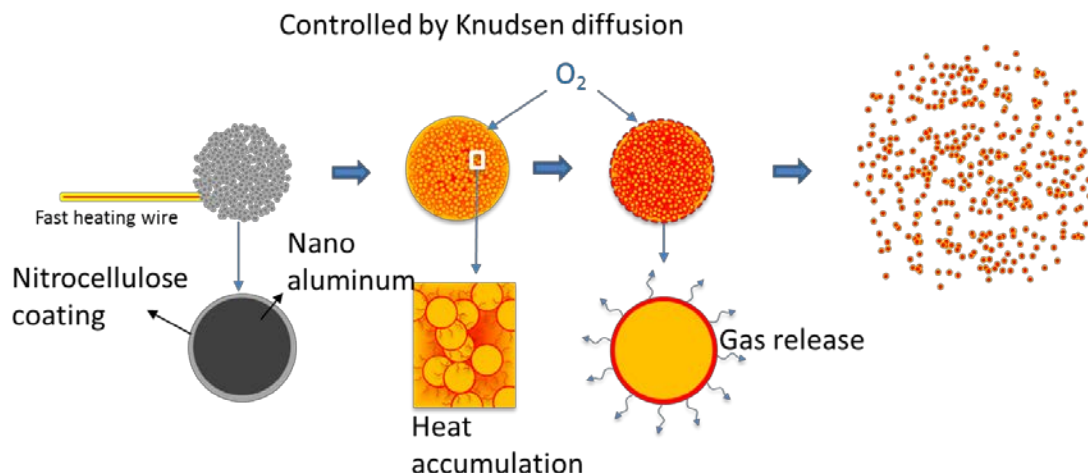
Figure 6. Proposed combustion process of gelled Al micro particles.

The results of rapid wire heating experiments are presented in Table 1. Solid micron aluminum which has approximately the same size distribution as gelled microspheres, could not be ignited by our fast-heating wire because of the much higher ignition temperature (~2300 K) needed exceed the capabilities of our wire (1600 K).

We noticed that for gelled particles, the ignition delay time is largely reduced from 14 ms to ~3.5 ms by adding 3 wt. % NC. With the further increase of NC, the gelled microspheres show shorter ignition delay, decreasing to 0.3 ms (10 wt. %) while the burning duration increasing from 46 ms (3 wt. %) to 64 ms (10 wt. %). It has been found that the burning time of Al/NC composites is 2~5 times longer than Al nanoparticles. However, the burning time of the nano Al and NC (10 wt. %) mixture remains the same as the pure Al nanoparticles.

As seen in Figure 5 and Table 1, the gelled aluminum microparticle (10% NC) showed by far the highest burning duration of ~64 ms and the shortest ignition delay time of ~0.26 ms, indicating its better combustion performance than nano-Al powder (or nano-Al/NC mixture). The addition of NC serves as both a binder and as an energetic source, which could decrease the ignition delay due to its low decomposition temperature. We attribute the fast reactivity of the gelled material to the localization of the heat release. It is well known, that nanoparticles are pyrophoric, but only when in sufficient high concentration. An isolated nanoparticle in air will not burn because of rapid heat loss to the surroundings. [46] The gelled particle is in effect an extreme example of this phenomena. The porous nature of the gel enables rapid oxygen transport while the constrained nature of the microspheres constrains the heat released within a small volume, which promotes

acceleration of the global reaction. With 1 wt. % NC, the nano-Al agglomerates together instead of forming gelled microspheres (Figure S6), which consequently has the similar burning behavior as the nano-Al. Increasing NC content results in an increase in particle size. As seen in Table 1 the particles with increased NC have a shorted ignition delay time, but since increasing NC also leads to larger particles we observe an increased burning time.

Table 1. Ignition delay and burn time averaged over three experiments for different formulations. The fast-heating snapshots of micron size Al, the mixture of nano Al and NC (10%, by mass) can be found in supporting materials (Figure.S5a and Figure.S5b, respectively)

Material	Ignition delay time /ms	Burn time /ms
Micron size Al (3.0-4.5 μm)	No ignition	0
Nano Al powder (50 nm)	14.1	14
Mixture of nano Al and NC (10%)	7.2	14
Gelled particles (NC, 1% by mass)	13.2	18
Gelled particles (NC, 3 wt. %, mean size: 2.0 μm)	3.5	46
Gelled particles (NC, 6.5 wt. %, mean size: 3.1 μm)	1.1	56
Gelled particles (NC, 10 wt. %, mean size: 11.1 μm)	0.3	64

In summary, gelled aluminum microspheres with a narrow size distribution were synthesized by a one-step electrospray method. The microstructures of the composite particles reveal a porous gelled inner structure with nano features. We show that the average microparticle size can be tuned over a relatively large range. Most interesting however is that these gelled aluminum microspheres show superior reactivity, than the nascent nanoparticle comprising the gelled particle. We expect that the unique gelled microparticle structure with nano building blocks could potentially circumvent the problems associated with trying to utilize nanometals in propellants.

REFERENCES

1. Arkhipov, V. A.; Korotkikh, A. G. *Combust. Flame* **2012,** *159*, 409-415.

2. Sadeghipour, S.; Ghaderian, J.; Wahid, M. A. *Advances in aluminum powder usage as an energetic material and applications for rocket propellant*; 4th International Meeting of Advances In Thermofluids, Melaka, Malaysia, Oct 3-4, 2011; American Institute of Physics: Melville, New York, **2012,** *1440*, 100-108

3. Dokhan, A.; Price, E.; Seitzman, J.; Sigman, R. *P. Proc. Combust. Inst.* **2002,** *29*, 2939-2946.

4. Escot, B. P.; Chauveau, C.; Gökalp, I. *Aerosp. Sci. Technol.* **2007,** *11*, 33-38.

5. Dreizin, E. L. *Prog. Energy Combust. Sci.* **2009,** *35*, 141-167.

6. Yetter, R. A.; Risha, G. A.; Son, S. F. *Proc. Combust. Inst.* **2009,** *32*, 1819-1838.

7. Jian, G.; Piekiel, N. W.; Zachariah, M. R. *J. Phys. Chem. C*, **2012,** *116*, 26881-26887

8. Muthiah, R.; Krishnamurthy, V.; Gupta, B. *J. Appl. Polym. Sci.* **1992,** *44*, 2043-2052.

9. Meda, L.; Marra, G.; Galfetti, L.; Severini, F.; De Luca, L. *Mater. Sci. Eng., C.* **2007,** *27*, 1393-1396.

10. Puszynski, J. A.; Bulian, C. J.; Swiatkiewicz, J. J. *J. Propul. Powder.* **2007,** *23*, 698-706.

11. Sullivan, K.; Young, G.; Zachariah, M. *Combust. Flame* **2009,** *156*, 302-309.

12. Armstrong. R. W.; Baschung, B.; Booth, D. W.; Samirant, M. *Nano Lett.* **2003,** *3*, 253-255.

13. Zhi, J.; Shu-Fen, L.; Feng-Qi, Z.; Zi-Ru, L.; Cui-Mei, Y.; Yang, L.; Shang-Wen, L. *Propellants Explos. Pyrotech.* **2006,** *31*, 139-147.

14. Lebedeva, E. A.; Tutubalina, I. L.; Val'tsifer, V. A.; Strel'nikov, V. N.; Astaf'eva, S. A.; Beketov, I. V. *Combust. Explo. Shock Waves* **2012,** *48*, 694-698.

15. Wen, D. *Energy Environ. Sci.* **2010,** *3*, 591-600.

16. Galfetti, L.; DeLuca, L.; Severini, F.; Colombo, G.; Meda, L.; Marra, G. *Aerosp. Sci. Technol.* **2007,** *11*, 26-32.

17. Yan, S.; Jian, G.; Zachariah, M. R. *ACS Appl. Mater. Interfaces* **2012,** *4*, 6432-6435.

18. Zhang, S.; Badiola, C.; Schoenitz, M.; Dreizin, E. L. *Combust. Flame* **2012**, *159*, 1980-1986.

19. Sippel, T. R.; Son, S. F.; Groven, L. J. *Propellants Explos. Pyrotech.* **2013**, *38*, 286-295.

20. Schoenitz, M.; Ward, T. S.; Dreizin, E. L. *Proc. Combust. Institute* **2005**, *30*, 2071-2078.

21. Schoenitz, M.; Ward, T. S.; Dreizin, E. L. *Mater. Res. Soc. Proc.* **2003**, *800*, 1-6.

22. Dreizin, E. L. *Prog. Energy Combust. Sci.* **2009**, *35*, 141-167.

23. Sippel, T. R.; Son, S. F.; Groven, L. J. *Propellants Explos. Pyrotech.* **2013**, *38*, 286-295.

24. Polshettiwar, V.; Baruwati, B.; Varma, R. S. *ACS Nano* **2009,** *3*, 728-736.

25. Yu, D. G.; Yang, J. H.; Wang, X.; Tian, F. *Nanotechnol.* **2012,** *23*, 105606.

26. Loscertales, I. G.; Barrero, A.; Guerrero, I.; Cortijo, R.; Marquez, M.; Ganan-Calvo, A. M. *Science* **2002,** *295*, 1695-1698.

27. Jaworek, A. *Powder. Technol.* **2007,** *176*, 18-35.

28. Jaworek, A.; Sobczyk, A. T. *J. Electrostat.* **2008,** *66*, 197-219.

29. Bock, N.; Woodruff, M. A.; Hutmacher, D. W.; Dargaville, T. R. *Polymers* **2011,** *3*, 131-149.

30. Chakraborty, S.; Liao, I. C.; Adler, A.; Leong, K. W. *Adv. Drug Delivery Rev.* **2009,** *61*, 1043-1054.

31. Takashima, Y.; Saito, R.; Nakajima, A.; Oda, M.; Kimura, A.; Kanazawa, T.; Okada, H. *Int. J. Pharm.* **2007**, *343*, 262-269.

32. Peltonen, L.; Valo, H.; Kolakovic, R.; Laaksonen, T.; Hirvonen, J. *Expert Opin. Drug Deliv.* **2010**, *7*, 705-719.

33. Yu, Z.; Garcia, A. S.; Johnston, K. P.; Williams, R. O. *Eur. J. Pharm. Biopharm.* **2004**, *58*, 529-537.

34. Hogan, C. J.; Yun, K. M.; Chen, D.-R.; Lenggoro, I. W.; Biswas, P.; Okuyama, K. *Colloids Surf., A.* **2007,** *311*, 67-76.

35. Almeria, B.; Deng, W.; Fahmy, T. M.; Gomez, A. *J. Colloid Interface Sci.* **2010,** *343*, 125-133.

36. Ganan-Calvo, A. M.; Davila, J.; Barrero, A. *J. Aerosol Sci.* **1997**, *28*, 249-275.

37. Loscertales, I. G.; Barrero, A.; Guerrero, I.; Cortijo, R.; Marquez, M.; Ganan-Calvo A. M. *Science* **2002**, *295*, 1695-1698.

38. Gañán-Calvo, A. M. *Phys. Rev. Lett.* **1997**, *79*, 217-220.

39. Bock, N.; Dargaville, T. R.; Woodruff, M. A. *Prog. Polym. Sci.* **2012,** *37*, 1510-1551.

40. Abete, T.; Del Gado, E.; de Arcangelis, L. *Polym. Compos.* **2013,** *34*, 259-264.

41. Gromov, A.; Ilyin, A.; Förter-Barth, U.; Teipel, U. *Propellants Explos. Pyrotech.* **2006**, *31*, 401-409.

42. Omland, T. H.; Dahl, B.; Saasen, A.; Svanes, K. Amundsen, P. A. *Annual transactions of the Nordic rheology society*, **2005**, *13*, 107-110

43. Bicerano, J.; Douglas, J. F.; Brune, D. A. *Rev. Macromol. Chem. Phys.* **1999**, *C39*, 561-642.

44. Wu, C.; Sullivan, K.; Chowdhury, S.; Jian, G.; Zhou, L.; Zachariah, M. R. *Adv. Funct. Mater.* **2012**, *22*, 78-85.

45. Jian, G.; Piekiel, N. W.; Zachariah, M. R. *J. Phys. Chem. C* **2012**, *116*, 26881-26887.

46. Krause, U.; Schmidt, M, Lohrer, C. A. *J. Loss Prev. Process Ind.* **2006**, *19*, 218-226.

2. Dispersion characteristics of thermite samples.

EXECUTIVE SUMMARY

Stoichiometric mixtures of aluminum based nano thermites were prepared for three different oxidizer formulations, Al/CuO, Al/WO$_3$, Al/Bi$_2$O$_3$. One of the major issues of nano thermite combustion, the nature of the oxidizer transport, is addressed in this study. The three mixtures were exploded on fine platinum wire at rates of ~10^5 K/s and the products were collected on a substrate on which surface analytics was performed using electron microscopy. The results show two unique particle distributions, one of which is formed from condensed phase reactions and the other from vapor phase coagulation. The relative mass fractions of the two particle distributions was calculated using image processing software and the calculated result showed that the large particles constituted approximately 80% of the mass for all the three thermite mixtures. This result shows that majority of the energy release of the thermite reactions occurs through the condensed phase. EDX analysis was performed to analyze the product composition. Based on these results a phenomenological mechanism for the nano aluminum based thermite reaction is proposed.

I.   Introduction

Nano scale reactive composites or metastable intermolecular composites (MIC's) are an increasingly active area of research in the field of propulsion and energetics, resulting from their high energy densities, high propagation velocities and low diffusion length scales. Aumann et al. [1] were the first to show that there was a significant difference in the reactivity of Nano sized thermite mixtures of Al/MoO$_3$ (200-500 nm) over the micron sized counterparts. When compared to the conventional mixtures, their experimentally observed reactivity was several orders of magnitude greater owing to the reduction in diffusion length scales. In addition to facilitating increased reactivity, MIC's boast higher control of specific energy release rate by altering the stoichiometry in the fuel oxidizer matrix or by changing the constituents with varying packing densities. Numerous experiments have been performed using halogen-containing compounds (e.g.

PTFE or Teflon) with Aluminum nanoparticles. The halogen in these oxidizers is believed to modify the transport properties of the alumina shell, formed as a result of environmental oxidation, which affects the reactivity of the mixture [18, 19].

Of all nano-scale reactive composite fuels investigated, the combustion of nano aluminum has been the most frequently studied. Several mechanisms have been proposed from such publications including pressure build-up resulting in quiescent shell rupture [3] and even possibly leading to a more violent event, resulting in spallation [4]. Most researchers consider diffusion of ionic aluminum and oxygen species across the oxide shell to be controlling processes. Rai et al. [2] have developed a power law relation for the aluminum nano particle oxidation that differs slightly from the traditional droplet combustion owing to the added effect of diffusion of oxygen and aluminum across the alumina shell which undergoes polymorphic phase transformation. Trunov et al. [5] have proposed a multi stage oxidation process for aluminum particles which includes both species transport and phase changes in the oxide shell. More recently studies have suggested that in addition to the volumetric expansion of the aluminum core, strong electric fields induced in the oxide shell can drive the aluminum cation diffusion across the shell [23, 24].

Such observations of the interesting reactive properties of MIC's have drawn attention to understanding the reaction from a mechanistic standpoint, its initiation and propagation, under high heating rates which are characteristic of a combustion event. Sanders et al. [6] studied the reaction propagation of multiple nano-thermite mixtures at varying densities and stoichiometric ratios. They emphasized the positive effects of having mobile species, which aid in the convective heat transfer, on the reaction propagation speeds. In addition, several studies have reported the development of reaction models for the mechanistic studies of these energetic composites. For example, Stamatis et al. [21], employed a multi-step model to describe the heterogeneous processes occurring during the heating of the Al/CuO nano composite. This study couples a low temperature reaction kinetics model, and a mass transfer limited model for species transport across the alumina shell. More recently, the work by Jian et al. [22] documented the transient evolution of vapor species at high temperatures. This model proposes that the molten aluminum core diffuses out of the alumina shell, with an effective diffusion constant of ~10^{-10} cm^2/s.

Most investigations performed by our group revolve around the utilization of Time of Flight Mass Spectrometry which can temporally identify atomic and molecular products that form from these redox reactions. Several studies have been conducted to explain the role of the metal oxidizer and relative importance of the oxygen release on the reactivity. Zhou et al. [7] have previously studied the role of oxygen release and have concluded that it is critical to facilitate the thermite reaction and subsequent propagation. Similarly, other studies can be found on the characterization of the reaction mechanism based on the rate limiting step being the diffusion of aluminum or the oxygen release from the metal oxide. Some of these studies involve simultaneous pressure and optical signal measurements, comparison of flame speeds in a burn tube etc. [8], [9], [20].

One of the outstanding issues regarding the role of the oxygen carrier in the MIC is whether oxygen is directly released from the oxidizer or if oxygen, in the form of an anion, is transported at the interface between fuel and oxidizer. The latter case may be defined as a condensed state process, in which little or no aluminum - oxygen reaction occurs in the vapor phase. In a recent work done by our group, we stress on the importance of gas phase oxygen release on the ignition of the reactive composites [25]. The study compared the oxygen release temperatures and the ignition temperatures of 10 different reactive composites. The study concluded that the presence of gaseous oxygen need not be a necessary prerequisite for the ignition of all nano composite thermite formulations, implying that a condensed phase reaction mechanism is still prevalent in some of the MIC's. The current study seeks to evaluate these two competing processes i.e., condensed phase vs. vapor phase oxidation, through a post-combustion analysis of rapidly quenched product particles.

II.   Experimental Approach

Several researchers have previously investigated quenched aluminum particles to extract useful information about their burning. Drew et al. [10] studied quenched aluminum particles that were cooled by a draught of helium gas. They opined that impingement quenching was not the ideal method for particle quenching as it resulted in erratic observations due large overlapping of material on the substrate. In this work, we use the same technique of impingement quenching but

here we are not focusing on the transient evolution of particles but our focus is on events that suggest considerable sintering, and a mechanistic evolution of the nature of the burning process.

The basic approach to this study is to ignite various MIC combinations on rapidly heated fine wire, and quench product particles on a substrate at short distances away from the wire so that post-inspection by microscopy and surface analytics can be performed.

Materials and Preparation:

Commercially available Aluminum nanoparticles (ALEX) with an average particle size of 50nm, procured from Argonide Corp., were used in this study. These particles had a core shelled structure with an active aluminum content of 70% which was confirmed by thermo gravimetric measurements [12]. These ALEX nanoparticles were ultra-sonicated in a hexane suspension for approx. 20 minutes with three different metal oxide nanopowders. The metal oxide nano powders used in this study were Copper (II) Oxide (CuO), Tungsten Oxide (WO_3), Bismuth Trioxide (Bi_2O_3) (all from Sigma Aldrich Corp. and <100nm). After ultra-sonication, the intimately mixed thermite mixture was micro pipetted onto a platinum wire of 76 µm diameter. The three systems chosen here, exhibit varied combustion characteristics in terms of propagation speeds, pressurization rates and burn times [6], [8]. These systems were extensively studied by Sanders et al. [6] employing the pressure cell, open tray and instrumented burn tube methods to study the reaction mechanisms of these MIC's. They concluded the importance of the presence of vapor phase/ mobile components to enhance the propagation velocities and proposed a shift in the heat transfer mechanism from convective mode to conductive when the density of the mixture increased. A particular case of interest was the performance of the Al/Bi_2O_3 mixtures at low densities which displayed a conductive heat transfer mechanism, in addition to convective, due to the localized increase in densities resulting from the drastic pressure rise. The adiabatic temperatures vary with the choice of the thermites, with Al/WO_3 mixture exhibiting a very high adiabatic flame temperature compared to the Al/CuO formulation. From pressurization rate, and the temporal behavior of optical emission, Sullivan et al. [8] showed significant differences in case of Al/CuO and Al/WO_3 in regard to the pressure peak vs. the optical peak which shows that Al/WO_3 nano composite does not produce much gas species until the system temperatures are very

high. Jian et al. [7] points out that the Al/Bi$_2$O$_3$ system ignites almost 700K below its oxygen release temperature while the Al/WO$_3$ system does not produce any gas within the experimental range of temperature. The Al/CuO mixture is observed to closely follow the expectation that ignition is correlated to oxygen release from the oxidizer. Apart from these variations in their respective combustion behavior, these metal oxides exhibit very different physical properties with CuO and WO$_3$ exhibiting higher melting and boiling temperatures compared to Bi$_2$O$_3$. The respective reduced metals also show similar behavior in regard to the bulk physical properties with Bismuth having the lowest boiling and melting point, as outlined in Table 1.

Table 1: Thermo-Physical properties of the thermite mixtures, adapted from [8].

| Thermite Mixture (Al/Metal Oxide)	Adiabatic Flame Temperatures (K)	Metal Oxide Melting point (K)	Metal Oxide Boiling point (K)	Metal Melting point (K)	Metal Boiling point (K)
Al/CuO	2837	1599	2273	1357	2843
Al/WO$_3$	3447	1746	2110	3695	5933
Al/Bi$_2$O$_3$	3253	1098	2163	545	1837
Aluminum Oxide	-	2313	3250	-	-

These dissimilarities provide the motivation for choosing these three materials for the current work. All three, show significantly different behavior in terms of ignition point, combustion intensity, physical properties and gas release. The question is how the nature of the product distribution would vary for these disparate systems, and if the analysis of the product could shed some light on their respective mechanisms.

T-Jump Wire Ignition and Particle Collection:

The details of the wire heating system comprising the mass spectrometer and power source can be obtained in another work by Zhou et al. [11]. In these set of experiments the primary modification

was the ability to capture reproducibly, post-combustion material on substrates. This entire assembly was mounted upon a bi-axial linear translational stage (Newport Research Corp). This stage had two manually controlled micrometer actuators with a resolution of 25.4 µm. The collecting substrate was a separately attached SEM stage with a layer of carbon tape on it so as to improve the conductivity of the sample. An image depicting the combustion event can be seen in Figure 1. By moving the Z direction micrometer we could collect the product particles on the substrate at distances on the order of several millimeters with accuracy over several micrometers. The impingement criteria were a separation of 1 mm for the "near" substrate and 3 mm for the "far" substrate conditions. A similar arrangement was used for the TEM samples, where a Nickel TEM grid was placed on the stage. A high speed digital camera (Phantom V12.1) was used to capture the video of the reaction from which characteristic transit times could be extracted.
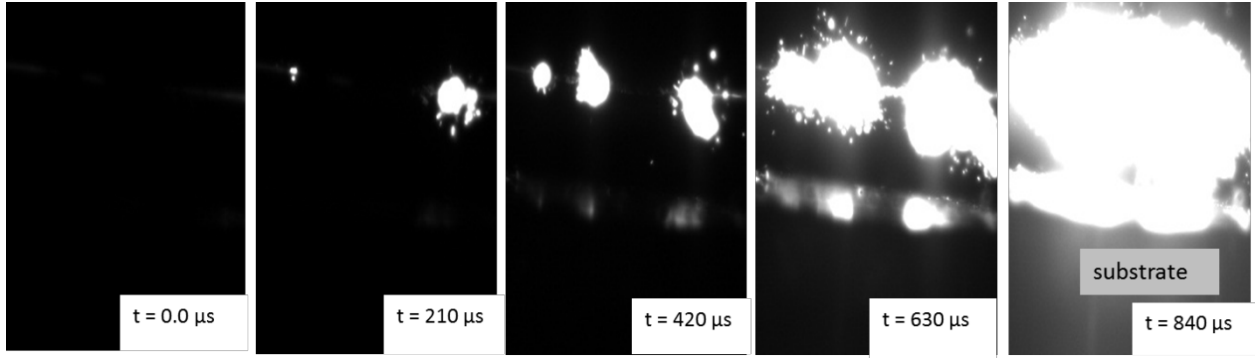

Figure 1: Temporal video snapshots of Al/WO$_3$ nano-composite combustion on 70 micron Pt wire, Heating rate = ~2*10^5 K/s, Time shown in µs

III.   Electron microscopy

A Hitachi SU 70 SEM and a JEOL FEG TEM was used for the electron microscopy evaluation. Particles were collected at two distinct separation distances to make a fair comparison of the particle evolution. The SEM images obtained for the three MIC's are shown in the subsequent images with an approximate time scale taken for the particles to reach the substrate. These time scales were obtained from the high speed video of the combustion sequence, where the individual frames, right from the start of the explosion of the composite off the wire till the point it impinges the substrate, were analyzed to get the approximate transit time.

Al/CuO Nano Composite

Figure 2 and 3 shows moderate and high magnification SEM images of the residue collected at the near and far substrate condition for the Al/CuO case. From these images we can see that there is a significant number of large particles (in comparison to the nanoscale starting materials) that have formed from the thermite reaction, some of which are as large as 20 µm. At still higher magnifications, using a JEOL FEG TEM we observe a layer of much finer particles as shown in Figure 4. Layers of particles were also visible on the surface of the larger particles as seen in Figure 3b. Figure 3a is a BSE image of the particles found for the impingement criteria of 1 mm. The brighter part is copper owing to its higher molecular weight. As we can see, both these particles are on the order of 10 microns in diameter.
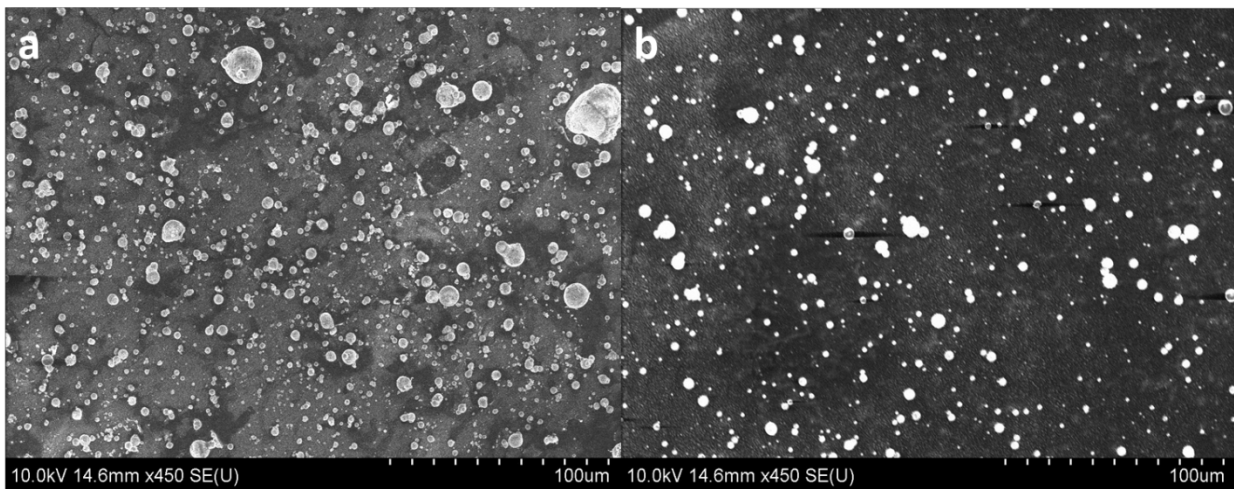
Figure 2: Post-combustion SEM images of Al/CuO Nano Thermite collected at various distances. a.) Time for impingement = 90 µs, Separation of the collecting substrate: 1 mm. b.) Time for impingement = 350 µs, Separation of the collecting substrate: 3 mm
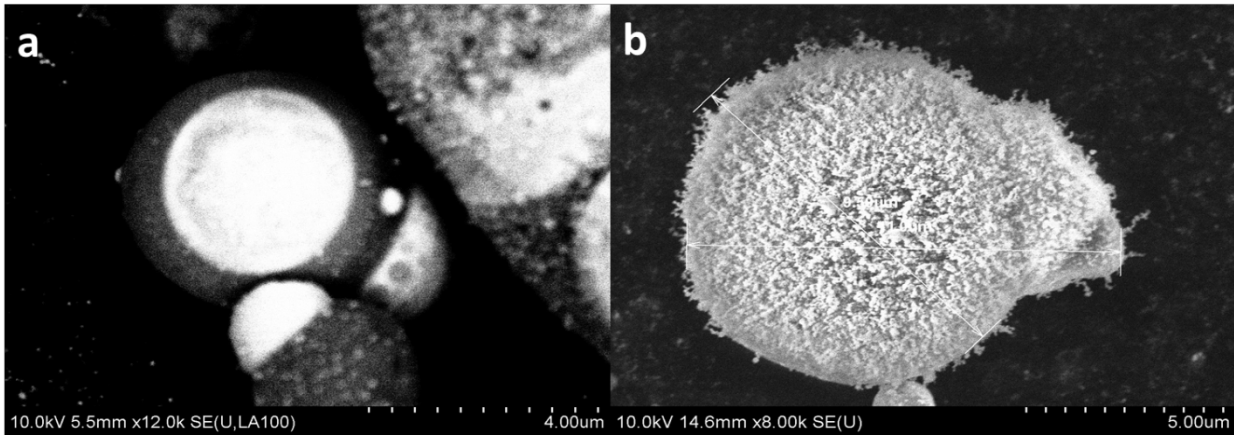
Figure 3: Post Combustion high magnification SEM images showing surface morphology at the various separation distances for Al/CuO. a.) Time for impingement = 90 µs, Separation of the collecting substrate: 1 mm. b.) Time for impingement = 350 µs, Separation of the collecting substrate: 3 mm
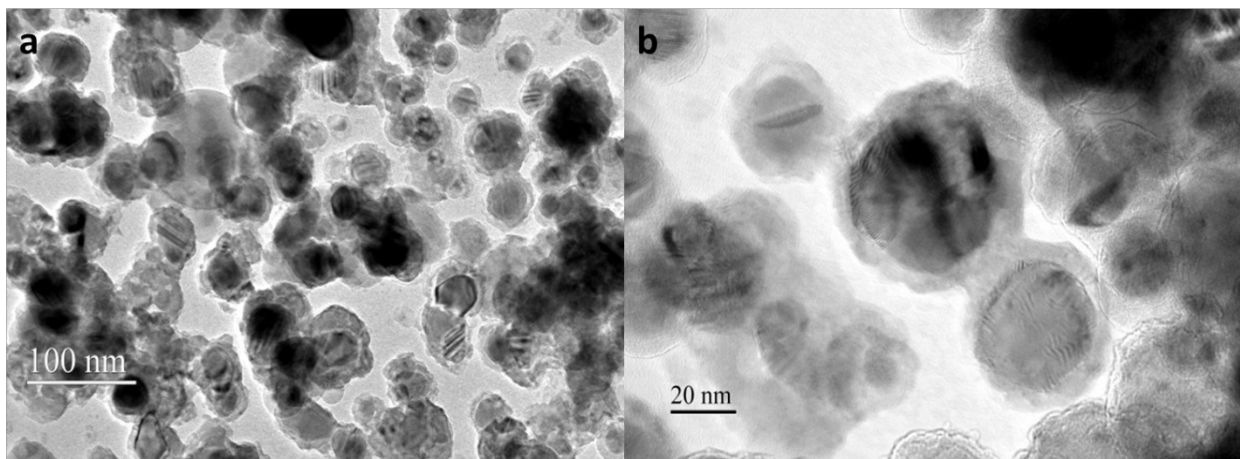
Figure 4: Post-Combustion TEM images (Al/CuO Nano Thermite) of the smaller particles collected on a Nickel TEM grid. Time for impingement: 150 µs

It is evident from these images that there are two distinct particle distributions. Also, the small particles were observed at both the separation distances and these small particles displayed a core-shell structure for the Al/CuO case, about which more will follow in the later sections.

Al/WO$_3$ and Al/Bi$_2$O$_3$ Nano Composite

The set of experiments were then broadened to include the Al/Bi_2O_3 and Al/WO_3. The near substrate images for both the cases as well as the impingement timescales are shown below in in Figure 5a and 5b for Al/WO_3 and Al/Bi_2O_3 respectively. The characteristic dimensions of the large particles are shown on the image itself for further clarity.
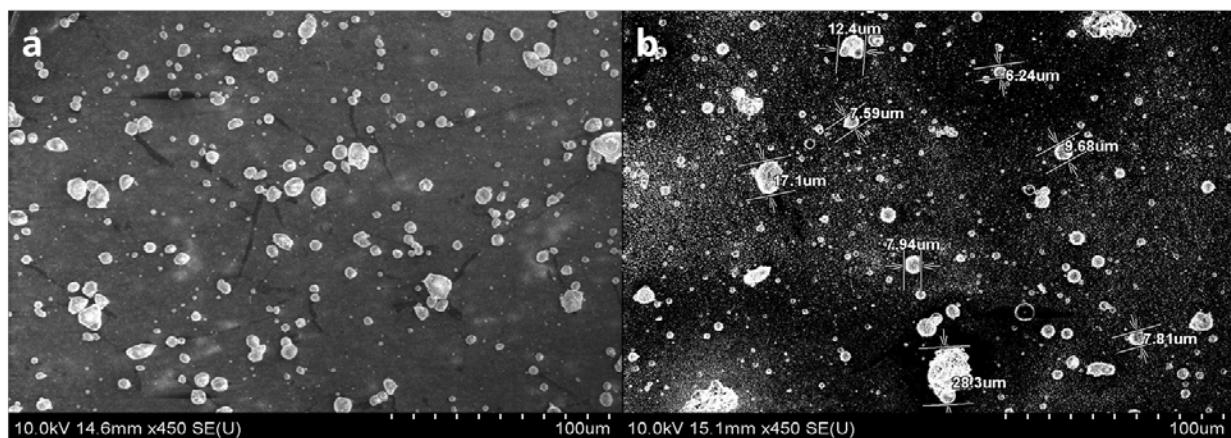

Figure 5: Typical particle sizes for the two Nano composites Al/WO_3 and Al/Bi_2O_3. a.) Al/WO_3, Time for impingement = 300 μs, Separation of the collecting substrate: 1 mm. b.) Al/Bi_2O_3, Time for impingement = 250 μs, Separation of the collecting substrate: 1 mm

IV.   Elemental Analysis

These studies shown that all three thermite systems form characteristically large particles which are on the order of micrometers and thus we may conclude follow a generic mechanism in this context. Also, evident from the TEM images in figure 4a and 4b, is the presence of nearly spherical particles (approximately 50 nm for Al/CuO) which display a core-shell structure for the Al/CuO case. The core consisted of the reduced metal from the metal oxide while the shell was an alloy of Aluminum, Oxygen and the reduced metal which was concluded from EDX analysis. Similar observations were made in the case of Al/Bi_2O_3. For Al/WO_3, the structure was not core shelled, but consisted of spherical particles composed of WO_x (Fig. 9a) as confirmed from EDX analysis, which we believe is a dissociation product of the parent WO_3.

As seen in Figure 3a, for the near substrate case, there is a distinctive bulb formation on the large particles, which was confirmed to be metallic copper from EDX analysis. For the far substrate

case, Figure 3b, the larger particles were heavily decorated with nano-sized particles on their surface. These nano particles consisted of the reduced metal and were similar to the ones seen in the TEM image in Figure 4a though the structure is not believed to be core-shell.

The surface of the large particles were identified to be an alloy of the kind $Cu_XAl_YO_Z$ (for the Al/CuO case) and is conjectured to be a mixture of $CuAl_2O_4$ and Al_2O_3 based on the phase diagrams [13] of $CuO-Al_2O_3$ mixtures and the atomic percentages obtained from the EDX analysis. It is reasonable to assume that the rapid quenching will lead to thermodynamic meta-stable states that may be very far from the equilibrium phases. The atomic percentages obtained for one particle varies greatly from that of another as the fuel/ oxidizer combinations involved in the formation of each particle can be far from stoichiometric and very different for each particle. Again we would like to clarify that these atomic percentages were obtained from a surface which was visually devoid of any decorations. We are not saying that these large particles are entirely composed of the aforementioned alloy.
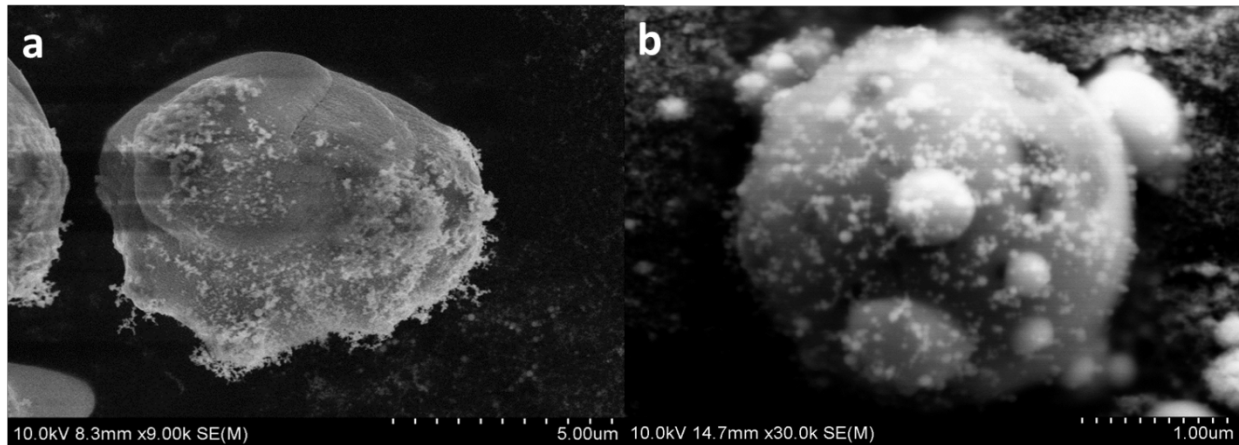
Figure 6: High magnification SEM images of the two Nano composites Al/WO₃ and Al/Bi₂O₃. a.) Al/WO₃, Time for impingement = 300 µs, Separation of the collecting substrate: 1 mm. b.) Al/Bi₂O₃, Time for impingement = 100 µs, Separation of the collecting substrate: 1 mm

Similarly, for the Al/WO_3 and Al/Bi_2O_3 cases, we observe large particles (Figure 6) whose surface was an alloy of aluminum, oxygen and the reduced metal. As in the case of Al/CuO, surface decorations could be seen in both these cases, but their nature differs considerably.

In the case of Al/WO_3 the surface decorations could be seen on fewer particles when compared to the case of Al/CuO. This can be understood based on our previous discussion about Al/WO_3 being

a poor gas generator at temperatures below approximately 2800K [8]. This restricts the vapor phase growth of particles, which we would prove in the later sections to be the mechanism behind the formation of the nano sized particles. In case of Al/Bi_2O_3, the surface decorations formed larger bulbs of the reduced metal as opposed to the fine nano structures in case of Al/WO_3. In order to attribute a generic mechanism to these results, we need a better understanding of the formation of the two particle distributions. As a starting point, it's imperative to know which of these particle distributions contribute to the majority of the species.

V.   Large vs. Small Particle Products and its significance on Mechanism

To begin our discussion we refer to the thermo-physical properties of the thermite mixtures in Table 1. The previous microscopy images showed there were two particle populations. Our first consideration is to understand the relative importance of these two populations in the context of a mechanism by estimating the relative mass distributions. To do this we employed digital image processing using the software ImageJ [26]. As example we show in Figure 7, an SEM image of the Al/CuO system. As we can see in Figure 7, the large particles are illuminated against a dark background. By adjusting the image threshold, we can single out the large particles from the background and use the particle analyzer tool to obtain the mean size of the particles. The results from this analysis are outlined in Table 2.

In this analysis, we assumed that the background is a uniform distribution of 50 nm particles, based on TEM images. This enables us, assuming spherical geometry and total aerial coverage of the small 50 nm particles, to estimate the volume of both the small and large particle populations. Though this is a crude assumption, it's not an unreasonable one for the analysis we are pursuing.
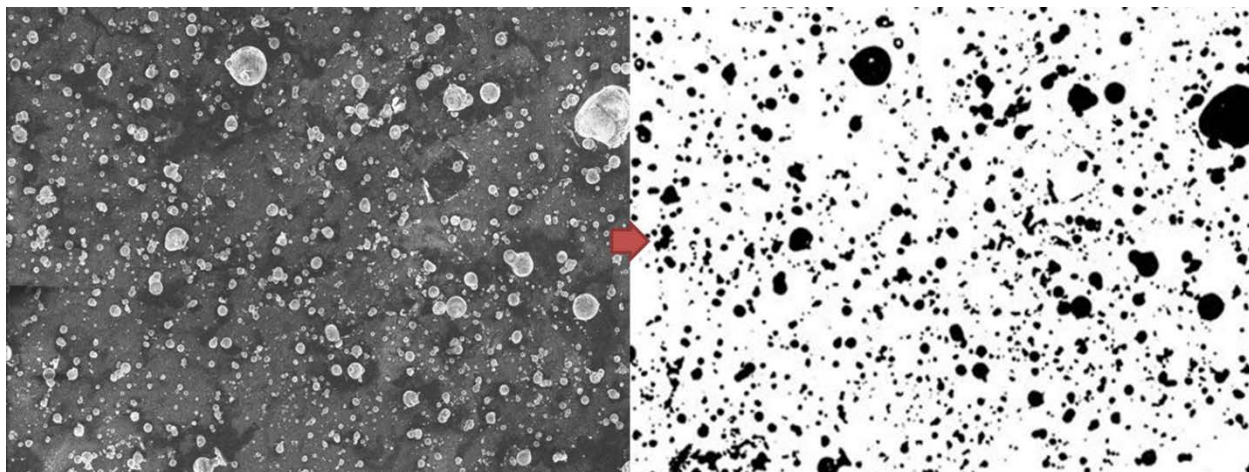
Figure 7: Image processing example for post-combustion Al/CuO. The image threshold was adjusted to single out the larger particles from the background.

The results of the image processing are presented in Table 2. While the large particles only comprise a small fraction of the aerial coverage ~ 15%, their average diameter of ~ 2.5 µm, leads to the result that approximately 85% of the volume is occupied by large particles. Assuming density is roughly constant between the two particle populations, the volume ratio is approximately the mass ratio. Similar analysis for Al/WO_3 and Al/Bi_2O_3 gave results that were experimentally essentially indistinguishable i.e. 90 and 85 % respectively).

Thus we may conclude that the bulk of the chemistry and energy release must pass through a mechanism that leads to the larger particles as opposed to the smaller nanoparticle products.

Table 2: Image processing results of post-combustion products

Total number of particles analyzed	N_L	1650
Mean projected area of the particle	S_L	$5\mu m^2$
Average particle diameter	D_L	$(5*4/\pi)^{0.5} = 2.5\ \mu m$
Total area composed of the dark particles (15%)	A_L	$8200\ \mu m^2$
Area covered by the white region (85%)	A_S	$46490\ \mu m^2$
Total number of 50nm particles in the white area	N_S	$\dfrac{A_S*4}{\pi*(D_S)^2} = 23688255$
Volume Ratio: $V_L/V_S = (N_L*D_L^3)\ /\ (N_S*D_S^3)$		≈ 9

We now turn our attention to how these two populations, one constituting particles in the micron scale, and the other in the 50-200 nm range can form. Most of these small particles are highly spherical, implying that they were in the liquid state at some point in their history, and were rapidly quenched on the substrate. The quench time for these nano particles were calculated using a lumped capacitance method [14] and was found to be on the order of a hundred nanoseconds [117ns] for a 50 nm copper particle. Furthermore, early in the formation, they were clearly in a free aerosol state as molten drops, else they would have aggregated with other small particles. These results show that the flame zone temperatures are considerably high so as to keep the nano sized particle in molten state.

From Table 1 for the Al/CuO mixture, we can deduce that copper metal, product of the redox reaction, would vaporize since the adiabatic flame temperature is near the boiling point of the metal. This allows us to post the question: How large a particle can be grown from the vapor in the transit time from the wire to substrate? To estimate the largest possible growth rate we assume that the copper vapor is in a supersaturated state with no nucleation barrier. This means we can assume both nucleation and growth follows the aerosol coagulation

equation in the free molecule regime [15]. The total mass of copper is estimated from the amount coated on the wire, which is approximately 0.1mg, and the stoichiometry of the mixture. The expansion volume for the products of the thermite reaction was considered as half the volume of the cylinder that forms between the wire and the collecting substrate i.e., the axis of the cylinder lies along the wire. This was evaluated for the near substrate condition, as that gives the maximum initial monomer concentration, thereby giving the fastest rate of coagulation. The proof for the far substrate case is redundant here as even with the higher rate, the big particles cannot be formed from the vapor phase coagulation, as enumerated in the forthcoming discussion.

For simplicity of calculation we assume a constant collision kernel, K= 5E-10 cc/s [15] so that the Smulochowski population balance is reduced to Equation 1 [15]:

$$N_\infty(t) = \frac{N_\infty(0)}{1 + K * N_\infty(0) * t / 2} \qquad (1)$$

Where, $N_\infty(0)$ is the initial monomer concentration (#/cc), $N_\infty(t)$ is the total particle concentration at time t (#/cc), t is time (s). The solution for the average particle diameter as function of time can be obtained by employing a simple volume conservation using the Van der Waals radius of copper (~0.14 nm) and assuming an initial monomer concentration equal to the maximum vapor phase concentration of Cu.
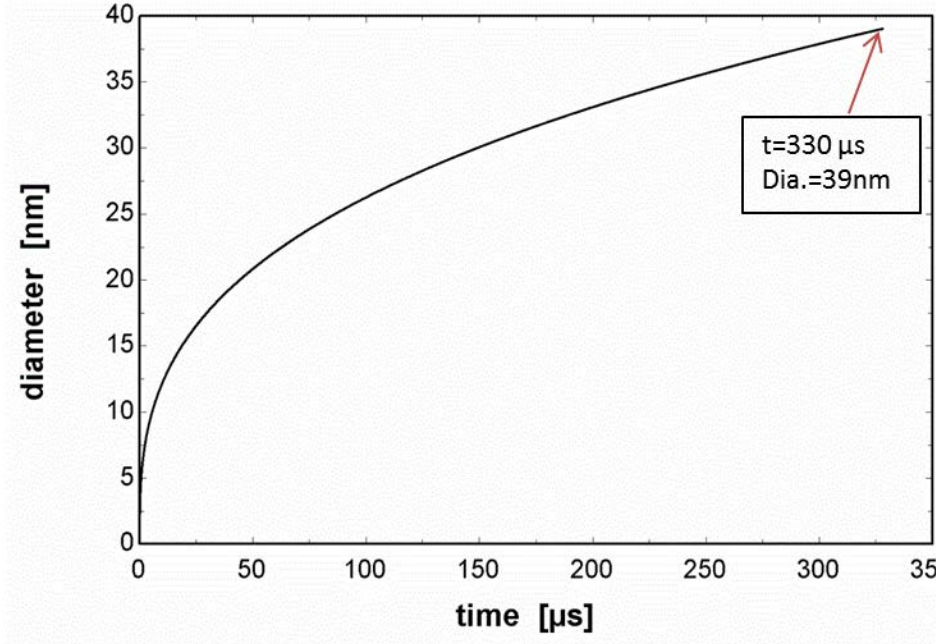
Figure 8: Copper particle growth using Equation , and assuming Cu vapor in supersaturated state with no nucleation barrier to condensation – i.e. maximum growth rate.

Figure 8 shows the growth of particles as a function of time at effectively the maximum collision rate. We see that at ~330 µs, which corresponds to what we believe is the transit time for the particles to the substrate, the nominal particles size should be about ~40 nm. This is reasonably consistent given the approximations in our calculation with the TEM results for the small particles. *But more significantly it says that there is no way that the large micron size particles, which will be recalled constitute the bulk of the mass, can form from the vapor.* In their work on arrested reactive milling, Schoenitz et al. [16] also found large particles in the product of Al/MoO$_3$ combustion. In our previous work by Sullivan et al. [14], real time X-ray phase contrast imaging was performed to substantiate the formation of sintered particles early in the reaction. They found large particles forming rapidly and early in the reaction. Thus we believe the large particles correspond to aluminum-metal oxide reaction that must have occurred in the condensed phase.

VI. Phenomenological Mechanism

A generic mechanism can be attributed to these results. From the previous EDX results, we stated that the large particles where primarily composed of an alloy of aluminum and oxygen. These particles are orders of magnitude greater than the nano sized particles which we concluded to be the products of vapor phase growth. Also, from the previous calculations, we proved that the large particles cannot be formed from vapor phase oxidation and subsequent growth, hence a condensed phase oxidation is under play here. Cases where there is a bulb formation can be explained as a consequence of the presence of low melting nano particle species. The large particles are the result of post oxidation sintering, hence we can safely say that their temperature would, at some point in their evolution, be above the melting point of alumina (2313 K). As the nano particles grow from the vapor phase, they would collide with these large particles and stick onto them. The criterion for bulb formation is that the melting point of the nano particle be lower than the ambient temperature. In this case, the incident, molten nano particles would immediately coalesce upon collision and phase separate forming the bulb. This can be confirmed from the melting points of Bismuth and Copper (Cu: 1357K, Bi: 545K), which are low melting, and as predicted forms bulbs. Such bulbs were observed in the study by Schoenitz et al. [16] in a pressure cell, implying that the nature of these formations from our wire heating experiment does not create an artificial condition.

In case of tungsten, the nano particle formed should have a higher melting point than the ambient temperature thereby not coalescing on collision and the subsequent collisions would pile on resulting in fine nano structures. The exact nature of the composition of the particles is extremely difficult to find as each particle can have a specific evolution history thereby leading to varied compositions. The purpose of this work is not to specify the identities of all the alloys that form, but rather to capture some common reaction features inherent to these systems. From the figure below, we can see the near perfect spherical shape of these small particles (obtained for the Al/WO$_3$ case) and accompanying it, we have the diffraction pattern that proves that these particles are amorphous which implies a rapid quench.

.
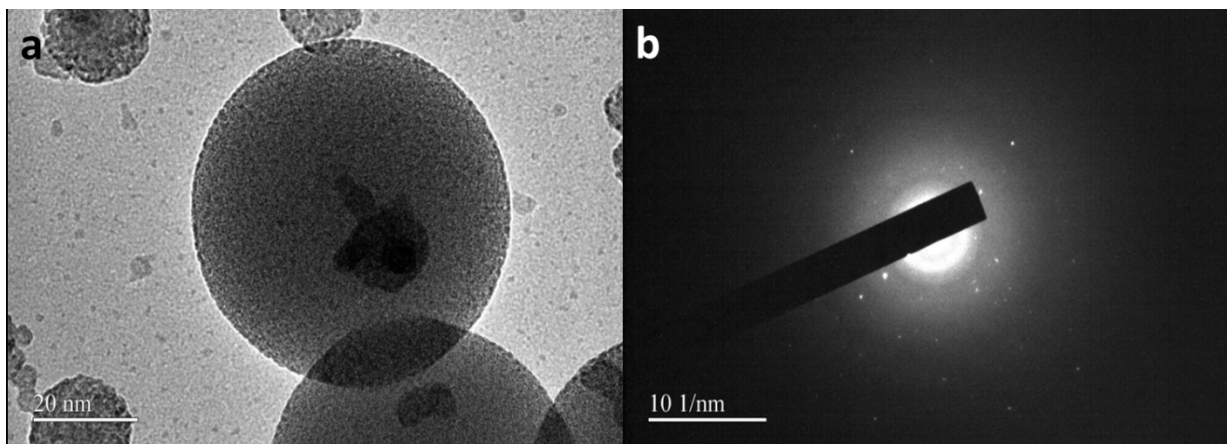
Figure 9: a.) The near perfect spherical shape of the small particles obtained from Al/WO₃ reaction. b.) The diffraction pattern showing random spots proving the amorphous nature of the particle.

From our coagulation calculation it is evident that the large particles cannot be formed from the vapor phase. In one of our previous publications, we discussed the possibility of early sintering of the reactants due to the heat released by the exothermic reaction, termed Reactive Sintering [14]. We believe that the current evidence strengthens the arguments made in that work.

As outlined in references [14] and [27], the reaction initiates at the reactant contact points. The oxidation can occur with both the participating species (Aluminum and Oxygen) diffusing towards each other. Once the exothermic oxidation reaction initiates, the system temperature and consequently, the vapor pressure of the reduced metal increases causing more metal to go to the vapor state. This vapor subsequently nucleates and grows to the appropriate size depending on the transit time. The alumina product which is molten is thus driven by coalescence and surface tension to be highly spherical. As collision probability favors small particles impinging on larger ones [15], the copper particles collide with large alumina particle and they stick or lump up on the surface of the alumina particle forming the bulbs depending on the ambient temperatures. Regarding the large particles, although we stated that they are an alloy consisting of aluminum, oxygen and the reduced metal, we have no reason to believe that the whole particle would have this composition. We believe that the particle is primarily composed of alumina formed from condensed phase chemistry and on the surface of the particle, there is significant alloying due to

the coexistence of molten alumina and reduced metal.

As we move away from the combustion zone, the temperatures drop sufficiently that the small copper particles, now solid, coagulate with the larger particle to form a fluffy decoration on the particle surface as seen in Figure 10b below, which by EDX have been confirmed to be predominantly composed of elemental copper. Also shown in Figure 10a is the far substrate case of Al/WO$_3$. This result may seem surprising as our previous discussion void the possibility of heavy surface decorations for the case of Al/WO$_3$. A possible cause for this would be that the local metallic vapor concentration around the large particle would be considerably large in this particular case. Hence, this should be considered as an exception to the generic formulation. As we mentioned earlier, after a thorough sampling of the substrate, we could notice that the surface coverage in case of large particles in the Al/WO$_3$ system was much lesser than that of Al/CuO and Al/Bi$_2$O$_3$ systems.
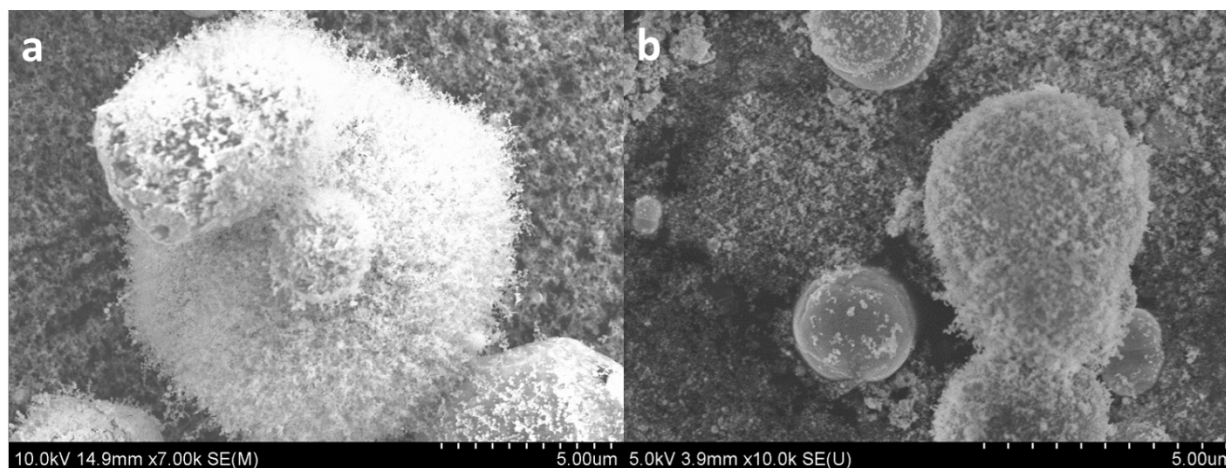
Figure 10: a) Far substrate case for Al/WO$_3$ nano thermite, b) Al/CuO nano thermite, showing the nano particle aggregates on the surface of the large particle.

Regarding the small particles, we could observe that they had a core shelled structure for the Al/CuO and Al/Bi$_2$O$_3$ case and were spherical particles composed of WO$_x$ for the Al/WO$_3$ case. The core consisted of the reduced metal while the shell was an alloy of aluminum, oxygen and the reduced metal. The typical sizes varied between 50nm and 200nm for all the three systems. The core shelled structure can be attributed to the simultaneous coagulation of reduced metal and alumina from gas phase. Due to the small sizes, an energetically favorable morphology after phase

separation would be the core shelled structure rather than nano sized bulbs. For the case of Al/WO$_3$, the presence of WO$_x$ nano particles suggests that the oxidizer is not entirely decomposing to the reduced metal. This is in conjunction with the prevalent results that WO$_3$ produces little or no oxygen in the gas phase [25]. A possible explanation would be that the aluminum reacts with the oxygen in the condensed state, thereby reducing the oxidizer to a lower valent oxide, which subsequently vaporizes and nucleates.

VII. Conclusion

Three metastable interstitial reactive composites were studied in which the products were impinged on a substrate and looked at under an electron microscope. The results show that there are two distinct populations of particles. The larger micron sized particle distribution proves that there is considerable condensed phase oxidation in all three cases as they cannot be formed from gas phase coagulation. The calculated mass ratio of the two distributions shows that majority of the products are formed through condensed phase chemistry. This method provides additional proof that the nano scale reactants when combusted in bulk do not combust efficiently as there is considerable condensed phase oxidation. Also, the nature of the products formed was analyzed, with the large particles primarily composed of alumina and the small particles being the reduced metal. The product morphology was observed to be dependent on the substrate separation and the physical properties of the materials involved. This result can help us in developing better experiments where the fuel and the oxidizer can be finely dispersed using gas generators etc. thereby reducing the proximity of multiple fuel particles hence reducing condensed phase oxidation.

VIII. References

[1] C.E. Aumann, G.L. Skofronick, J.A. Martin, J. Vac. Science Tech., B13 (3) (1995) 1178-1183
[2] A. Rai, K. Park, L. Zhou, M. R. Zachariah, Comb. Theory and Modelling 10 (5) (2006) 843-859
[3] A. Rai, D. Lee, K. park, M.R. Zachariah, J. Phys. Chem. B (2004), 108, 14793-14795
[4] V. I. Levitas, B. W. Asay, S. F. Son, M. L. Pantoya, App. Phys. Letters, 89, (2006) 071909
[5] M.A. Trunov, M. Schoenitz, E.L. Dreizin, Comb. Theory and Modelling 10 (4) (2006) 603-623
[6] E. Sanders et al. J. Prop. & Power 23 (4) (2007) 707-714
[7] L. Zhou, N. Piekiel, S. Chowdhury, M.R. Zachariah, J. Phys. Chem. C 114 (2010), 14269-

14275

[8] K. Sullivan, M.R. Zachariah, J. Prop. & Power 26 (3) (2010), 467-472

[9] R.A. Williams, J.V. Patel, A. Ermoline, M. Schoenitz, E.L. Dreizin, Combustion and Flame 160 (3) (2013), 734-741

[10] C.M. Drew, A.S. Gordon, R.H. Knipe, Heterogeneous Comb., Progress in Astro. and Aero. 15 (1964), 17-39

[11] L. Zhou, N. Piekiel, S. Chowdhury, M.R. Zachariah, Rapid Commun. Mass Spectrom. 23 (2009), 194-202

[12] S. Chowdhury, K. Sullivan, N. Piekiel, L. Zhou, M.R. Zachariah, J. Phys. Chem. C 114 (2010), 9191-9195]

[13] ACerS – NIST Phase Equilibria Diagrams V 3.4.0

[14] K.T. Sullivan, N. Piekiel, C. Wu, S. Chowdhury, S.T. Kelly, T.C. Hufnagel, M.R. Zachariah, Combustion and Flame 159 (2012), 2-15

[15] Smoke, Dust, and Haze, S. Friedlander, Oxford University Press, (2000)

[16] M. Schoenitz, T.S. Ward, E.L. Dreizin, Proceedings of the Combustion Institute 30 (2) (2005) 2071-2078

[17] T. Bazyn, N. Glumac, H. Krier, T.S. Ward, M. Schoenitz, E.L. Dreizin, Combust. Sci. and Tech. 179 (2007), 457-476

[18] C. Farley, M. Pantoya, J. Therm. Analy. Calorim. 102 (2010), 609-613

[19] D. T. Osborne, M.L. Pantoya, Combust. Sci. and Tech., 179 (2007), 1467-1480

[20] B.W. Asay, S.F. Son, J.R. Busse, D.M. Oschwald, Propellants, Explosives, Pyrotechnics 29 (4) (2004), 216-219

[21] D. Stamatis, A. Ermoline, E.L. Dreizin, Combustion Theory and Modelling 16 (6) (2012), 1011-1028[22] G. Jian, N.W. Piekiel, M.R. Zachariah, Journal of Physical Chemistry 116 (51) (2012), 26881-26887

[23] B. Henz, T. Hawa, and M.R. Zachariah, J. Appl. Phys., 107, 024901 (2010)

[24] E. Beloni, P. R. Santhanam, E. L. Dreizin, Journal of Electrostatics 70 (2012), 157-165

[25] G. Jian, S. Chowdhury, K. Sullivan, M. R. Zachariah, Combustion and Flame 160 (2) (2013), 432-437

[26] ImageJ   http://rsb.info.nih.gov/ij/

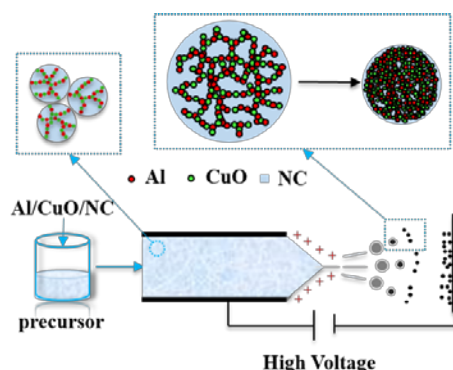[27] K.T. Sullivan, W.A. Chiou, R. Fiore, M.R. Zachariah, Applied Physics Letters, 97 133104 (2010)

III. Results for FY-14

Development of a new class of materials : Microparticles comprised of nanoparticles of thermite and biocide containing materials.

Due to its high enthalpy and ready availability, conventional aluminum powders with an average size of 3-20 μm, are commonly employed in solid rocket propellant and other propulsive systems. Although the energy density is increased after incorporation of micrometer-sized aluminum fuel in propellant systems, the burning rate however was not found to improve much, resulting in low rates of energy release. Additionally, the oxide coating on the surface of microsized aluminum sufficiently passivates the fuel to a high ignition temperature ~2300 K. In contrast, the use of nanoscale aluminum lowers the ignition temperature to < 1000K, with a much enhanced burning rate, and a lower ignition delay time. Unfortunately nanometallic fuels suffer from processing challenges, that have significantly retarded their utility, most primarily because their very high surface area/small particle size increases the viscosity of polymer binder and oxidizer mix, such that high mass fractions of fuel cannot be formulated.

We have built on the past year where we created gelled aluminum particle to include materials that involve both fuel – oxidizer and biocide components.

A. This includes demonstration of an electrospray route to assemble Al and CuO nanoparticles into micron composites with a small percentage of energetic binder, which shows higher reactivity than nanothermite made by conventional physical mixing. The electrospray approach offers the ability to generate micro scale particles with a narrow size distribution, which incorporates an internal surface area roughly equivalent to the specific surface area of a nanoparticle. The size of the micron scale composites could be easily tuned by changing the nitrocellulose content which is used as the binder. The composites were burned in a confined pressure cell, and on a thin rapidly heated wire to observe burning behavior. In Fig 2 we see that the sample of 5 wt. % nitrocellulose showed the best response relative to the physical mixing case, with a 3X higher pressure and pressurization rate. The ignition characteristics for these micron particles are essentially equivalent to the nanothermite despite their significantly larger physical size. It appears that electrospray assembly process offers to potential advantages. 1. Enhanced mixing between fuel and oxidizer; 2. Internal gas release from nitrocellulose that separates the particles rapidly to prevent sintering. The later point was shown by comparing the product particle size distribution after combustion.


Fig. 1 Electrospray formation of nanostructured microparticles.
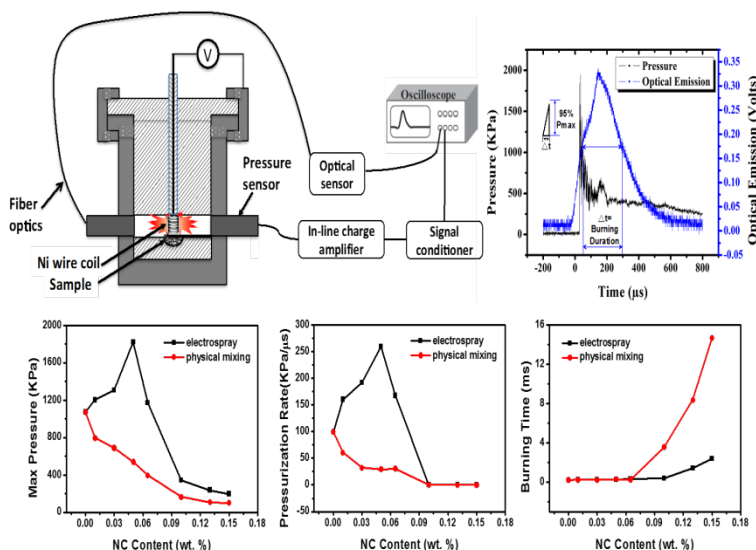
Fig.2 Maximum pressure (a), pressurization rate (b) and burning time (c) of the nanothermite samples prepared by electrospray and physical mixing as a function of NC content

One recurring strategy for neutralization is to deliver both heat and biocidal agents simultaneously. To that end we have extended the above work to create Al/CuO nanothermite microparticles containing molecular iodine ranging from 5 wt. % to 50 wt. %, and evaluate their combustion properties and potential use as sporicidal agents. The reactivity was evaluated using a constant-volume combustion cell, which showed that, with increasing iodine content, the $Al/CuO/I_2$ reaction is decreased by several orders of magnitude, while the burning time increased. Results also show that the reactivity of the composites can be increased by reducing the particle loading in precursor. The post-combustion products are determined to be Al_2O_3, Cu and CuI. T-Jump wire ignition experiments showed that for microparticles containing up to 20 wt. % of iodine are ~750 °C, and similar Al/CuO composites. *In-situ* rapid heating SEM imaging of $Al/CuO/I_2$ composites confirmed that iodine was released (~500 °C) prior to the thermal reaction (~800 °C).
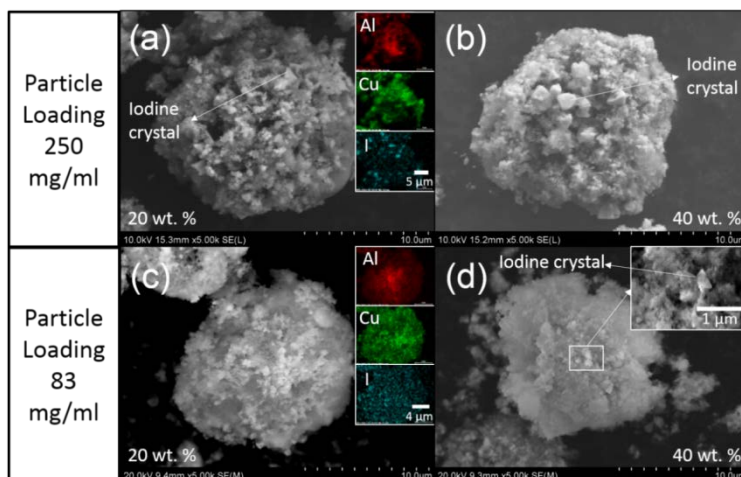
Figure 3. SEM images of iodine-containing Al/CuO composites. Iodine content: 20 wt. %, (a, c), 40 wt. % (b, d). Note a and b are microparticles from precursors with particle loading of 250 mg/ml; c and d are from precursors with particle loading of 83 mg/ml. The inserts in Figure 3a and 3c are EDS elemental maps.
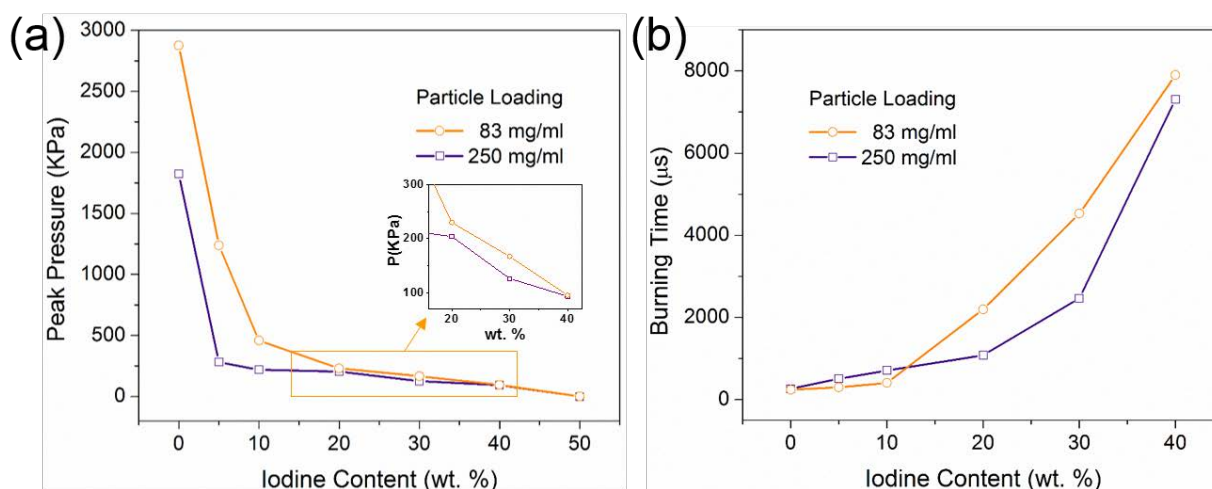
Figure 4. Peak pressure and burning time as a function of iodine content. Note: 50 wt. % iodine case can be ignited but is too weak to obtain an optical signal.

In addition to elemental iodine three metal iodate nanoparticles, $Bi(IO_3)_3$, $Cu(IO_3)_2$, and $Fe(IO_3)_3$, were synthesized and assembled with aluminum nanoparticles using an electrospray technique to create microparticles. The metal iodates act as a strong oxidizer to participate in formulating high reactive thermite mixtures, while containing high mass loadings of iodine (e.g. in the case of bismuth iodate >50 wt. % of iodine). This resultant thermite reaction generates both high-temperature and high-pressure with the added benefit of the release of iodine as a longer lived bactericide. This work shows that metal iodate and aluminum nanoparticles, when intimately assembled into micro-sized nanothermites by an electrospray process, show significantly improved reactivity and sporicidal performance over conventional metal oxide-based thermites.

Table 1. The pressure cell results of physically mixed nanothermites, sample mass: 25.0 mg. Note: All the composites contain no NC. *The AFT of Al/Bi_2O_3 thermite is only 3031 K. (Because this was a fuel lean mixture, stoichiometric ratio=1, to optimize pressurization rate) Note: The formation energies of these oxidizers were calculated based on the data at https://materialsproject.org/. The formation energies of $Bi(IO_3)_3$, $Cu(IO_3)_2$ and $Fe(IO_3)_3$ are calculated as -1282 kJ/mol, -725 kJ/mol and -1293 kJ/mol, respectively.

Al+Oxidizer	Pressure (MPa)	Pressurization (GPa/s)	Burning Time (μs)	Adiabatic Flame Temperature (K)	Stoichiometric Ratio
Bi_2O_3, 90-210 nm	1.0	54	240	2333*	1.3
$Bi(IO_3)_3$, ~90 nm	2.3	770	150	4062	1.0
CuO, ~50 nm	1.1	100	220	3054	1.0

98

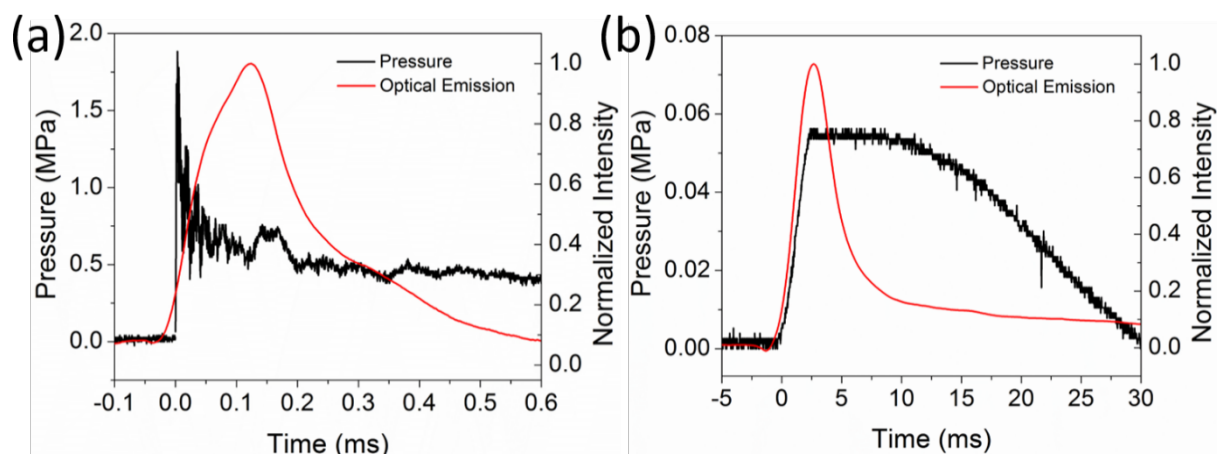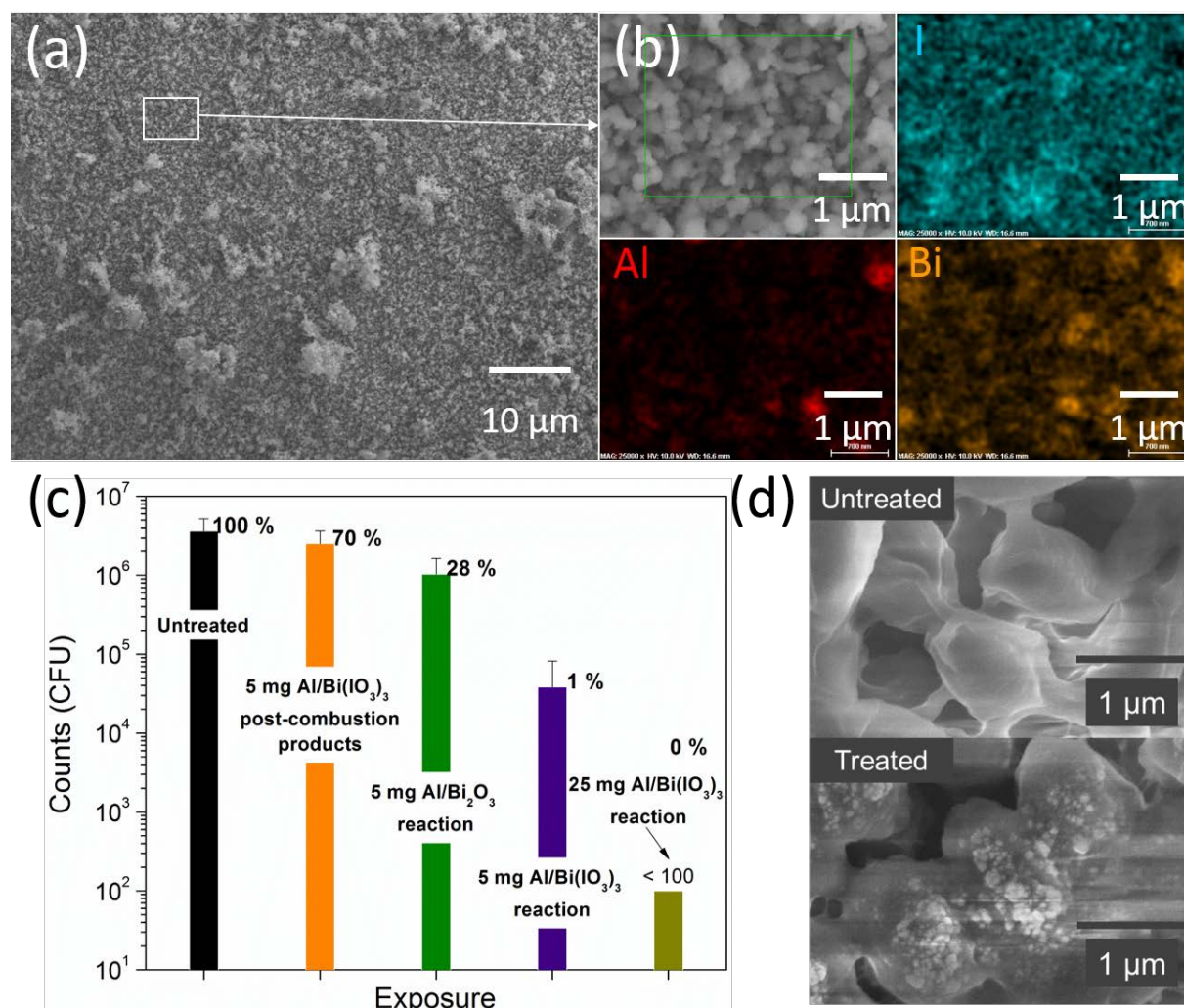|					
Cu(IO$_3$)$_2$, ~200 nm*	1.8	225	170	4061	1.0
Fe$_2$O$_3$, ~50 nm	0.06	0.02	3330	3027	1.0
Fe(IO$_3$)$_3$, ~70 nm	1.9	590	170	4043	1.0

Figure 5. a, b) Pressure and optical emission profiles of Al/Fe(IO$_3$)$_3$ (a) and Al/Fe$_2$O$_3$ (b) nanothermite reactions.

Figure 6 *a, b) SEM and energy dispersive X-ray spectroscopy (EDS) results of Al/Bi(IO₃)₃ thermite reaction products. c) CFU counts from the spores treated by 5.0 mg Al/Bi(IO₃)₃ post-combustion products, 5.0 mg Al/Bi₂O₃ thermite reaction, 5.0 mg and 25.0 mg Al/Bi(IO₃)₃ thermite reaction. d) SEM images of spores before and after undergoing the Al/Bi(IO₃)₃ thermite reaction (5.0 mg), respectively. Note: all the composites are produced by electrospraying with 5 wt. % NC. The labeled numbers in c are survival ratios of spores.*

3. Dispersion characteristics of thermite samples.

NanoThermite reactions are mechanistically not well understood, due to their ultra-fast transient nature, and the complexity of probing both the vapor-phase and condensed-state chemistries. In this work we examine the combustion product particles of three nano-sized thermite systems (Al/CuO, Al/WO₃, Al/Bi₂O₃) as a probe of the underlying mechanism. Electron Microscopy (EM) and Energy-dispersive X-ray Spectroscopy (EDX) were used to evaluate the combustion product particle size distribution and composition. The results show two distinct product particle size distributions common to all three oxidizers. The larger particles are super-micron (though the precursors were nano-sized) and comprise approximately 90% of the product mass. Simple scaling

arguments show that the large population cannot be formed from the vapor given the available residence time. The smaller distribution is sub-100 nm which is primarily the reduced metal formed from vapor phase condensation. This result implies that the majority of the global reaction and thus the energy release is occurring in the condensed phase.

To explore this further the reaction between metallic fuel and oxygen carriers is investigated through ultra–fast laser heating of Aluminum and Copper Oxide (CuO) nanoparticles (NPs) using Movie Mode Dynamic Transmission Electron Microscopy (MM-DTEM) capable of high spatial and temporal resolution. Nanothermite materials heated *in situ* at ~10^{11} K/s shown in Figure 7 morphological changes on timescales of 1-5 μs. The resulting structures were typically phase-separated into adjoining spheroids. Further analysis with energy dispersive spectroscopy (EDS) and selected area electron diffraction (SAED) revealed that both the extent of reaction and the products produced were comparable to reactions driven by other modes of heating with slower rates. These results indicate that condensed phase and interfacial reactions are a fast and dominant mechanism in the nanothermite combustion.
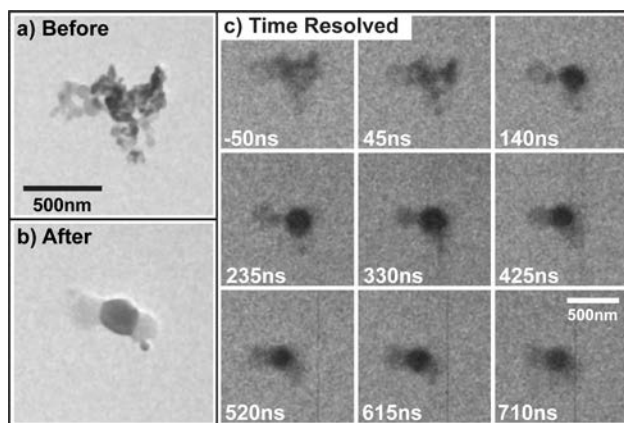

Figure 7. *Morphological changes of Al and CuO NP's heated with a 532nm laser (Pulse length= 12 ns; Peak laser fluence =0.3 kJ/m^2). (a) and (b) were taken in conventional TEM mode while the images of (c) were taken with pulsed electrons. (a) shows the aggregate prior to heating while (b) shows the resulting reacted material morphology. (c) Movie-Mode DTEM image sequence showing the change in morphology with time. Each frame was taken with a ~20 ns electron pulse duration and 95 ns time delay between pulses. The listed times are relative to the peak intensity of the ~12 ns sample heating laser pulse. The same scale is used for both (a) and (b) with another scale shared by all the images of (c).*

The characteristic diffusion time is defined as $t = \frac{l^2}{D}$, where l is the characteristic length scale and D is the diffusion coefficient. The important length scale here is the primary particle size radius. Thus for a 30 nm diameter particle, the observed delays of 500 ns and 5 μs correspond to effective diffusivities of ~4.5×10^{-6} and ~4.5×10^{-7} cm^2/s respectively. While these values are high compared to the reported oxygen diffusivities in copper oxide (~10^{-9} cm^2/s for O in Cu$_2$O at ~1500 K), at high temperatures and under vacuum conditions, CuO is at these heating conditions far outside of equilibrium stability .   If we assume an activation energy of ~1-2eV (typical values found for copper oxide) for diffusion, the difference in estimated diffusivities can be accounted by a ~200-

350 K difference in temperature between the two cases, which is consistent with the absorption and temperature estimates described above.

This explanation implies that exothermic reaction is not necessary for the morphological changes observed in these experiments. To evaluate this further, elemental analysis was performed using energy dispersive X-ray spectroscopy (EDS) line scans as in Figure 8. These results clearly confirm that the light areas are Al rich and the darker areas are Cu rich. Further they indicate that all of the oxygen is associated with the aluminum. In addition there appears to have been some alloying between the Al and Cu, although this was not consistent for all cases. This confirms that there was significant interaction between the Al and CuO, including the exchange of oxygen for reaction. However, it should be noted that the total amount of oxygen is diminished in comparison to the amount of Cu present. This loss of oxygen is consistent with an initial reduction to Cu_2O, which leads to both coalescence and subsequent reaction.
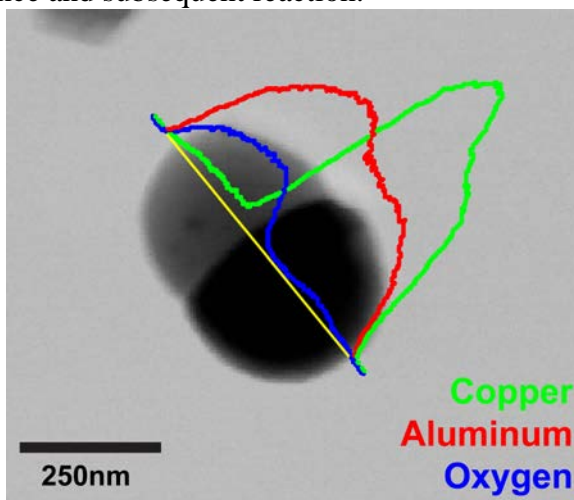
Figure 8. *Post-reaction product from an Al/CuO laser heating experiment that was analyzed with an EDS line scan. The red line indicates the intensity of the Al signal, green represents Cu, and blue represents O. The results indicate a lighter Al/O phase and a darker Cu/Al phase.*

The DTEM experiments compare well with reaction dynamics of those observed in thermally driven reactions nanocomposite. These results show that the oxide alone will release O_2 at temperatures slightly lower than the ignition temperature for the thermite. Further, a significant amount of gaseous oxygen was present in the system during Al/CuO reaction. Thus any condensed phase interaction between the two materials involves a reduced phase of CuO.

One additional aspect of these results is that it appears due to this rapid sintering and condensed phase reaction that the global reaction has not reached completion. In Figure 9 we see a focused ion-beam slice of a product particle from the reaction between Al and CuO. What we see is that there is a deficiency of oxygen of some 25% globally within the particle. Note that the product particle is much bigger than the starting particle indicates significant reactive sintering.
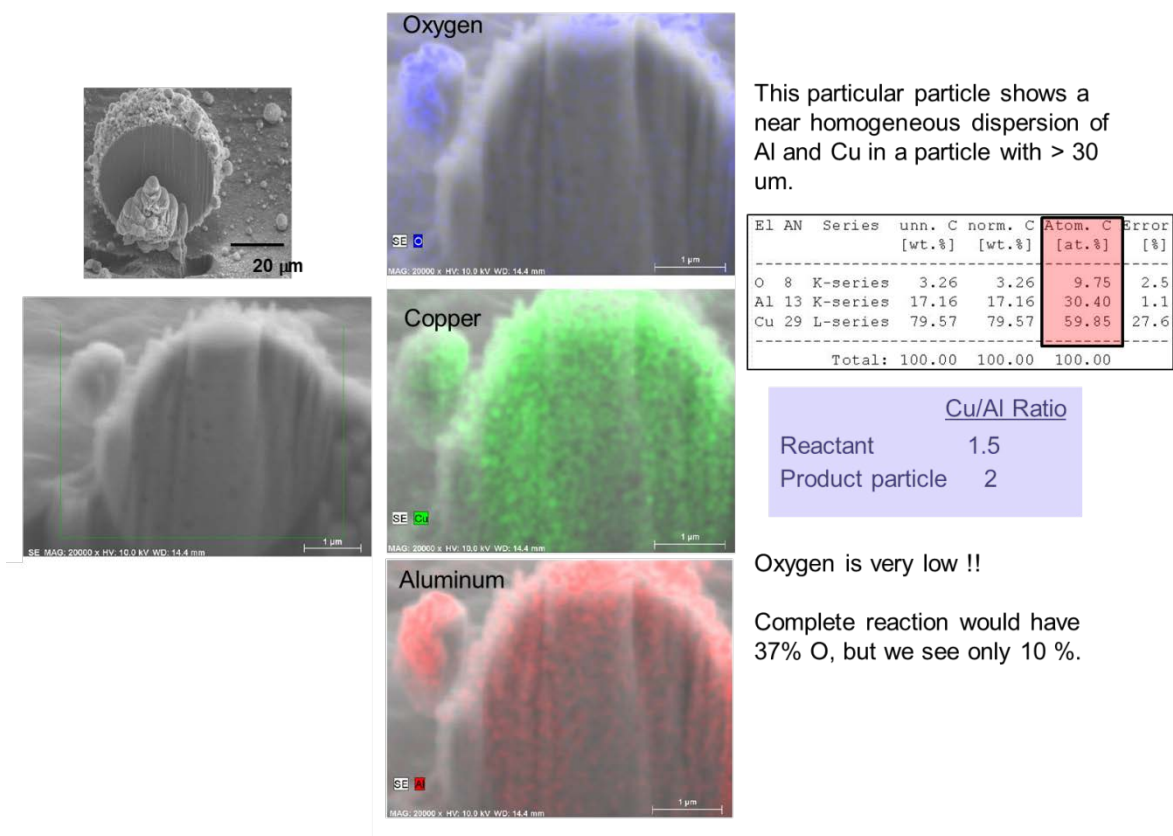
Figure 9: *FIB slice of a product particle and EDS maps. The results show a significant deficiency of Oxygen implying that reaction has not gone to completion.*

The question at hand is if indeed these nanoscale objects are not going to completion, it is presumably due to the long diffusion lengths required for reaction due to sintering. We show in Figure 10 product particles for physically mixed Al/CuO thermite and the mesoparticles created by electrospray. It is quite clear that the mesoparticle products are significantly smaller.

This result suggests that more energy may be extracted from the mesoparticle, however this is yet to be shown,
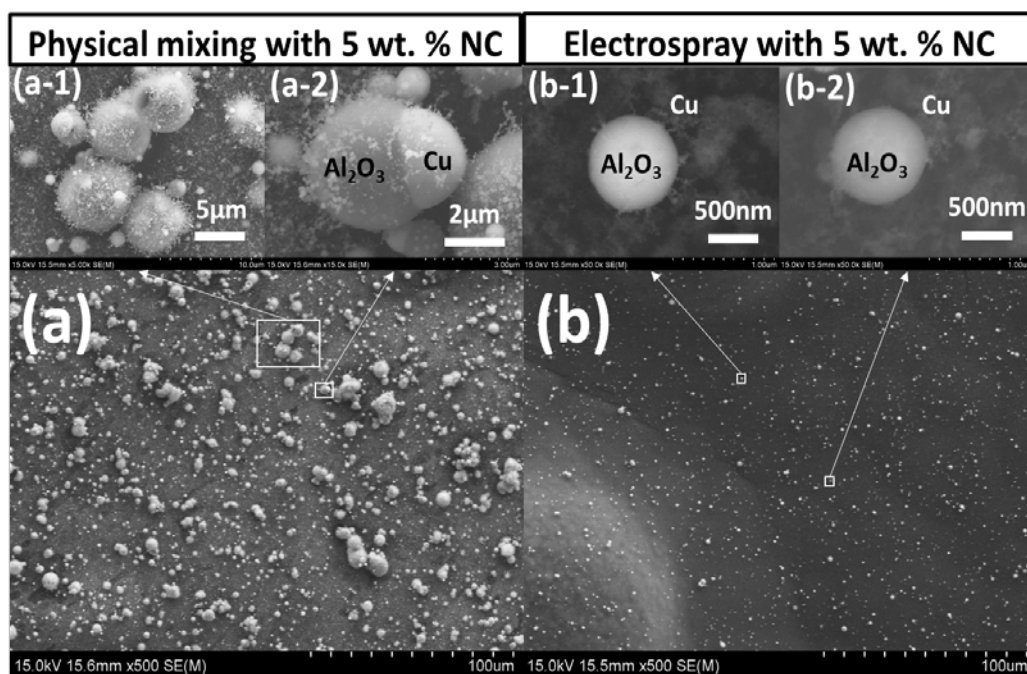
Figure 10: *Comparison of product particles resulting from physically mixed vs eh ES mesoparticle Al/CuO thermite. The much smaller product particles in the ES system imply shorter reaction lengths.*

DEPARTMENT OF DEFENSE

DEFENSE THREAT REDUCTION
AGENCY
8725 JOHN J. KINGMAN ROAD
STOP 6201
FORT BELVOIR, VA 22060
     ATTN: A. LYALIKOV

DEFENSE TECHNICAL
INFORMATION CENTER
8725 JOHN J. KINGMAN ROAD,
SUITE 0944
FT. BELVOIR, VA 22060-6201
     ATTN: DTIC/OCA

DEPARTMENT OF DEFENSE
CONTRACTORS

QUANTERION SOLUTIONS, INC.
1680 TEXAS STREET, SE
KIRTLAND AFB, NM 87117-5669
     ATTN: DTRIAC